A MULTI-FREQUENCY AND MULTI-PARAMETER ELECTROMAGNETIC NDE FRAMEWORK FOR COMPLEX MATERIAL CHARACTERIZATION

By

Xiaodong Shi

A DISSERTATION

Submitted to
Michigan State University
in partial fulfillment of the requirements
for the degree of

Electrical Engineering – Doctor of Philosophy

2022

ABSTRACT

A MULTI-FREQUENCY AND MULTI-PARAMETER ELECTROMAGNETIC NDE FRAMEWORK FOR COMPLEX MATERIAL CHARACTERIZATION

By

Xiaodong Shi

Technological advances have been observed due to continuing discoveries and applications of materials exhibiting novel or enhanced properties, which offer superior performance to conventional products and processes. When these materials and parts are used in some critical applications and directly impact the safety and success of a project, it is crucial to ensure their quality and reliability. NDE technologies have rapidly evolved over the past years. The application of these technologies has improved the quality and the reliability of components that are being used in various fields.

This work aims to develop a reliable NDE framework that can characterize the materials with complex shapes and/or properties. The studies will mainly focus on the electromagnetic methods, design/optimize the sensing system, and processing of the data to utilize information from multi frequency and multi-parameter testing. Strain distribution is an essential indicator of stress concentration, damage initiation, and evolution. Many dielectric materials sustain considerable strain before failure. The first part of the research deals with designing a near-field microwave high-resolution imaging (NMHI) system that is able to estimate very large deformation for dielectric materials. The main contributions of this part of the research are the following: a) designing a rapid imaging system that is able to provide high-resolution information of the OUT. b) a multi-modality data fusion technique is applied to evaluate the strain of Polyamide 11 (PA-11) through simulations and experiments. c) the relationship between near-field microwave signal measured from the sample and the sample's mechanical properties has been studied.

The second part of the research focuses on the design of a root phenotyping system. The opaque surrounding environment of the roots and the complicated growth process make the in-situ and non-destructive root phenotyping faces significant challenges, which also raises tremendous research interest. Existing methods for root phenotyping are either unable to provide high-precision

and high accuracy in-situ detection or change the surrounding root environment and are destructive to root growth and health. The contributions of this part of the research are the following: An ultra-wideband microwave imaging system is designed and optimized for non-destructive root phenotyping with the potential of in-situ monitoring. The system has been developed to estimate the location and shape of the root with the soil's background noise. The capability to provide the size and localization information of single and multiple roots demonstrates the simulation framework's robustness. Precise results and high imaging quality of the reconstruction achieved from the experiment studies validate the proposed microwave imaging method's accuracy. The non-iterative TR algorithm proposed for signal processing is computationally efficient, enabling rapid roots localization. This work also shows its ability to real-time monitor the root system in a natural soil environment. The advantage of its fast scanning ability and robustness enables the microwave imaging technique to be deployed in fields for scanning a large volume of soil and accessing the state of roots in a real-time manner.

The third part of the research deals with designing portable NDE sensors to meet different scanning requirements. Many constraints need to be considered when designing the NDE sensing system for the robot. The sensor's footprint is limited by the design of the robotic system as well as the complexity of testing structures. The allowable maximum power consumption of the entire system is constrained by the available power supply unit on the robot. Many environmental conditions could affect the NDE results obtained from the robotic actuating and sensing. Such would add inevitable uncertainties to the acquired data or restrict actuation access, lowering the fidelity and resolution of NDE data used for further damage assessment and analysis. To overcome these aforementioned challenges and obtain optimized sensing outcomes, the proposed NDE sensors were customized to fit in the robotic system and workspace environment for power plant boiler inspection. These optimizations lead to a low-cost, lightweight, non-contact, and simplified NDE setup.

ACKNOWLEDGEMENTS

I would like to express my most sincere gratitude to my two major advisors: Dr. Yiming Deng and Dr. Lalita Udpa. For their extraordinary support, guidance, and encouragement during my Ph.D. study. Special thanks to their intellectual, financial support, inspiration, and invaluable advice. They have advised me not only on my research but also on my career and life. I feel fortunate to work with them and am proud to be a member of the NDEL research group.

I would like to express my sincere gratitude to my committee members: Dr. Satish Udpa, Dr. Rongrong Wang, and Dr. Vijay Srinivasan, for taking the time to serve on my committee and for providing invaluable comments and suggestions to enhance the quality of the dissertation.

I would like to thank my colleagues and friends of NDEL for their support and help. I'm very thankful for their valuable advice and help. I would like to mention my colleagues and friends Mohand Alzuhiri, Dr. Deepak Kumar, Dr. Chaofeng Ye, Dr. Anders Rosell, Dr. Zhiyi Su, Dr. Oleksii Karpenko, Dr. Anton Efremov, Dr. Saptarshi Mukherjee, Dr. Portia Banerjee, Dr. Vivek Rathod, Dr. Rajendra Prasath, Subrata Mukherjee, Srian Datta, Guillermo Huanes-Alvan, Fares Alharbi, Xuhui Huang, Zi Li, Bharath Shenoy, Ciaron Hamilton, Shuo Zhang and everyone else in NDEL.

Finally, I would like to thank my family for constant sources of love, support, and encouragement throughout my life.

TABLE OF CONTENTS

LIST OF TABLES

LIST OF FIGURES

LIST OF ALGORITHMS

KEY TO SYMBOLS AND ABBREVIATIONS

AM:	Additive Manufacturing
CFRP:	Carbon Fiber Reinforced Polymer
DC:	Direct Current
DIC:	Digital Image Correlation
DWT:	Discrete Wavelet Transform
FDTD:	Finite-Difference Time-Domain
FS:	Full Specimen
GFRP:	Glass Fiber Reinforced Polymer
HFSS:	High-Frequency Structure Simulator
TDWT:	Inverse Discrete Wavelet Transform
NDE:	Non-Destructive Evaluation
NMHI:	Near-field Microwave High-resolution Imaging
NS:	Notched Specimen
OUT:	Object Under Test
RF:	Radio Frequency
R_x:	Receive
SBC:	Scattering Boundary Conditions
TR:	Time Reversal
T_x:	Transmit
WDC:	Wavelet Detail Coefficients

CHAPTER 1

INTRODUCTION

1.1 Introduction of NDE

The term "Non-destructive testing, evaluation, and inspection" (NDT/NDE/NDI) refers to a variety of analysis techniques to determine the quality or structural integrity of a material or component without influencing the serviceability of the object under test (OUT) [15]. Research in NDE technologies has rapidly evolved over the past years. This is due to their essential role not only in diagnostic maintenance but is also emphasized in other supplemental roles such as prognostic maintenance, health monitoring, quality assessment, and manufacturing processes. The application of these technologies has improved the quality and the reliability of the structures and systems that are being used in various fields, such as aerospace, energy, automobile, and civil infrastructures. Unlike the destructive methods that can be only performed on a limited number of samples and cause damage to them, NDE methods are able to provide the information of the samples that are actually being put into service[16].

The basic principle of NDE is applying energy that will interact with the OUT and not alter the object's function. A generic NDE system usually includes excitation source(s), transmitter/receiver, and a data acquisition device. The transmitter will inject the energy generated by the excitation source into the OUT. The signal captured by the receiver will be influenced by the interaction between the energy and the testing sample. The response signal recorded by the data acquisition device will contain information on potential defects (location, size, and shape) and/or the material's properties.

1.2 Motivation

A rapid pace of technological advances has been observed due to continuing discoveries and applications of materials exhibiting novel or enhanced properties which offer superior performance to conventional products and processes. When these materials and parts are used in some critical applications and directly impact safety and success, it is crucial to ensure their quality and reliability.

The following subsections discuss some of the emerging materials and fabrication methods.

1.2.1 Composite Material

The application of composite materials is rapidly increasing in a variety of industries ranging from aerospace to civil, to fully or partially replacing metal parts in a variety of structures due to their unique properties such as high strength/stiffness-to-weight ratio, high design flexibility, lower material cost, and increased productivity. In spite of having better damage tolerance and corrosion resistance than metals, the presence of defects in composites such as disbonds, voids, or delaminations may significantly affect their strength and integrity, as shown in Fig 1.1. Consolidation of the composite provides an increase in the strength-to-weight ratio. The performance will be negatively affected by the presence of porosity, delaminations, cracks, or wrinkles. Among other factors, the toughness of CFRP composites is influenced by the chemistry as well as the porosity and the resin-to-fiber ratio. Therefore, it is necessary to employ non-destructive evaluation (NDE) techniques in order to ensure the safety and performance of such materials.

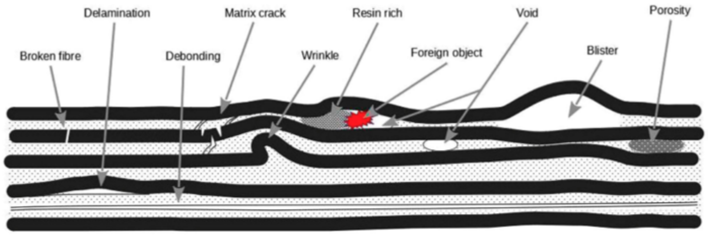

Figure 1.1: Common defects in composite materials [2].

1.2.2 Additive Manufacturing Material

Additive Manufacturing (AM) is the process of building up parts directly from 3D model data by joining materials one layer upon another layer [17]. As opposed to traditional subtractive manufacturing methodologies, which use cutting tools to remove materials from a larger metal, AM prints the component by adding materials together. It allows AM to produce complex geometries and internal features which cannot be manufactured using subtractive methods [18]. In addition, AM uses a computerized 3D model, which allows design optimization and efficient use of raw materials. By eliminating the production steps, AM can reduce material waste, energy, and time costs by up to 90% [19]. According to NASA, [20], AM can save more than eight months compared to traditional manufacturing when building rocket injectors. It is also able to manufacture customized parts according to different demands. The components can be produced directly from the designed 3D model without the need for expensive and time-consuming part tooling and prototype fabrication [21].

With fewer constraints on product design and more flexibility, AM makes it possible to produce a single consolidated object instead of separated parts. Since the late 1980s, the AM has been developed rapidly [22], and it also has been called Rapid Prototyping [23]. 3-Dimensional Printing, Solid Freeform Fabrication, or Desktop Manufacturing [24], which express the characteristics of this method from different aspects. It also uses a wide range of materials such as metals, polymers, composites, and biological tissues.

Although AM is able to offer so many impressive benefits, there are still a lot of technical barriers and challenges that need to be overcome. As a novel technology, it not only redefines the way of manufacturing but also redefines the way of testing and evaluating products. When additive-made parts are used in some critical applications and have a direct impact on the safety and success of a project, it is crucial to ensure their quality and reliability. The Fig1.2 shows the three

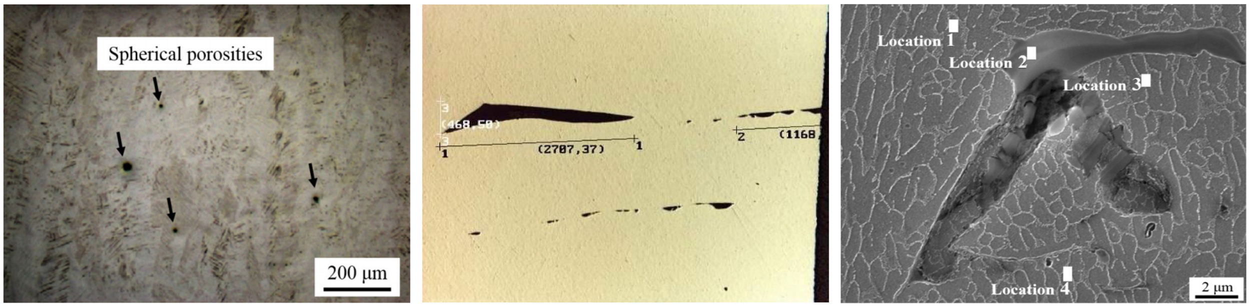

Figure 1.2: Optical image of (a) porosities on the surface [3] (b) bonding between layers [4] (c)Scanning Electron Microscope image of incomplete fusion [5].

common defects of AM fabricated parts. However, the parts produced by AM are often complex in shape and manufactured in one piece directly. These parts usually combine hundreds or thousands of individual layers, which are melted by energy sources and deposited upon each other. Many of the process variables such as printing speed, energy distribution, substrate, and atmosphere will have a complex interaction and influence the parts' quality. Therefore, it isn't easy to test and evaluate AM parts using conventional methods without affecting the part.

1.2.3 Phenotype of the Root in Soil

The phenotype of plants refers to some individual's observable feature. It is dependent on two factors; the genotype, i.e., the expression of the genome, and how it interacts with the environment. Studying the phenotype of plants will provide a better understanding of the interaction between the plants and different environmental factors and plant breeding. As one of the essential organs of the plant, root architecture influences the uptake efficiency of nutrients and water. Improvements to the architecture of roots promise to increase water and nutrient use efficiency but profiling the root phenome (such as its structure and function) represents a significant bottleneck. The opaque nature of soil makes phenotyping root systems in situ challenging compared to analyzing above-ground

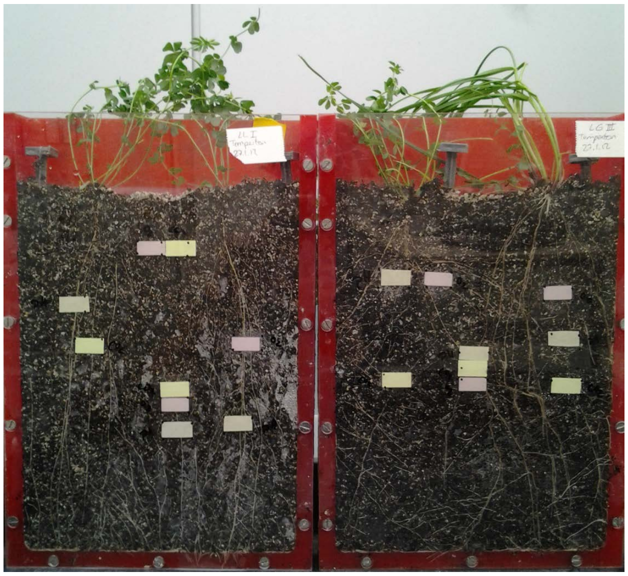

Figure 1.3: Example of rhizotrons which have been used to assess root architecture and distribution in the experimental setup[6].

plant organs. Soil is a very complex medium in terms of energy-material interaction. The soil properties are highly dependent on particle size, porosity, and moisture. The environment of the roots and the complicated growth process make the in-situ and non-destructive root imaging face great challenges, which also raises great research interest. As shown in Fig.1.3, a rhizobox(a box containing the soil and root with an observation window that is transparent or removable for the root inspection) is used to provide some inspection-ability to the root close to the transparent window. However, this method cannot inspect the roots that are covered in the soil.

1.2.4 Complexity of NDE problem

As mentioned in the previous section, non-destructive inspection methods and techniques for post-production quality assurance or in-service inspection are essential for any crucial application.

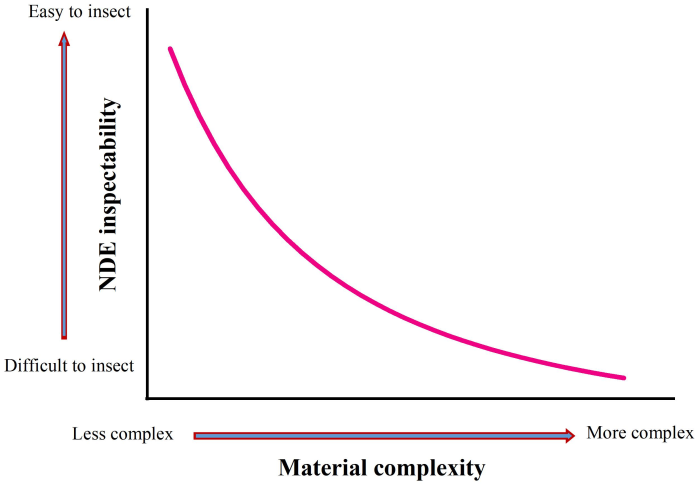

Figure 1.4: Complexity vs. Inspectability.

However, the inspector may deal with different complexity when performing the Non-destructive evaluation. As complexity increases, it becomes more challenging to conduct an inspection. When inspecting structures or components, geometric complexity is one of the primary factors influencing the inspection ability to OUT. Large area coverage is required for the system with a good balance of speed and sensitivity. Complex geometry introduces the need for an NDE system with higher flexibility. Contour following techniques and high-speed data acquisition is necessary to reduce the scanning time for large and complex structures.

The challenges of NDE may also come from the environment, including extreme temperature, visibility, and accessibility. Sub-sea infrastructures (such as communication cables, pipelines, and offshore oil structures) are essential for modern civilization. A boiler that produces steam in the thermal power station is critical for electricity generation. In the event that any of these systems fail structurally, severe damage can be caused to people, the environment, and the economy. However, the inspection of these structures faces difficulties due to the environment and requires the NDE system to be designed and optimized to meet the requirements and constraints.

Some other factors of the NDE complexity include the complex property and complex numerical model of the OUT. The desired property of the OUT may not be able to be obtained directly when performing the NDE. The property of interest may be complex and related to multiple other parameters. Numerical models are usually employed to provide a better understanding of materials' properties and assist the design of the NDE system. In some applications, it also faces significant challenges for accurately describing the NDE process in the numerical model.

1.3 Statement of Problem and Organization of the thesis

The objective of this work is to develop a reliable NDE framework that able to characterize the materials with some of the aforementioned complexities. The studies will mainly focus on the electromagnetic methods, design/optimize the sensing system, and processing of the data to utilize information from multi-frequency and multi-parameter testing. Other NDE or destructive evaluation methods will also be used to provide reference information. As shown in Fig.1.5, the first step is to understand the mechanisms involved in the damage and failure of the material or structure. With the information for the constraints and sample properties, the NDE system and the sensor will be designed accordingly with the help of the numerical model. The experimental results will be used to validate the simulation model and improve the design of the NDE system. Data processing methods will be applied to reduce the noise and extract the demanding information.

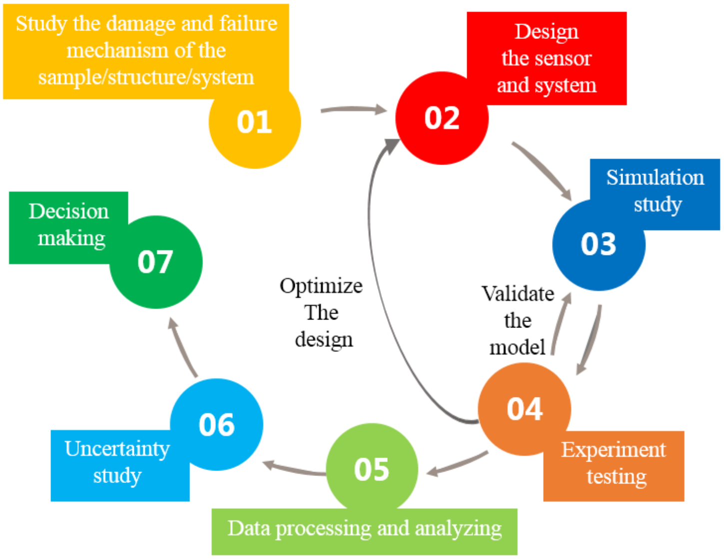

Figure 1.5: The flowchart of the NDE framework.

In this thesis proposal, the works will be discussed in the following chapters:

1.3.1 Multi-modality strain estimation using a rapid near-field microwave imaging system for dielectric materials.

Strain distribution is an important indicator of stress concentration, damage initiation, and evolution. Many dielectric materials sustain very large strain before failure. In Chapter 2, a near-field microwave high-resolution imaging (NMHI) system is presented to estimate very large deformation. The sensitivity of the microwave imaging system to the dielectric property and geometric changes have been utilized in the present work. A multi-modality data fusion technique is applied to experimentally evaluate the strain in the ASTM-D638 standard dog bone structure made of PA-11 material. Plastic strain in the range of 0.3-0.7 of the maximum strain has been successfully correlated to the microwave probe response in PA-11 materials. The comparison of strain distribution obtained from NMHI and digital image correlation (DIC) indicate the potential of NMHI as a fast, non-contact method to estimate large mechanical strain.

1.3.2 Root phenotyping using ultra-wideband microwave imaging system

The root is a vital organ for the plant's growth and health. The opaque surrounding environment of the roots and the complicated growth process make the in-situ, and non-destructive root imaging faces great challenges, which also raise great research interest. Existing methods for root imaging are either unable to provide high-precision and high accuracy in-situ detection or change the surrounding root environment and are destructive to root growth and health. Thus, an ultra-wideband microwave scanning method that uses time reversal is proposed in Chapter 3 and developed to achieve the in-situ root imaging nondestructively. An electromagnetic numerical model that simulates the transmission signal of two ultra-wideband microwave antennas has been studied to verify the method's feasibility. The simulated signal of roots with different shapes shows the proposed system's capability to measure the root size in the soil. The reconstruction from both simulations and experimental measurements provide an accurate size estimation of the carrot in the soil, which indicates the system's potential for root imaging.

1.3.3 NDE System Design for the Boiler Inspection Robot

Many constraints needed to be considered when designing the NDE sensing system for the robot. The sensor's footprint is limited by the design of the robotic system as well as the complexity of testing structures. The allowable maximum power consumption of the entire system is constrained by the available power supply unit on the robot. There are also many environmental conditions that could affect the NDE results obtained from the robotic actuating and sensing. Such would add inevitable uncertainties toward the acquired data or restrict actuation access, in turn, lowering the fidelity and resolution of NDE data used for further damage assessment and analysis. In Chapter 5, NDE sensors were customized to fit the robotic system and workspace environment for power plant boiler inspection to overcome these aforementioned challenges and obtain optimized sensing outcomes. These optimizations lead to a low-cost, lightweight, non-contact, and simplified NDE setup

CHAPTER 2

MULTI-MODALITY STRAIN ESTIMATION USING A RAPID NEAR-FIELD MICROWAVE IMAGING SYSTEM FOR DIELECTRIC MATERIALS

2.1 Introduction

Advances in material science and manufacturing have produced complex engineering structures that can operate in fatigue and/or harsh environment. Infrastructure involving these structures is growing quickly, for which rapid inspection techniques are needed for their periodic maintenance. This is critical for ensuring the quality of service and reliability of structures in harsh environments. Thus, rapid nondestructive evaluation (NDE) technologies that can detect and characterize damage is of great interest at present [25]. Strain measurement is one of the essential elements in materials or structural testing. Knowing the distribution of strain and its value at the critical zones of the structure leads to important indicators for evaluating the strength and life of the structure [26]. Damage initiates in a structure by permanent deformation accompanied by elastic and plastic strains. Plastic strain occurring in the structure indicates an alarming situation that cannot be neglected. In this chapter, a detection of deformation involving residual elastic strain and plastic strains has been studied. The scope of the work has been limited to a very large deformation occurring in the dielectric materials. Some of the contents and results in this section have been presented in [27].

2.2 Prior work in Strain estimation

The current strain measurement methods for dielectric materials can be divided into contact types and non-contact types[28]. The contact-based methods include the ultrasonic method is one of the most mature and widely used technologies [29, 30]. However, its use is complicated on the structure with special geometry, surface cleaning to ensure proper coupling between the sensor and the OUT, and requires skilled personnel to perform the NDE. Also, contact-based ultrasonic probes involve the application of gel and consume lots of time. The non-contact modes includes photoelastic method[31], Digital image correlation(DIC) [32, 33], X-ray[34, 35], noncontact ultrasound [25], capacitive [36, 37] and microwave techniques [38]. The DIC technique is a cost-effective and full-field optical measurement method, which obtains the strain data by relating different digital images taken at various stages of the test and tracking blocks of pixels in the images [39, 40]. Although DIC offers accurate strain information of the object-under-test (OUT), it requires continuous data acquisition during the deformation. Thus it is limited to small structures for real-time monitoring and is not applicable to NDE [41]. The X-Ray system is hazardous, expensive, and not practical for field testing. Therefore, a strain estimation method of dielectric material using the NMHI technique is investigated, followed by multi-modal correlation analysis between DIC and NMHI data. The near-field microwave imaging method is a promising nondestructive evaluation technique that can provide a quantitative measure of the surface and sub-surface profile of lossless or low-loss dielectric materials [42, 43, 44, 45]. Unlike the far-field technique [46], the resolution of the near-field measurement is not constrained by diffraction limits since it is determined by the probe's aperture size. Thus, it is capable of providing sub-wavelength resolution. The sub-wavelength resolution microscope was first proposed by Synge in [47], with experimental designs reported in [48]. Since then, a lot of research has been focused on improving and developing various designs for a microscope scanning system. Cho et al. achieved millimeter level resolution with frequencies around 1 GHz by using coaxial resonators [49]. Reducing the aperture size by using a sharp, probing tip achieved a spatial resolution of 100 nm by Gao et al. [50]. Bakli et al. presented a scanning system that combines a vector network analyzer and a high precision interferometer which provides broadband capabilities, and high measurement accuracy [51].

2.3 Nearfield Microwave Imaging

A near-field microwave imaging system consists of either a single transceiver [52], or multiple arrays of probes [53], which illuminates the OUT and measures the localized response from the material [54, 55]. The response varies with the electrical properties of the material. However, to

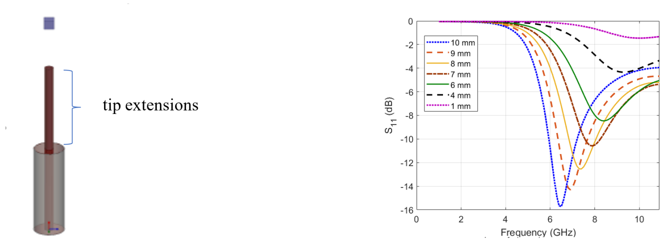

(a) Probe

(b) Reflection coefficients for the coaxial probe with varying tip extensions

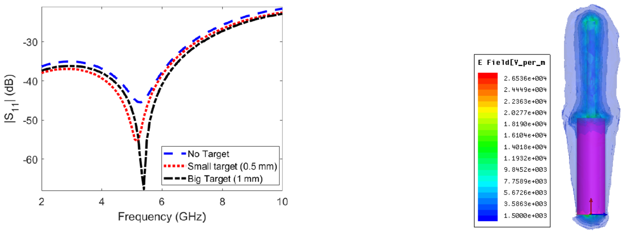

(c) Reflection coefficients for the coaxial probe in presence of samples with different sizes

(d) Radiated near E field for the probe

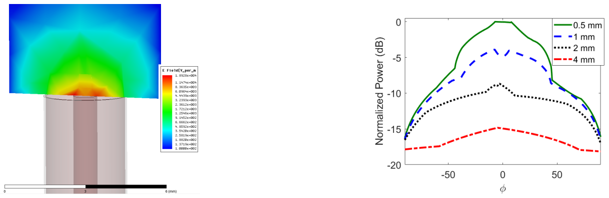

(e) Cross section of radiated near E field

(f) Near E field radiation pattern of the probe

Figure 2.1: NMHI Probes and Frequency response.

achieve high-resolution images, the separation between the tip of the near-field antenna and the sample's surface has to be small and stay constant. The precision of that distance will significantly influence the accuracy of a near-field imaging system.

Some of the conventional probes used in NMHI are aperture in a waveguide, scanning tunneling microscopy, atomic force microscopy, and open-ended transmission line [56, 57, 58, 59, 60]. Researchers have extensively studied these probes and used them in several industrial applications. Experiments have been conducted using an open-ended coaxial probe with an extended copper tip, operating at a narrow band frequency of around 7 GHz (λ= 42.8 mm). A standard RG58 coaxial cable is used to fabricate the probe. The outer copper section, along with the dielectric enclosing, is removed to create an extended copper tip, as shown in Fig. 2.1(a). Since the impedance of the coaxial probe is matched to 50Ω, no additional matching circuits are required. Electromagnetic fields radiate out from the extended tip of the coaxial probe with monopole antenna-like radiation. The resonant frequency of the probe is determined by the length of the extension, similar to a quarter-wave monopole. Increasing the length of extension decreases the resonant frequency of the probe, as shown in Fig. 2.1(b). The coaxial probe provides a wider band of operating frequencies and eliminates the matching circuit requirement.The change in the reflection coefficients of the coaxial probe varies due to perturbation in electromagnetic fields due to the presence of a target or a defect inside a sample. A simulation is conducted with the coaxial probe placed 0.5 mm away from a GFRP composite sample with a 2 mm circular hole defect. The effect of the defect on the reflection coefficients is shown in Fig. 2.1(c).

The radial component near E-field of the monopole antenna can be expressed as [61]:

$$E_r = -j\eta \frac{(I_0 l e^{-jkr})}{(2\pi k r^3)} cos\theta, \tag{2.1}$$

where I_0 is the current, l is the length of the antenna, η is the intrinsic impedance of the medium, and The wavenumber $k = 2\pi/\lambda$. The simulated far-field radiation pattern shows monopole-like radiation with nulls at the center for E-plane and omnidirectional radiation in H-plane at $f_r = 6.5Ghz$. The field decays very fast ($O(1/r^3)$ and is a function of the wavelength ($\lambda = 2\pi/k$), antenna length l and η. Higher frequency provides finer resolution, however reducing the near field range ($R = 0.62\sqrt{D^3/\lambda}$, D is the maximum overall antenna dimension), thus requiring smaller lift-off distances. The simulated E-field distribution around the probe, depicted in Fig. 2.1(d) at f_r shows fields spreading along the tip region and radiating from the tip edges. Fig. 2.1(e) presents the magnitude of the simulated radiated electric fields in the E-plane at f_r. As seen from Figs. 2.1(e, f), the fields are maximum at the center but decay rapidly for increased lift-off distances (~15 dB for 4 mm). This is because the lift-off distance due to surface variance significantly impacts capacitive coupling between the probe and the sample. Thus, the choice of frequency is based on a trade-off between resolution and lift-off distance. The near field radiation pattern for the probe was computed using HFSS at different distances from the apex of the antenna and shown in Fig. 2.1 (f).

In accordance with (1), it is observed from Fig. 2.1(f) that the field decays at a rate of ($O(1/r^3)$ where r is the distance away from the probe.

2.3.1 Background and Theory

The reflection coefficient of the microwave probe changes due to perturbation in fields in the object under test. The presence of any anomaly (void or inclusion) and change in the geometry in the sample has direct effects on the complex permittivity of the material. The complex permittivity also changes with elastic and plastic strain [62, 63, 64]. This property can be used to measure the strain in the structure made of dielectric materials. It is found to also change with the temperature, frequency, and electric field [65, 66, 67]. So fluctuation of temperature and electric field has to be minimized when performing the microwave's nondestructive evaluation. The complex relative permittivity changes the net coupling capacitance between the probe and the object, as shown in Fig. 2.2.

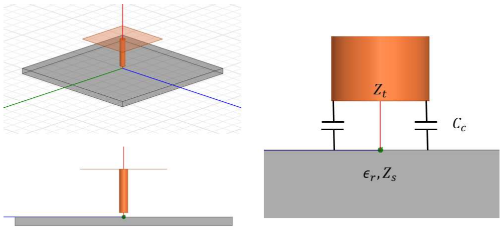

Figure 2.2: Nearfield microwave probe model with interaction between the probe tip and the Object Under Test.

The feed signal used for imaging is a continuous sinusoid wave with amplitude A_1 as expressed in Eq. 2.2.

$$T_x(t) = A_1 \cos(2\pi f t) \tag{2.2}$$

The simplified model assumes no reflections from the feed point and only considers the change in capacitance due to material permittivity. Changes in tip capacitance introduce reflections at the end of the transmission line. The reflection parameter can be represented using Eq. 2.3, and can be considered as the reflections are only due to the change in impedance of the material.

$$\Gamma = \frac{Z_{st} - Z_0}{Z_{st} + Z_0} \tag{2.3}$$

where $Z_0 \sim 50\ \Omega$ and Z_{st} is the impedance of tip - sample interaction. The reflected signal is a function of transmitted signal and reflection coefficients, shown in Eq. 2.4.

$$R_x(t) = \Gamma T_x(t) \tag{2.4}$$

The reflected signal can be probed using a directional coupler having a coupling factor β, and the probed signal can be mixed with the transmitted signal to get the net phase change. The phase shift in the received signal ϕ is shown in Eq. 2.6.

$$O\left(t\right) = \alpha T_x\left(t\right) \beta R_x\left(t\right) \tag{2.5}$$

$$O(t) \approx \Gamma A_1^2 \left[\cos\left(4\pi f t + \phi\right) + \cos\phi\right] \tag{2.6}$$

The frequency components are filtered out, and only DC components are measured. The output is seen as a function of the change in material properties in the form of Γ and ϕ.

$$O_{DC} \approx \Gamma A_1^2 \cos\phi \tag{2.7}$$

The near-field microwave imaging measures phase information at different points over the material according to Eq. 2.7. The scanning controller moves the material holding platform in the raster scanning mechanism and covers all the points in a predefined area.

2.3.2 NMHI Setup

The block diagram of implemented setup is shown in Fig.2.3 (a) with the developed RF circuit in Fig. 3(b). A 7 GHz RF source generator is used to feed the near-field microwave probe. The low output of the source is amplified to +24 dBm, and a 3 dB RF splitter is used to divide the amplified signal into a feed and a reference signal. The directional coupler is connected to the feed signal coming from the splitter and is also used to probe the reflected power. The reflected signal is mixed with the reference signal to get any changes in phase according to the changes in the properties of the OUT.

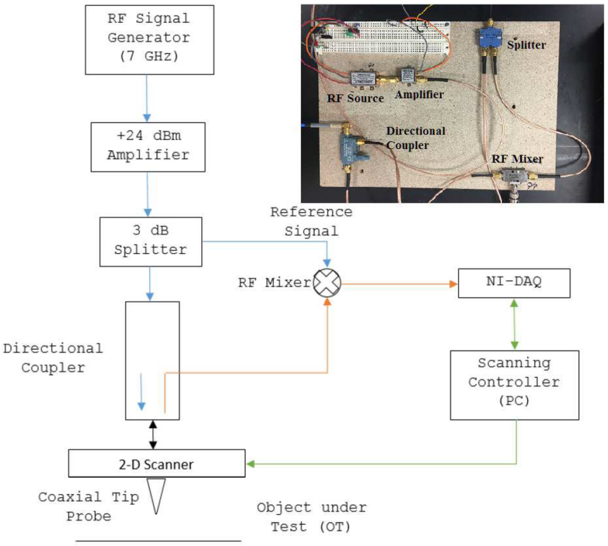

Figure 2.3: Near-field microwave microscopic imaging system and block diagram.

The probe used for imaging is a coaxial cable with an open-ended copper tip due to its simple design, easy availability, and wideband frequency response. The experiments are performed by keeping the tip perpendicular to the object, where the fields are stronger and localized. The minimum step size or the finest resolution of the scanner is 0.5 $mm (0.01\lambda)$.

The object used to test the capabilities of NMHI is shown in Fig.2.4 (a) and Fig.2.4 (c). A polyamide (PA-11) rectangular sheet and an aluminum calibration sample are used to test the system's capabilities. The PA-11 sample has $3.26\lambda \times 2.37\lambda \times 0.18\lambda$ length, width and thickness respectively. Two square defects are machined on one side of the sample with $0.89\lambda \times 0.89\lambda \times 0.13\lambda$ and $1.18\lambda \times 1.18\lambda \times 0.13\lambda$. The object is scanned from the opposite surface of the sample. The aluminum calibration sample is of size $4.15\lambda \times 4.15\lambda \times 0.08\lambda$, with different machined defects of shape and size.

The predefined area of interest and the spatial resolution is used to initialize an empty image matrix, and a raster scanning algorithm is set to fill the whole matrix. The measured response from the PA-11 sample with sub-surface defects is shown in Fig.2.4(b). Both squares are detected with

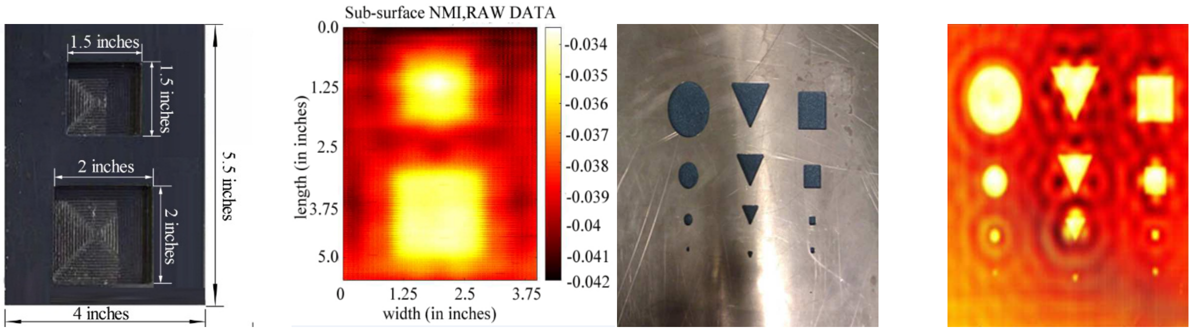

(a) Polyamide (PA-11) sample with engraved defects (b) PA-11 NMHI raw data (c) Aluminum Calibration Sample (d) Aluminum NMHI raw data

Figure 2.4: Nearfield microwave microsopic imaging of a plastic (Polyamide) sample with sub-surface defects.

accurate size information. It shows the capability of the system to image subsurface defects. The results of the scan of the Aluminum sample shown in Fig.2.4(d) show the millimeter resolution capability by detecting all the small defects and the ability of the system to accurately image the profiles (square, triangular and circular) of the defect.

2.4 Mechanical Properties Estimation Using Multi-modal Data Fusion

The tensile test-based studies were performed on a number of Polyamide 11 dog-bone samples by employing an integrated experimental and numerical simulation. A numerical simulation model is developed for strain estimation using COMSOL Multi-physics software. The material model for the mechanical analysis was calibrated by utilizing the data obtained from the tensile test. The shape of the specimens complies with the ASTM-D638 standards, as shown in the Fig.2.5. Using the Universal Testing Machine and a high-resolution camera, the specimens are subjected to tensile stresses to produce 30%, 50% and 70% of maximum tension before the specimens break. DIC technique was used to obtain the local strain and displacement during the tensile testing, and the results from the DIC analysis were compared with that from the numerical simulations.

The von Mises strain is a widely used criterion for studying the ductility, malleability, and yielding of the material [68]. As the strain number obtained from the DIC method is a uniaxial value, the von Mises strain allows the comparison between the 2D strain property of the OUT with

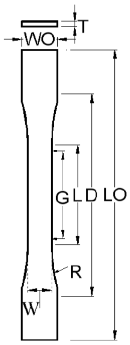

Dimensions (see drawings)	mm
W-Width of narrow section	13
L-Length of narrow section	57
WO-Width overall	19
LO-Length overall	165
G-Gage length’	50
D-Distance between grips	115
R-Radius of fillet	76
T-Thinkness	3.2

Figure 2.5: The shape of specimen under the tensile test.

the NMHI data.

The Von Mises strain is given by

$$\varepsilon = \frac{1}{3}\sqrt{2(\varepsilon_{xx}-\varepsilon_{yy})^2+\varepsilon_{xx}^2+\varepsilon_{yy}^2}, \tag{2.8}$$

where ε_{xx} and ε_{yy} are the local strains along x and y direction measured by DIC.

The elongation are performed at ASU PARA lab on specimens at at a speed of 0.2 in/minute, with data acquisition frequency of 10 Hz. The local Von Mises strain for the 70% and 30% elongated specimens are shown in the Fig. 2.6.

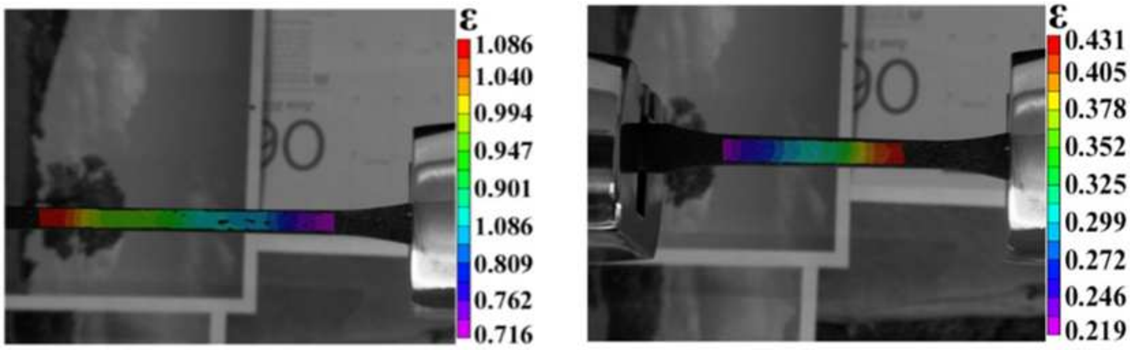

Figure 2.6: The Von Mises strain of the 70% (left) and 30% (right) elongated specimens obtained by DIC (experiment data is collected by ASU PARA Lab).

According to the dimensions mentioned in Table.1, the 2-D Von Mises strain is simulated for specimen with 70% elongation. As the basis for the strength calculation, the stress-strain relationship of the PA11 sample is obtained from experimental data. The test curve of the PA11 uniaxial tensile deformation is shown in Fig.2.7. It can be seen from the figure that when stress is less than or equal to 5 ksi (point a), the stress-strain relationship of PA11 conforms to linear change and is in the elastic phase. When it is greater than 5 (ksi), it enters the yielding stage. When the strain exceeds 0.1 (point b), PA11 enters the strengthening stage, and the PA11 material test piece can produce large plastic deformation. When the strain reached 0.6, the deformation resistance further increased until the d point. The material properties, such as Young's modulus (Es = 147.79 ksi = 1019 Mpa) and Poisson's ratio (Poisson ratio = 0.32), are assigned.

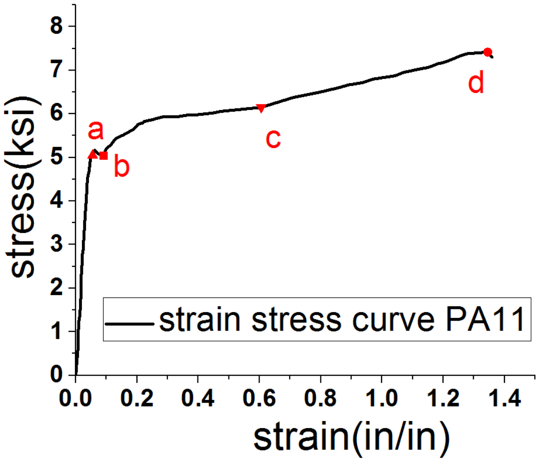

Figure 2.7: Strain-Stress Curve of PA-11 specimen (experiment data is collected by ASU PARA Lab).

The simulated result and the strain along the middle section line are shown in Fig.2.8. It can be observed that strain is constant throughout the narrow section.

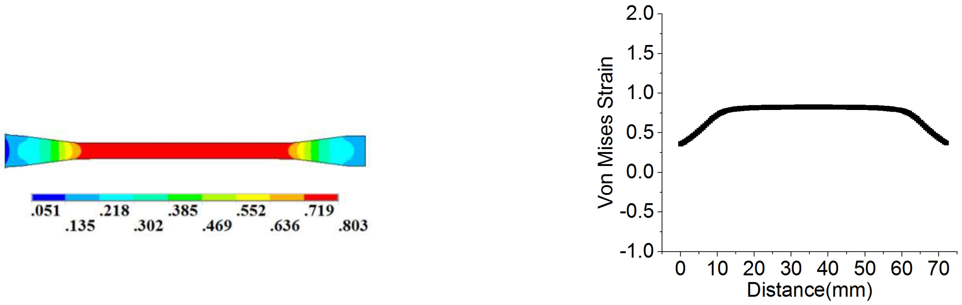

Figure 2.8: Von Mises strain simulation of the specimen with 70% elongation.

Contrary to the simulation results, the local strains along the x-direction of the specimen increase from left to right. The difference between simulation results and experimental data may be due to the non-idealities of the specimens. In order to validate our hypothesis and have the simulation results comparable to experimental data, the widths of both ends of the narrow section are assigned with different dimensions in the simulations. The dimensions are estimated according to the dimensions of specimens after the tensile tests. The original specimen width W_o is found using Eq.2.9

$$W_o = \frac{W_x}{\left(1 - \varepsilon_{yy} + \mu\varepsilon_{txx}\right)}, \tag{2.9}$$

where W_x is the width of the specimen after stress unloading and μ is Poisson's ratio. The axial elastic strain ε_{txx} is calculated as:

$$\varepsilon_{txx} = \frac{l_o + l' - l_x}{l_o}, \tag{2.10}$$

where l_o is the initial length of the specimen before loading, l' is the elongation, l_x is the length of the specimen after unloading stress. Based on the width variation of the narrow section of the specimen, the simulation is updated. The comparison between the modified simulation and experimental data from DIC is shown in Fig.2.9. It can be seen that the strain output from the simulation and DIC experiment match closely. The Von Mises strain decreases along the specimen length for both simulations and experiments. The improved ANSYS model provides a testbed for optimization and data validation.

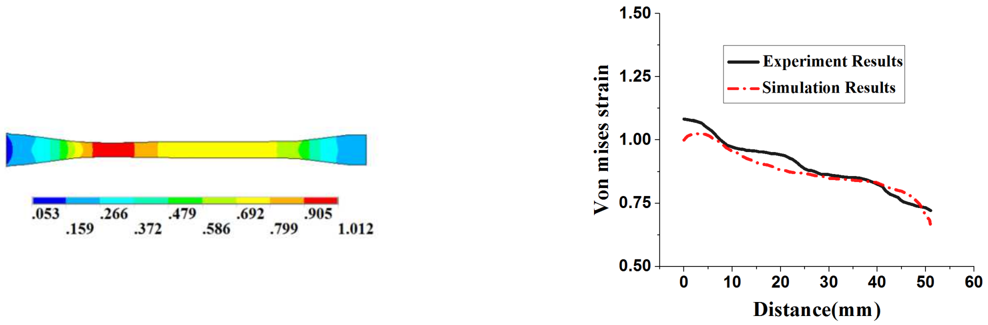

Figure 2.9: (a).Von Mises strain from simulation (b) Comparison between experimental results and simulation.

A correlation between DIC and NMHI data is performed to demonstrate the capability of NMHI for accurately estimating the mechanical properties. The comparison between the processed NMHI data and the measured strain for different elongations of the specimens is shown in Fig.2.10. Due to the difference in acquisition units for both NMHI and DIC, the plots are normalized for comparison.

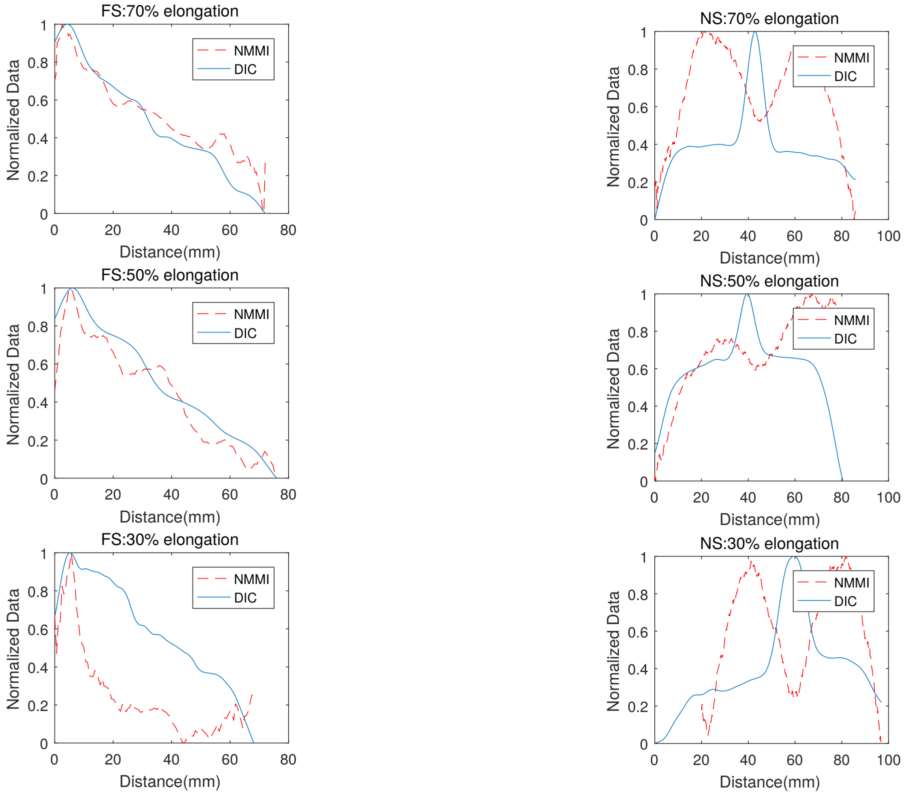

(a) (b)

Figure 2.10: Comparison between the Von Mises strain and NMHI scanned data along the section line for the (a) Full specimen and (b) Notched specimen with 70% 50% and 30% elongation.

As shown in the Fig. 2.10 (a), the curves which represent NMHI data measured from the specimen decrease with the Von Mises strain. The best agreement is shown in the plot of 70% elongation, whereas discrepancies between the two estimates are seen in 30% elongation. For the 30% elongation, there is a significant deviation between the two approaches, but they exhibit similar trends. It can be seen that NMHI data has better agreement with DIC under more significant elongation or when the plastic strain is higher. This is reasonable since the NMHI data is acquired after unloading the specimens. Von Mises strain is a total strain that is composed of elastic and plastic parts. At 70% of elongation, the plastic strain dominates, which results in a permanent change in the dielectric properties. This is measured by the NMHI system with a small percentage of elastic residual strain arising from local inhomogeneity. Whereas the DIC data captures both elastic and plastic strain. The elastic strain recovered over the length of the specimen is constant at large plastic strain resulting in a closer match at 50% and 70% elongation. At 30% elongation, the elastic strain dominates, resulting in the discrepancy between the NMHI and DIC data. The DIC data measures this dominating elastic strain as well as plastic strain. The initial 30% elongation causes nonlinear plastic strain distribution in the sample from the fixed ends to the center of the specimen. The DIC data measures the major elastic strain in a linear loaded condition. Whereas the NMHI data is nonlinear, indicating the nonlinear variation of plastic deformation across the specimen length. The data in Fig.2.10 (b) represents NMHI's and DIC's measured strain data for NS. The NMHI data doesn't follow a close trend with DIC's data at the center due to an extra drilled hole on the specimen. The drilled hole perturbs the fields of the NMHI probe and gets significantly more responsive to the shape of physical structure than its dielectric properties. It can be seen that NMHI data follows the stress at the edges as it is the scanning data away from the hole.

2.5 Discussion

The increase in the strain causes the electrical property, sample's geometry (width and thickness) and the microstructure to change. The NMHI scanning system will capture all these changes and be reflected in the scanned data. In order to study the change of the material's microstructure under the different strain and how it will affect the material's electromagnetic properties, multi-modality simulations have been employed.

As shown in Fig.2.11, a coaxial antenna is simulated using a monopole antenna mode to obtain the full field scanned result. The length of the antenna is 1/4 λ, and the radius is 1/40 λ which are same as the experiment. The antenna is fixed and points to the middle of the specimen. An air layer with a radius of 203 mm and a height of 133 mm is introduced. First, the tensile test simulation calculates the strain and displacement data. Then, according to the information obtained, the electromagnetic simulation was run to estimate the near-field microwave scanning result. The plot

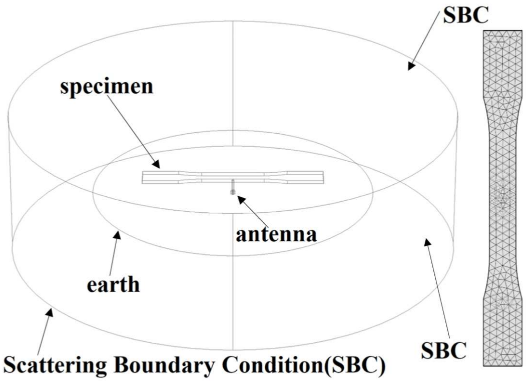

Figure 2.11: Multi-modality simulation in COMSOL showing the specimen model, meshing & Boundary Conditions.

of normalized probe response with the von Mises strain that only considers the effect of geometry change (thickness and the width) is shown in Fig.2.12. The two ends of the curve meet due to the normalization.

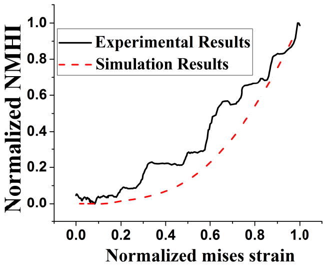

Figure 2.12: Comparison between the NMHI scanned data and simulation of sample only considering the geometry change.

Some huge discrepancies can be observed between the simulated result and experimental data, indicating the necessity of considering the material's electromagnetic properties due to the microstructure change.

As shown in Fig. 2.13, the permittivity is adjusted according to the strain using Eq. 2.11

$$P_i = P_O - R_s \times P_O \times \frac{S_i}{S_{max}}, \tag{2.11}$$

Where S_{max} is the maximum strain and P_O is the permittivity of the materiel. R_s is the changing ratio of the permittivity along with the strain. A much better fit is found in the simulated result than in the model that only considers the geometry change.

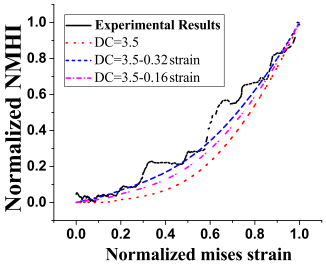

Figure 2.13: Comparison between the NMHI scanned data and simulation of sample with adjusting the parameter according the strain.

In order to use the NMHI data to predict the strain, the relationship between the Von Mises strain measured using DIC and dielectric changes measured using NMHI is illustrated by a normalized comparison plot and displayed in Fig. 2.14. A piecewise regression of the data is done by the Quasi-Newton Methods [69, 70], as shown in the Algorithm. 11.

Algorithm 2.1 Quasi-Newton Algorithm

```
1:  Input: X, Y, target error $\varepsilon$.
2:  Set: y $= \varphi(X, \beta) + E$
3:  Init:$\beta_0 = (\beta^1_{(0)}\beta^2_{(0)} \cdots\cdots \beta^p_{(0)})$
4:  Set $k := 0$   $B_0 = I$   Set $f(\beta) = \sum_{i=1}^{n} (y_i - \varphi(X, \beta))^2$
5:  while $g_k >= \varepsilon$ do
6:      $g_k = \nabla f(\beta_k)$,$d_k = -B_k^{-1} g_k$
7:      $\lambda_k = \arg min f(\beta_k + \lambda d_k)$
8:      $S_k = \lambda_k d_k$,$\beta_{k+1} := \beta_k + S_k$, $z_k = g_{k+1} - g_k$
9:      $B_{k+1} = B_k + \frac{z_k z_k^T}{z_k^T S_k} - \frac{B_k S_k S_k^T B_k}{S_k^T B_k S_k}$
10:     $k := k + 1$
11: end while
```

As shown in Fig.2.14 (a), when the normalized Von Mises strain value is less than 0.5, the slope of the regression curve and NMHI-strain (DIC) curve is relatively small. This indicates that when the strain is small, the deformation does not significantly affect dielectric properties since the elastic strain is completely recovered. When the normalized Von Mises strain value is greater than 0.5, the data of the NMHI and the DIC are consistent in trend (2.10) for which the NMHI-DIC curve has a very good agreement with the regression curve. The regression curve has been evaluated by the error histogram shown in Fig.2.14 (b). The data from 70% elongation has errors that are within

5%. The regression errors for 30% elongation are larger as expected since the regression is not good when the strain is relatively small. The measurement of material property change with the applied elastic and plastic strain opens the options for several novel applications. These applications are (1) the detection of permanent deformation in dielectric materials like polymers, composites, and nano-composites for NDE applications, (2) detection of manufacturing defects and damages in dielectric components for NDE applications, (3) mounting the probe permanently to detect the material changes in-situ for structural health monitoring (SHM) of structures made of dielectric material.

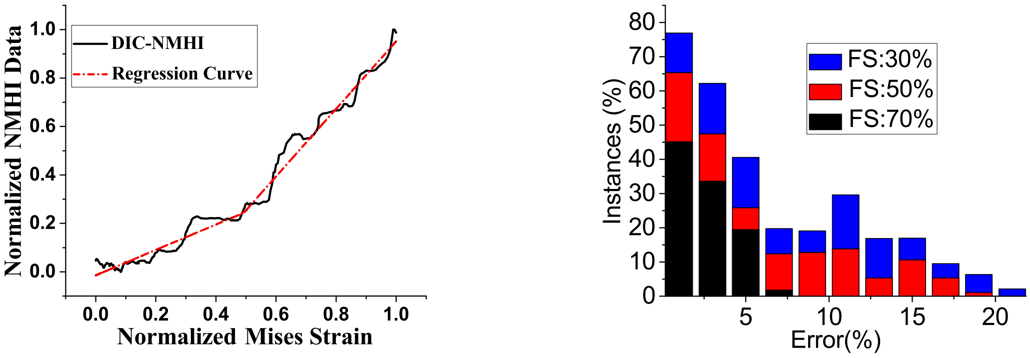

(a)

(b)

Figure 2.14: The plot of (a) DIC strain against the NMHI data with double-fold regression (b) The regression error for 70% 50% and 30% elongation.

CHAPTER 3

ROOT PHENOTYPING USING ULTRA-WIDEBAND MICROWAVE SYSTEM

3.1 Introduction

As one of the plant's three major organs, the root system provides functions central to plant fitness, such as nutrient absorption, fixation, water transmission, synthesis, and storage [71]. The spatial distribution of roots in the soil directly affects the growth and health of plants. In addition, root systems transfer carbon, which is captured from the atmospheric CO_2 by plants, to soil and aid long-term soil carbon storage [72]. A better understanding of root phenotype in situ and non-destructively is important for the research of soil and plant science, earth system science, and others. Some of the contents and results in this section have been presented in [73].

Much research has been done on the plant's aerial parts' structure and function and has made remarkable progress. However, because the root system generally grows in dense, opaque soil, it is difficult to observe it visually or optically [74, 75, 76]. Since 1727, traditional root phenotyping methods are usually destructive, time-consuming, and low-resolution, such as excavation methods[77], pinboard method[78], and trench profile technique[79]. Root imaging method became the main root phenotype method since the introduction of the glass pane method in 1873[80], which is achieved by observing and drawing the root color, size and shape by humans and can't phenotype the root growth accurately. Bates[81] updated the glass pane to glass tube method to better apply it to in-situ root phenotyping. Neutron radiography was proposed and applied to obtain the root growth image[82] in 1985. However, the long-term radiation effects on the plant root growth and the complexity and inconvenience of the equipment make the neutron radiography method inapplicable for in-situ root phenotyping. Since 2000, high-precision optical instruments and digital imaging methods have greatly improved the accuracy of root imaging technology and made non-destructive root phenotyping possible. X-ray computed tomography uses high-energy photons to scan the root and reconstructs the root image using the decayed X-ray signals detected by the detector[83]. X-ray computed tomography method can achieve non-destructive, high resolution, high accuracy and fast 3D root phenotyping[84, 85, 86]. However, the expensive and non-portable nature of the X-ray makes this method ineffective for in-situ root phenotyping. In addition, the X-ray computed tomography is limited in recording the root growth [87]. The Magnetic Resonance (MR) method has similar advantages and disadvantages to the X-ray computed tomography method, except for the lower resolution and shorter imaging time[88]. MR imaging is mainly dependent on the water content of the root, so its accuracy may be influenced by the plant type and soil moisture[89] in root imaging. Computed tomography (CT), and position emission tomography (PET) have ionization radiation and can alter root development [90]. A laser root scanner can provide precise 3D measurements non-destructively, but it is time-consuming and expensive[91]. According to the characteristics of the laser, it can only be used when the root is growing in a transparent medium. The confocal laser scanning microscopy[92], cameras[93, 94], fluorescence techniques[95, 96], and hyperspectral imaging method[79] are all limited to real soil as the laser scanner do. The non-invasive and non-contact thermoacoustic sensing and characterization of the plant is ongoing research, which is still limited by using the agarose[97]. The advantages and limits of existing root phenotype methods are summarized in Table I.

Terahertz (THz) imaging is a powerful technique for subsurface imaging of objects and roots in soil [98]. The applicability in the field is limited as its wireless band exceeds the 802.11b protocol. Scattering, absorption, and lesser penetration depth are additional hurdles in the implementation. The unavailability of sources, detectors, and modulators at affordable prices cannot commercially make this technology available to the users. The microwave imaging method is a promising nondestructive evaluation technique that can quantitatively measure the lossless or low-loss dielectric materials profile. It has shown great promise in a wide range of applications, including but not limited to imaging of composite structures [99] and low-dielectric-contrast media [100]. The Microwave NDE method has been used for testing voids, delamination, porosity, etc., in dielectric materials, including polymers, ceramics, plastics, and their composites [27]. Microwave has also been used in determining soil moisture in rhizoboxes [101]. A microwave resonator system

Method name	**Advantage**	**Limit**
Excavation methods[77], pinboard method[78], trench profile technique[79], glass pane/tube method [80, 81]	Easy and cost effective method	Destructive, time consuming, may affect and limit the growth of the root, low accuracy and low-resolution
Neutron radiography[82]	Provides root image	Destructive, inapplicable for in-situ root phenotype
X-ray computed tomography[83, 84, 85, 86, 87]	Non-destructive, high resolution, high accuracy, and fast 3D root phenotype	Expensive, destructive, non-portable, ineffective for in-situ root phenotype
Magnetic resonance (MR) method[88, 89]	Non-destructive, high accuracy and 3D root phenotype	Lower resolution and longer imaging time compared to the X-ray method. MR dependents on the water content of the root, so its accuracy may be influenced by the plant type and soil moisture
Laser root scanner[91]/confocal laser scanning microscopy[92]	Provide precise 3D measurements non-destructively	Destructive, can only be used when the root is growing in a transparent medium, requires longer imaging times, expensive
Cameras[93, 94]	Provide precise images non-destructively and fast	Can only be used when the root is growing in a transparent medium
Fluorescence techniques[95, 96]	Provide precise measurements	Destructive, can only be used when the root is growing in a transparent medium
Hyperspectral imaging method[79]	Discriminates between living, senescent and dead roots, leaf debris and soil	Can only be used when the root is growing in a transparent medium
THz imaging method [98]	High resolution images, detects and identifies roots and objects buried in soil	Scattering, absorption and radiation issues, and unavailability of hardware for commercialization

Table 3.1: Advantages and limits of existing root phenotype methods.

is verified to have the ability to determine the plant biomass non-invasively [102], while it lacks the ability of root phenotyping. Non-contact inspection and the ability to penetrate dielectric materials are two of the most important microwave NDE attributes and make it suitable for the in-situ real-time monitoring of plant roots. Therefore, a microwave scanning method that uses Time Reversal (TR) is investigated for its potential application as a real-time and in-situ root reconstruction imaging method. As a signal processing technique, Time reversal can be used to estimate the localization and characterization of a source of wave propagation, as well as to calculate the focus wave energy at selected points in space and time[103].

In this chapter, an Ultra-wide Band Microwave Imaging (UBMI) system has been proposed and developed that offers low-cost, high-contrast, and fast NDE for plant root imaging. The system is capable of creating a dielectric map of the scanning area by extracting the changes in both magnitude and phase in the transmitted and reflected signal. The time-reversal method has been used to create a 2D reconstruction image of the root, which can provide the size and position information of the root.

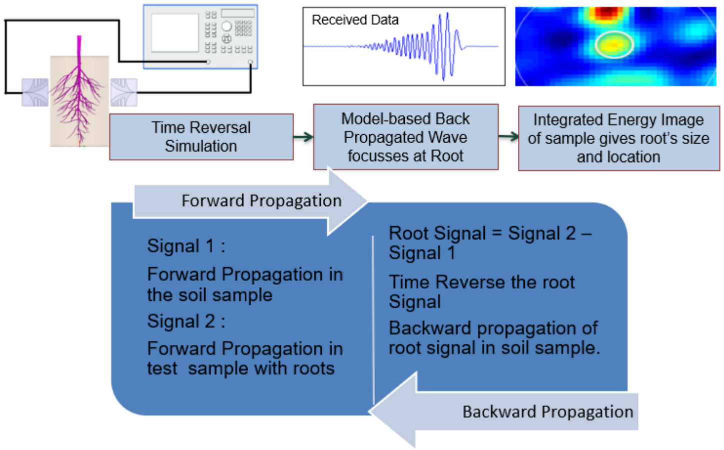

Figure 3.1: Flow chart of root imaging technique using time reversal.

3.2 Imaging System

An ultra-wideband TR-based microwave imaging system has been developed that offers the plant low-cost, high-contrast, and fast NDE techniques. The flow chart of the UBMI system is shown in

Fig.3.1. A Vivaldi antenna array operating at ultra-wideband frequency from 3 GHz to 10 GHz and providing high gain and symmetric beam patterns was designed in accordance with [104] to detect the root buried in the soil in-situ, based on the properties of TR. An arch range was constructed for fitting the antenna system, having a fixed position transmitter antenna and a receiver antenna that is rotated around the scanned target with uniform angular steps to emulate an antenna array. A vector network analyzer (Keysight E8363B) provides an excitation signal to the transmitting antenna that is radiated and transmitted through the root buried in the soil and recorded by the receiving antenna. The magnitude and phase measurements vary depending on the wave scattered by the soil and root sections. The perturbation due to the roots are computed and processed using a TR algorithm to image the root buried in the soil.

Time reversal imaging

The proposed TR algorithm offers a non-iterative processing framework for rapid root imaging. Unlike regularization-based imaging techniques that rely on an iterative framework for inversion, TR employs a physics-based direct back-propagation technique to perform imaging. The method exploits the time-symmetric nature of the scalar electromagnetic wave equation, expressed as

$$\left(\nabla^2 - \mu\varepsilon\frac{\partial^2}{\partial t^2}\right)\varphi(r,t) = 0. \tag{3.1}$$

where c is the speed of light in free space and μ, ε are the material permeability and permittivity, respectively. The time-symmetric nature of the wave equation allowed for fields diverging away to be reversed in time and converged back spatiotemporally to the scattering sources [105]. The detailed theory, numerical implementation, and analysis of the TR algorithm have been performed previously by the authors in [106]. As seen in [107], the TR algorithm can be implemented to detect targets and other scattering sources. The time-integrated energy (Θ) of the time-reversed wave can be utilized to obtain a focused Spatio-temporal image of the imaging domain, given by

$$\Theta(x,y) = \int_0^T h_n^2(t) = \int_0^T |E_z(x,y,t)|^2 dt, \tag{3.2}$$

where $h_n(t)$ and $h_n(-t)$ are the estimated forward and backward medium responses, and T is the total time. Here TM_z polarization is assumed, with E_x, E_y and $H_z = 0$.

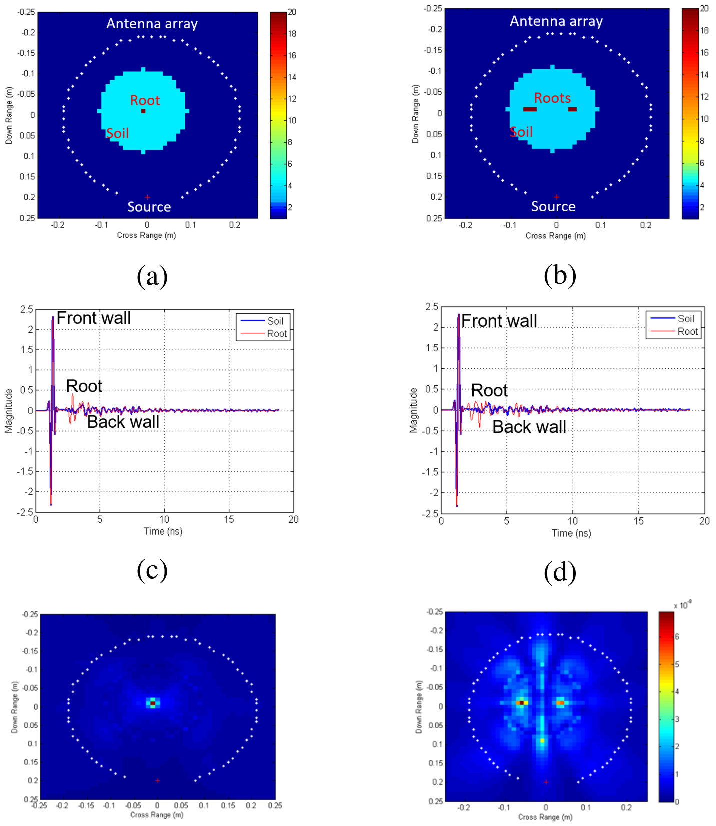

(a) (b)

(c) (d)

(e) (f)

Figure 3.2: Time reversal simulation results for single and multiple root showing (a, b) model schematic with permittivity distribution for single and two roots. (c, d) Forward scattered signals for receiver 30 (highlighted with + in Fig. 3.2(a, b)) for single and two roots. (e, f) Time integrated energy images detect the presence of roots for single and two root cases.

A 2-D numerical study is conducted to validate the feasibility of the TR algorithm for root imaging applications. The electromagnetic wave equations are numerically modeled using a finite-difference time-domain (FDTD) algorithm. The overall schematic of a single root section and multiple root sections embedded in a soil region, along with a source antenna and a circular receiver antenna array, is shown in Fig. 3.2(a, b). The soil region is assumed to comprise some moisture content with dielectric constant (ε_r)=10 and conductivity (σ)=0.04 S/m at 6 GHz, while the root section is assumed to be mostly dry with ε_r=4 and σ=0.008 S/m at 6 GHz. A modulated Gaussian pulse with a width of 0.1 ns is used to excite the source antenna. The scattered fields

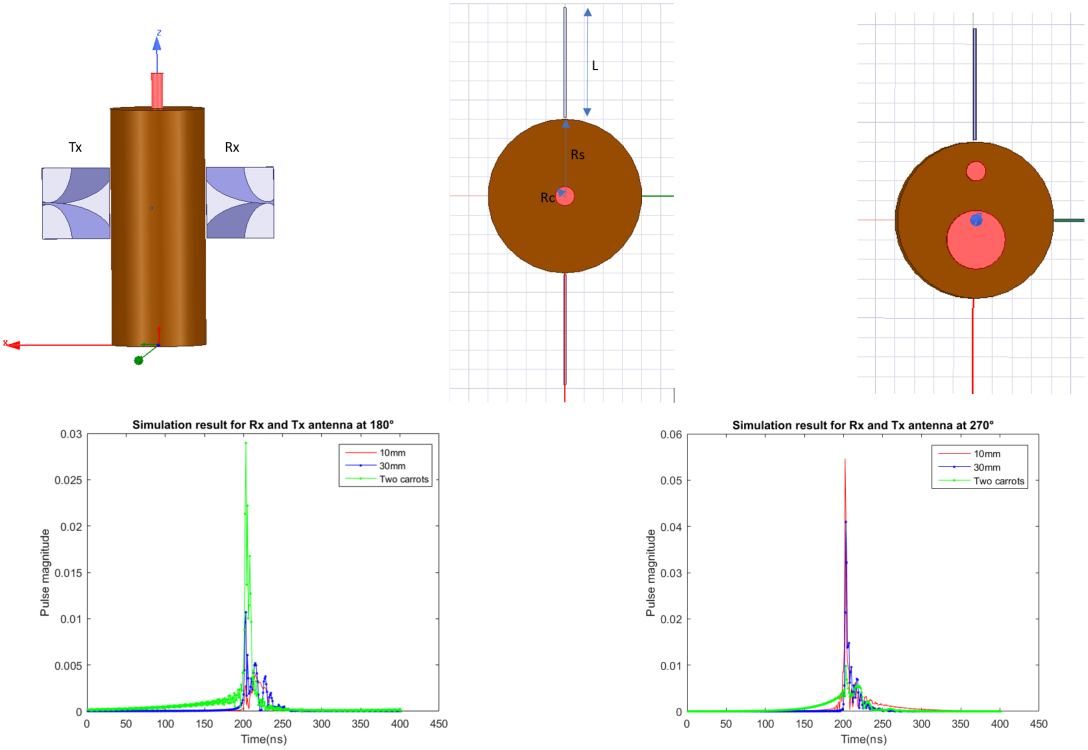

Figure 3.3: Schematic of the HFSS simulation showing (a) side view of the container with soil and carrot, and location of launcher and receiver antennas, (b) top view showing container with soil and single carrot, and (c) top view showing container with soil and two carrots. The time-domain results for the antennas at (d) 180° and (e) 270°.

are computed for this model and an equivalent model without the presence of root to reduce the soil scattering effects and obtain the root perturbations. The scattered field signals for Receiver 30, with and without the roots for single and multiple roots, are shown in Fig. 3.2(c, d). The received signals for the root model consist of the front wall scattering of the soil region followed by the root scattering, back-wall scattering of the soil region, followed by second-order scattered fields. The scattering due to the root is absent for the equivalent model without the root. The root perturbations for each receiver antenna are computed and numerically back-propagated using the FDTD TR algorithm. As seen in Fig. 3.2(e, f), the computed time-integrated energy shows efficient focusing around the root regions for both single and multiple roots. As can be seen in the case of multiple roots, cross-coupling between the two roots leads to some additional artifacts around the soil top and bottom interfaces in the energy images. The simulation results show that the proposed TR algorithm can effectively image buried roots in a soil environment.

HFSS Simulations

3D high-frequency structure simulation studies are conducted to analyze the sensitivity of the antenna system towards root detection using a commercial electromagnetic field simulator Ansys HFSS. An antipodal Vivaldi antenna is designed for ultra-wideband, high gain, and beam symmetry to illuminate the root. The HFSS simulation model when the azimuth angle between Tx and Rx is 180,° is shown in Fig.3.3(a) to (c) as an illustration. The Tx is fixed, and the Rx rotates around the scanned target root with a uniform angular step of 10°. The start and endpoint for Rx are at an azimuth angle of 50° from Tx. The soil (Rs) radius is 50 mm, and the radius of the root(Rc) is set to be 10 mm and 30 mm, respectively. The single carrot with different two radius sizes and the combination of these two carrots are all simulated to analyze the performance of the designed antenna fully, as shown in Fig.3.3(b) and (c).

The S_{12} magnitude and phase frequency domain data are converted to time domain data using a standard inverse fast Fourier transform (IFFT) method. The envelopes of the pulses when the angular steps theta are 180° and 270° are shown in Fig.3.3(d) and (e), respectively. The pulse magnitudes have a significant difference between the different radius of the carrot in every angular step. The larger the size of the root, the bigger the pulse magnitude. In addition, the pulse magnitudes of two carrots are significantly different from that of a single carrot. The simulation results show that the proposed ultra-wideband microwave imaging system can effectively identify different sizes and numbers of carrots buried in the soil.

3.3 Experimental results

Experimental setup

The antennas are connected to a vector network analyzer for the experimental setup, which radiates power to the transmitter antenna and reads the received power through the receiver Vivaldi.

The experimental setup is shown in Fig.3.4. Two carrots of varying sizes are considered samples under test. The average diameter of the small carrot is 16 mm, while that of the bigger one is 25

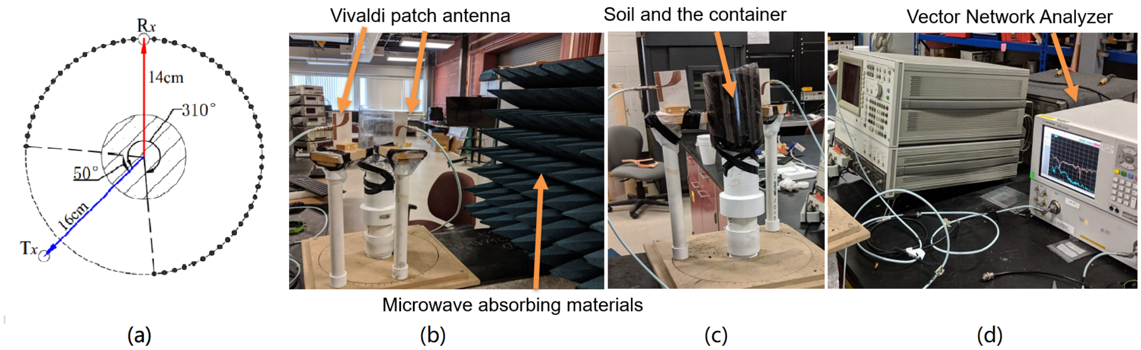

Figure 3.4: (a) Schematic of the experimental setup showing the scanning location points spaced angularly at 10°. Experimental setup showing (b) Vivaldi style patch antennas with centrally located sample container containing soil and carrot, with a microwave absorber, (c) close view of soil container and two antenna supports of which one is mounted on a rotating base and (d) RF signal measurement equipment's (VNA).

mm. The diameter of the soil container is 100 mm. Microwave pyramidal foam absorber materials were placed in the surrounding of the setup to prevent spurious reflections from introducing the error in the measurements.

Three sets of measurements (small carrot, large carrot, and two carrots together) are performed to see the imaging capability of the system. The transmitter and receiver are placed at a distance of 16 cm and 14 cm from the center of the container, respectively. The starting position of the receiver subtends an angle of 50° with the transmitter at the center of the container. A circumferential scan of 260° (till the receiver is at 310°) is performed at steps of 10°.

Results

Fig.3.5 shows the S_{21} amplitude and phase for the small carrot, large carrot, and multiple carrots, respectively. Position 1, 2, and 3 refers to the receiver's position at 90°, 180° and 270° respectively. It is observed that the variations in magnitude are higher at 90°, while the phase change is similar at all three positions. However, the phase data for the three positions are more distinguishable than the amplitude data. This is because even though the relative distance between the Tx and Rx does not change to a large extent, the angular change has a greater effect on the phase of the received

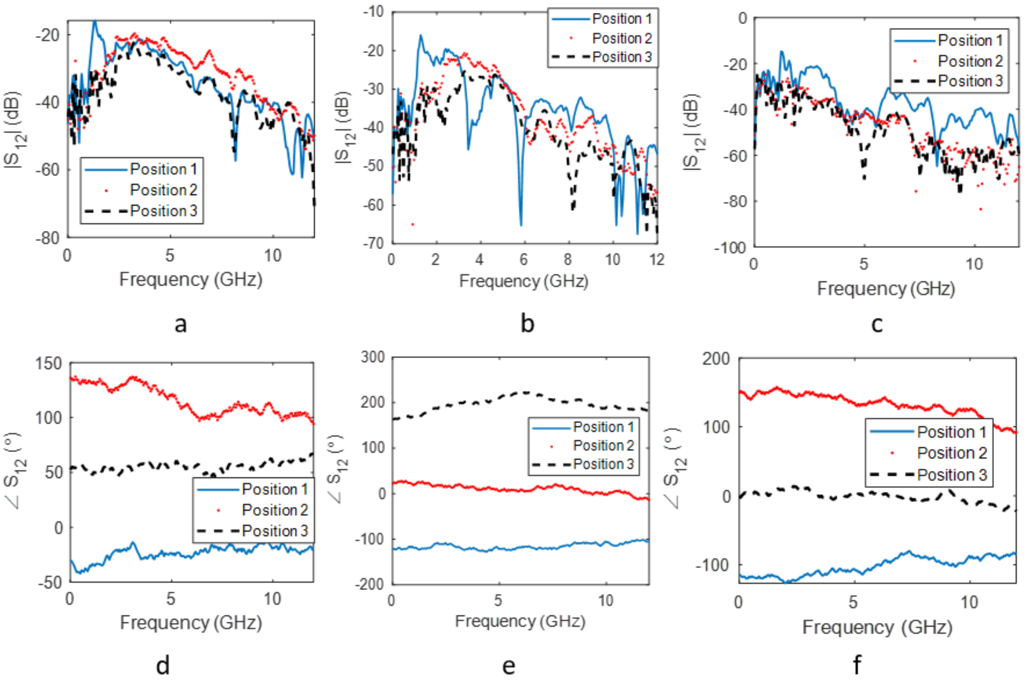

Figure 3.5: Insertion loss magnitude for (a) small carrot, (b) large carrot and (c) multiple carrots. Insertion loss phase for (d) small carrot, (e) large carrot and (f) multiple carrots.

signals.

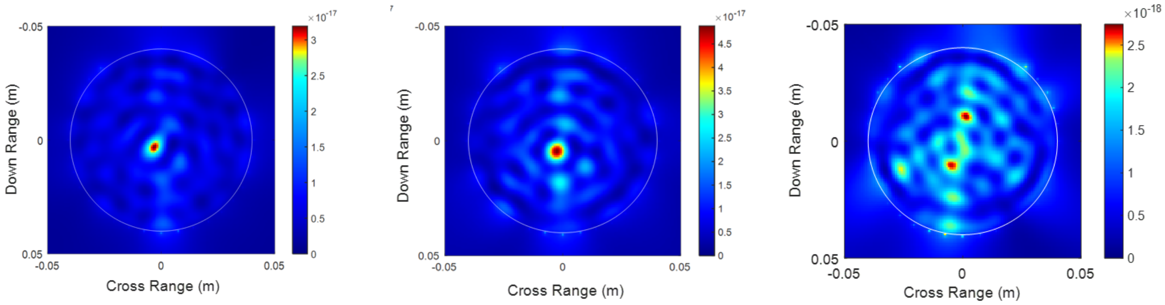

(a) (b) (c)

Figure 3.6: Time reversal imaging for (a) small carrot, (b) large carrot and (c) multiple carrots.

The frequency-domain data is converted to time-domain pulses and back propagated using an FDTD model. The images obtained by TR imaging for the three sets of measurements as shown in Fig.3.6(a) and (b) capture the change in sizes of the carrots. In the case of 3.6(c), we see two distinct localized spots corresponding to the two carrots. Additional artifacts are noticed more in the multiple carrots case. This can be attributed to the increase in multiple scattering when the waves encounter two roots instead of a single carrot.

Discussion on the error estimate

Fig.3.6(a) and (b) present the individual TR images obtained for the 16 mm and 25 mm carrot, respectively. 3.6(a) produces a cleaner image due to weaker scattering by the 16 mm carrot as compared to the 25 mm carrot. Estimation of the size of the target is done by applying image processing techniques to the TR images. Explicitly, the TR images are converted to gray-scale images and convolved with a Gaussian filter. Appropriate thresholding is further done to detect hot spots in the images, corresponding to the targets (roots in our case). We define an error metric ζ as:

$$\zeta = \frac{y - x}{y} \tag{3.3}$$

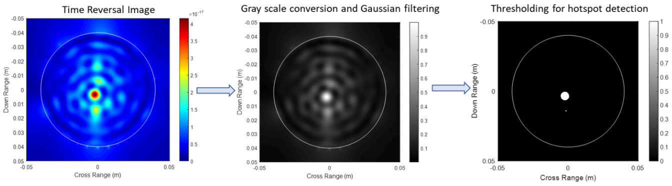

Figure 3.7: Image processing steps for the detection of targets. Root size and shape estimation of the large carrot.

Where y is the true size of the target and x is the estimated size of the target obtained from TR. Figure 3.7(a) illustrates the image processing steps for the detection of the targets. This includes two steps where the first step converts the RGB image to a greyscale image and applies Gaussian filtering. The second step applies thresholding to detect the hotspot. The diameter of the targets (value of x in (1)) are estimated to be 5 mm and 7 mm, respectively. The shortest diameter of the hotspot is reported as the estimated size to avoid smudging caused due to experimental inaccuracies. The error metric ζ is calculated to be 0.68 and 0.72, respectively, for 16 mm and 25 mm carrots. The differences can be attributed to several factors. Mainly, the source and receivers for the TR imaging are modeled in the FDTD code as point sources. However, in practice, they consist of patch antennas of finite sizes, and this approximation can cause localization errors, which in turn will result in an erroneous image target size. Also, any deviations in the modeled permittivity value of the soil (medium) from its actual value will cause an error in localization. Although the exact localization spots do not correspond to their true sizes, it should be noted that the ratio of their sizes is equivalent, i.e., the small to large image target size ratio is 0.71 while the true size ratio is 0.64. Future work is being planned to involve machine learning on the signals or deep learning on the images generated to correct such errors. The advantage of this method is the speed of imaging, which can be in the order of a few seconds depending on the scanning speed. With present-day robotics technology, the scanning speed can be quite sufficient to achieve real-time imaging and evaluate the condition of roots in the field. The antenna parts can be made using rugged materials like metals and Teflon, which are corrosion resistant and can withstand harsh environmental conditions endured by plants like moisture and sunlight.

3.4 Conclusion

An ultra-wideband microwave imaging system is proposed for the in-situ nondestructive root phenotyping. The system has been developed to estimate the location and shape of the root with the soil's background noise. The capability to provide the size and localization information of single and multiple roots demonstrates the simulation framework's robustness. Precise results and high imaging quality of the reconstruction achieved from the experiment studies validate the proposed microwave imaging method's accuracy. The 2D imaging can be improved to 3D phenotyping with the antenna array's deployment both in the vertical and circumferential direction around the root for field inplementation. The non-iterative TR algorithm proposed for signal processing is computationally efficient that enables rapid localization of roots. This work also shows its ability for the real-time monitoring of the root system in the real soil environment. The advantage of its rapid scanning ability and robustness enables the microwave imaging technique to be deployed in fields for scanning a large volume of soil and access the state of roots in a real-time manner.

CHAPTER 4

NDE SYSTEM DESIGN FOR THE BOILER INSPECTION ROBOT

4.1 Introduction

The aim of this chapter is to design and optimize a portable NDE system for the intelligent mobile robotic platform with capabilities for autonomous live inspection and repair. In many industrial environments, such as the application of power plant boiler inspection, human inspectors often have to perform hazardous and challenging tasks. There is a significant chance of injury, considering the confined spaces and limited visibility of the inspection environment and hazards such as pressurization and improper water levels. In order to provide a solution to eliminating these dangers, the concept of a new robotic system was developed and prototyped that is capable of autonomously sweeping the region to be inspected. The robot design contains systematic integration of components from robotics, NDE, and artificial intelligence (AI).

This chapter studies a design of a portable NDE scanning system based on eddy current array probes, which can be customized and installed on various mobile robot platforms. Machine learning methods are applied for semantic segmentation that will simultaneously localize and recognize defects without the need for human intervention. Experiments have been conducted that show the NDE capabilities of the system. Improvements in human safety and structural damage prevention and lower overall maintenance costs are possible by implementing this robotic NDE system. Some of the contents and results in this section have been presented in [108].

The flow chart in Figure 4.1 gives a schematic illustration of the proposed robotic NDE and repair system. A portable NDE system needs to be designed that has components to acquire received physical signals back to the “Computational Space”. “NDE Space” refers to the functionalities required to send and receive signals between the probe and material under test. In contrast, “Computational Space” refers to the functionalities an embedded chip or computer will handle. The main unit for the computational space is the control unit, which facilitates the overall system’s operations. For NDE purposes, there are two asynchronous processes handled by the control: moving the end-effector to the material via optimal tool-path planning and conducting the NDE measurements. The proposed system is a typical Cyber-Physical System (CPS) with unique challenges for the NDE community.

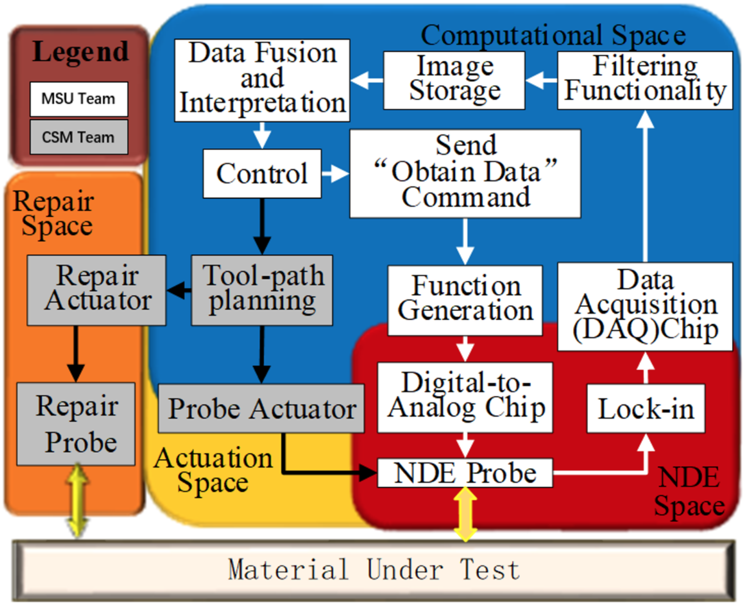

Figure 4.1: Robotic NDE and Repair System Flowchart.

4.2 NDE Sensors

4.2.1 Eddy Current Sensors

Eddy current technique is based on electromagnetic induction. A time-varying electrical current energizes a wounded coil (primary current). A magnetic flux is generated at the center of the wounded coil as shown in Figure 4.2, which is adopted from [7] for illustration. Based on Faraday's induction theorem, the alternating flux generates electrical current in a conductor if it is placed perpendicular to the flux direction. As a result, circulating electrical currents flow in the conductor in the form of eddy waves, which are called eddy currents.

The circulating eddy currents generate their own magnetic field, which opposes the primary magnetic field. The presence of the cracks in the test material disturbs the baths of the eddy

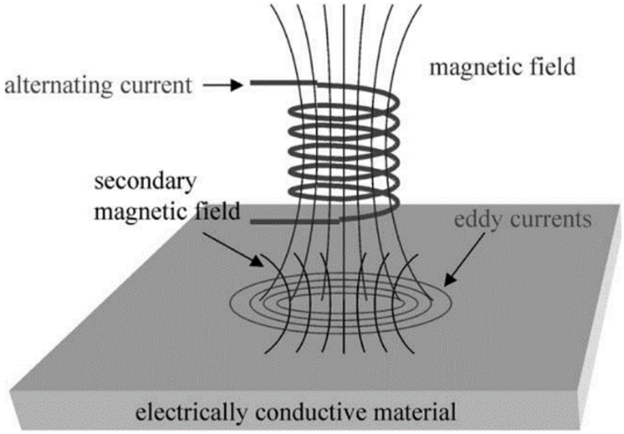

Figure 4.2: Primary and secondary magnetic field. Eddy current on the test piece [7].

currents and the secondary magnetic field. Thus, changes in the secondary magnetic field are used as indications of the presence of the crack. The following measurement techniques are used to measure the magnetic field in the eddy current. Induction coils and semiconductor-based devices such as Hall sensors, magneto-resistance, and measure are being widely used to measure the magnetic field.

4.2.2 Near Field Microwave Sensor

A nearfield microwave imaging system consists of either a single transceiver or multiple arrays of probes, which illuminates the OUT and measures the localized response from the material. The response varies with the electrical properties of the material. However, to achieve high-resolution images, the separation between the tip of the near-field antenna and the surface of the sample has to be small and stay constant. The precision of that distance will significantly influence the accuracy of a near-field imaging system.

The block diagram of implemented setup is shown in Figure 2.3. An 8 GHz RF source generator is used to feed the near-field microwave probe. The low output of the source is amplified to +24 dBm, and a 3 dB RF splitter is used to divide the amplified signal into a feed and a reference signal. The directional coupler is connected to the feed signal coming from the splitter and is also used to probe the reflected power. The reflected signal is mixed with the reference signal to get any changes in phase according to the changes in the object's properties.

The probe used for imaging is a coaxial cable with an open-ended copper tip due to its simple design, easy availability, and wide band frequency response. The experiments are performed by keeping the tip perpendicular to the object, where the fields are stronger and localized.

4.3 Preliminary Experimental Tests

The sample shown in Figure 4.3 is prepared with multiple defects for testing with different widths and lengths. A total number of 12 defects are fabricated on the sample. Table **??** lists the length and width of the samples staring from the most left defect on the sample appearing in Figure 4.3.

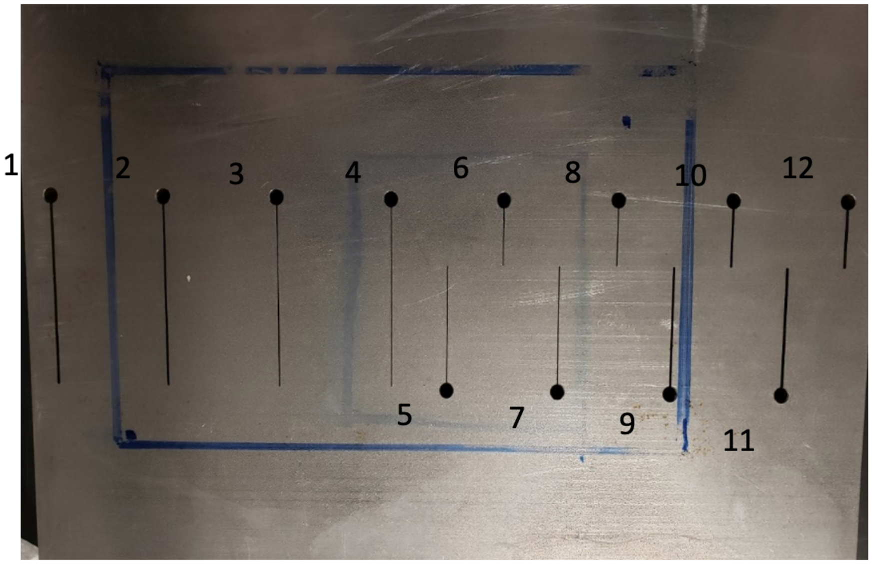

Figure 4.3: The sample under test. The cracks are with different width and length.

Crack	1	2	3	4	5	6	7	8	9	10	11	12
Length (mm)	60	60	60	60	40	20	40	20	40	20	40	20
Width (mm)	1	0.8	0.4	0.2	0.2	0.2	0.4	0.4	0.8	0.8	1	1

Table 4.1: Length and Width of Samples (starting from left-most defect).

The defects are fabricated in the physics workshop at Michigan State University. Due to limitations in controlling the depth of the cracks, the depth is set to the sample thickness. For future testing, samples will be prepared using advanced cutting technologies, and high-tech companies will be consulted.

4.3.1 Eddy Current Testing

The eddy current testing is done using a transmitter and receiver eddy current sensor. The setup is depicted in Figure 4.4. The transmitter and receiver eddy current sensor has 400 turns in total, 200 turns for the transmitter, and 200 turns for the receive. The transmitter coil is excited with time-varying sinusoidal input. Increasing the excitation frequency enhances the voltage of the transmitter coil, which induces the eddy currents on the test sample; however, as the excitation frequency is further increased, it has an inverse effect on the skin depth of the eddy currents on the tested material. The following excitation frequencies are used 30 kHz and 50 kHz. The results are presented for comparison as follows.

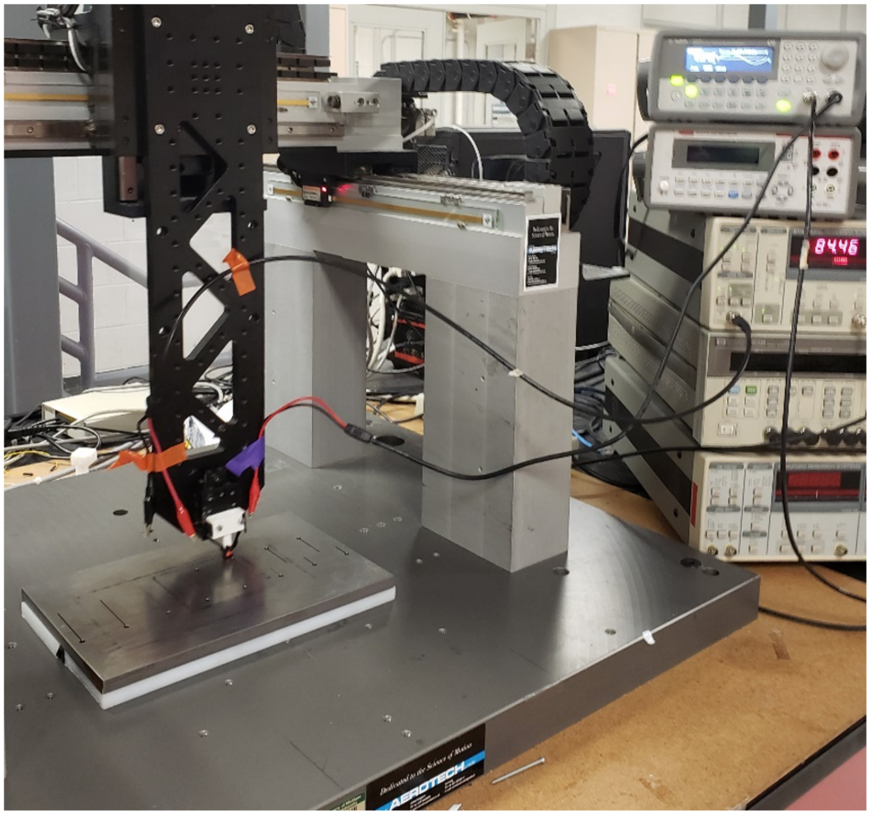

Figure 4.4: Eddy current TR sensor Experimental Setup.

In the results signal received by the receiver coil is passed to a lock-in amplifier. For detecting the effect of crack on the eddy current are detected by monitoring voltage amplitude and phase induced on the receiver coil. For testing the system, an area of 80 mm is inspected. The selected area encompasses the four-narrow crack in the sample.

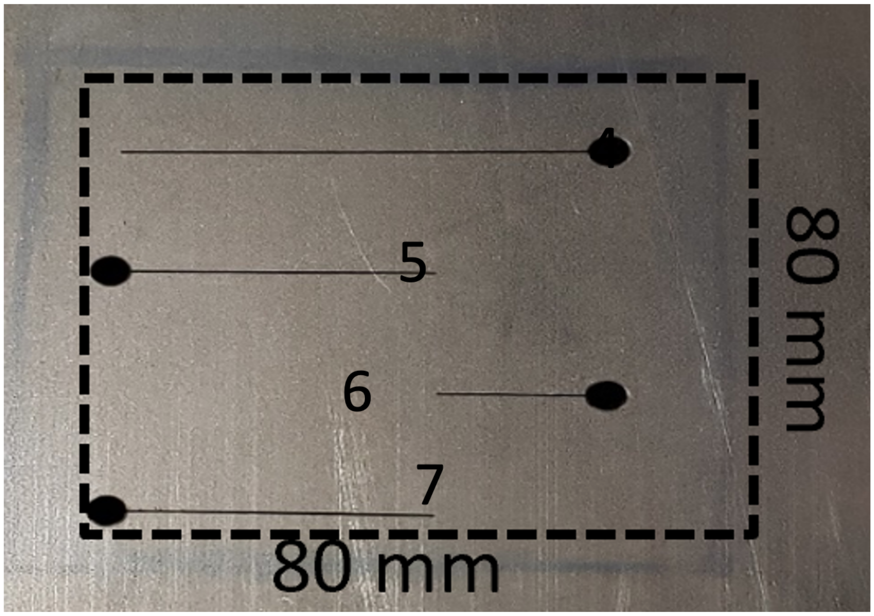

Figure 4.5: 80 mm^2 inspection area.

The following figures show the results of the eddy current inspection using different excitation frequencies and different scanning speed.

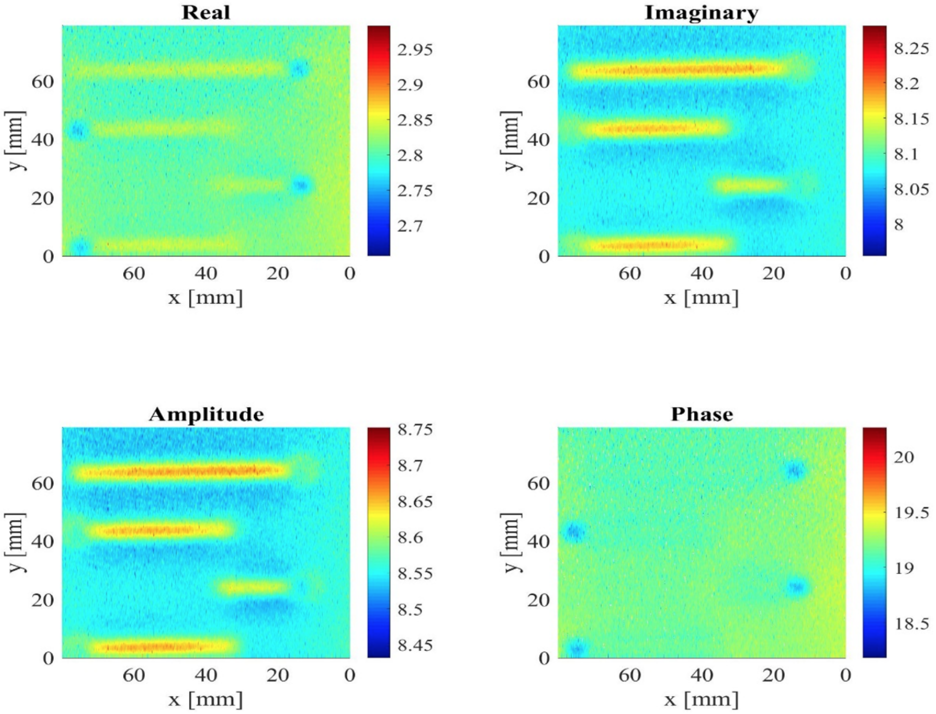

Figure 4.6: Eddy current imaging using 30 KHz excitation and scanning speed of 10mm/s.

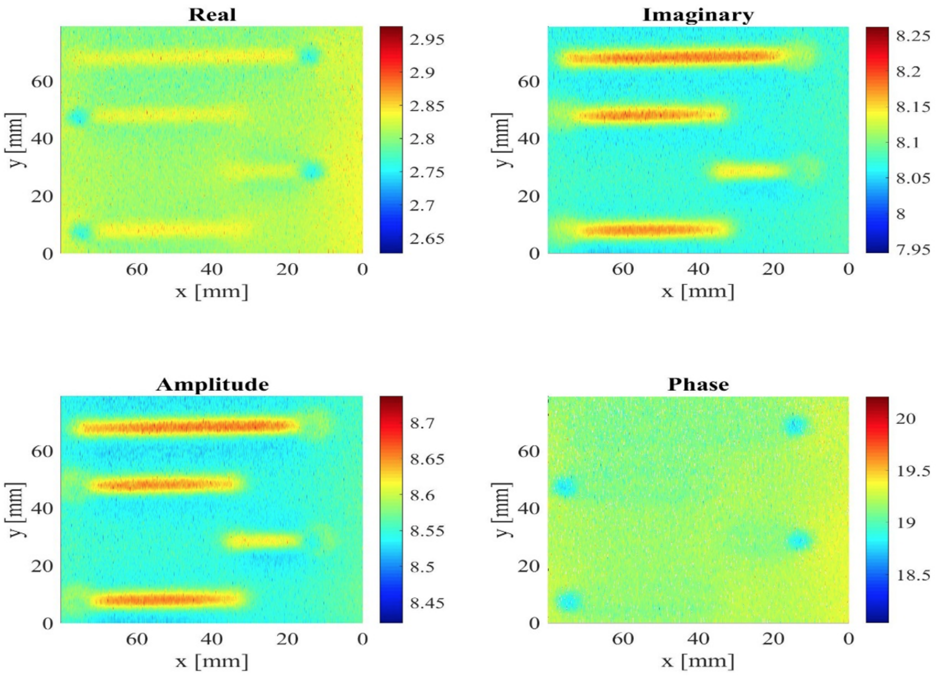

Figure 4.7: Eddy current imaging using 30 KHz excitation and Scanning speed of 5mm/s.

Inspecting the sample with 30 kHz for 10mm/s and 5 mm/s are shown in Figure 4.6 and Figure 4.7, respectively. The received signal is amplified using the lock-in amplifier. The real and imaginary values are mapped to amplitude and phase to extract further information about the scanning results. The four quantities are used to create images of the eddy current scanning. Comparing the images of 30 kHz excitation frequency to 40 kHz in Figure 4.8 and Figure 4.9 for 10 mm/s and 5mm/s, respectively, the sensitivity to the crack position was enhanced.

In the experimental testing, an excitation frequency of 50 kHz showed better results for both scanning speeds, as presented in Figure 4.10 and Figure 4.11 compared to the previous results. Although reducing the speed from 10mm/s to 5mm/s did not show better contrast in the defect region, it resulted in less variation in the defect-free region values.

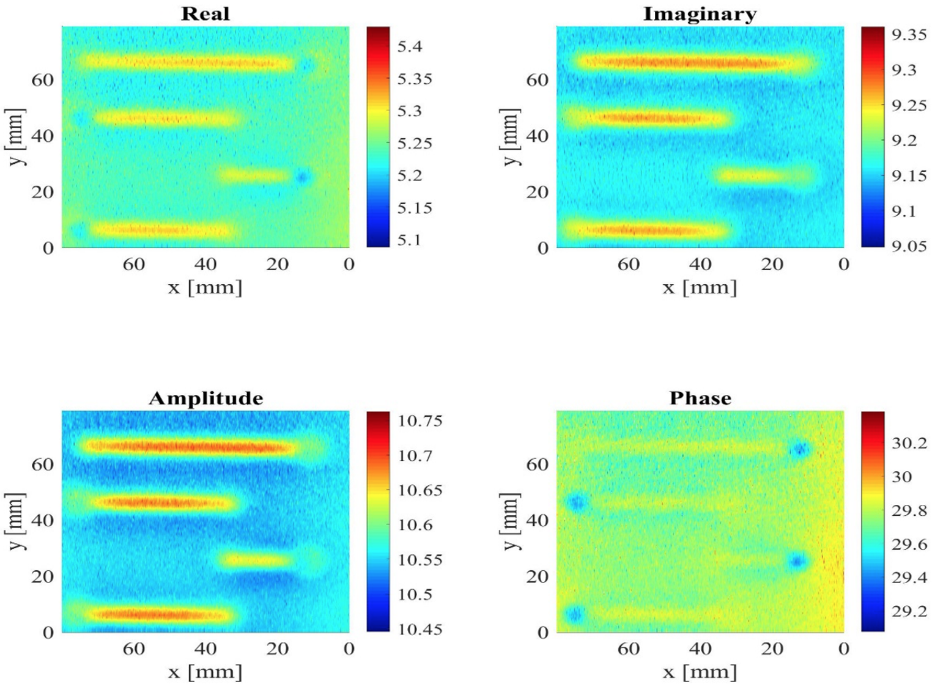

Figure 4.8: Eddy current imaging using 40 KHz excitation and scanning speed of 10mm/s.

In the results signal received by the receiver, the coil is passed to a lock-in amplifier. For detecting the effect of crack on the eddy current is detected by monitoring voltage amplitude and phase induced on the receiver coil. For testing the system, an area of 80 mm is inspected. The selected area encompasses the four-narrow crack in the sample. The following figures show the results of the eddy current inspection using different excitation frequencies and different scanning speed.

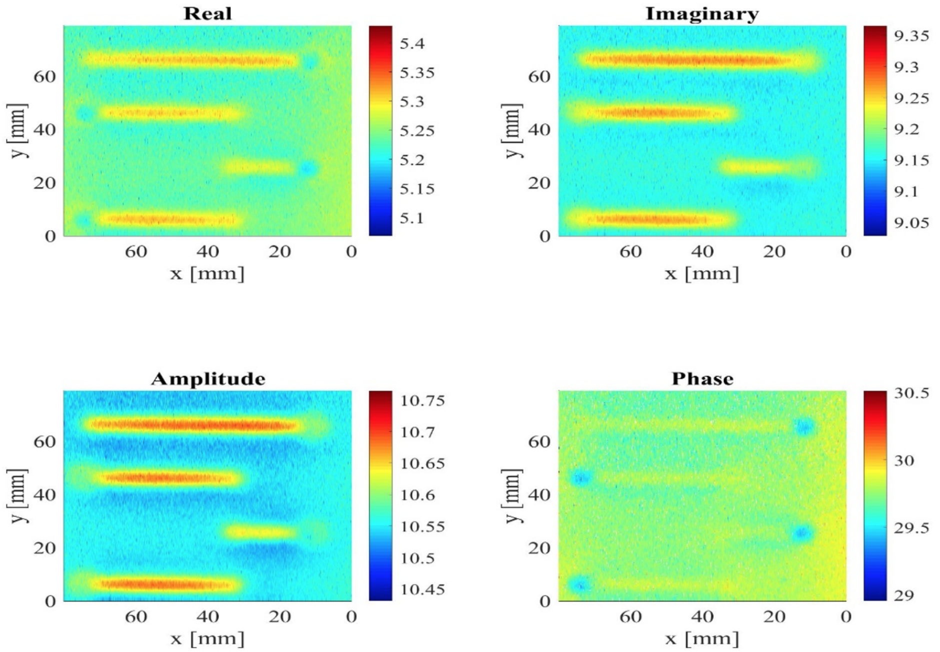

Figure 4.9: Eddy current imaging using 40 KHz excitation and scanning speed of 5mm/s.

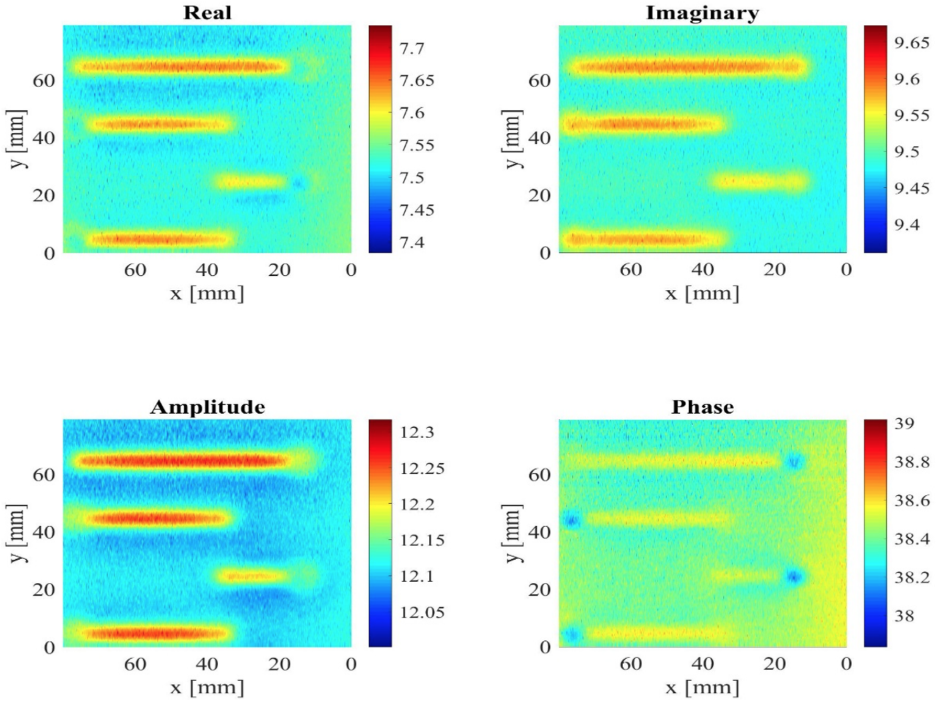

Figure 4.10: Eddy current imaging using 50 KHz excitation and scanning speed of 10mm/s.

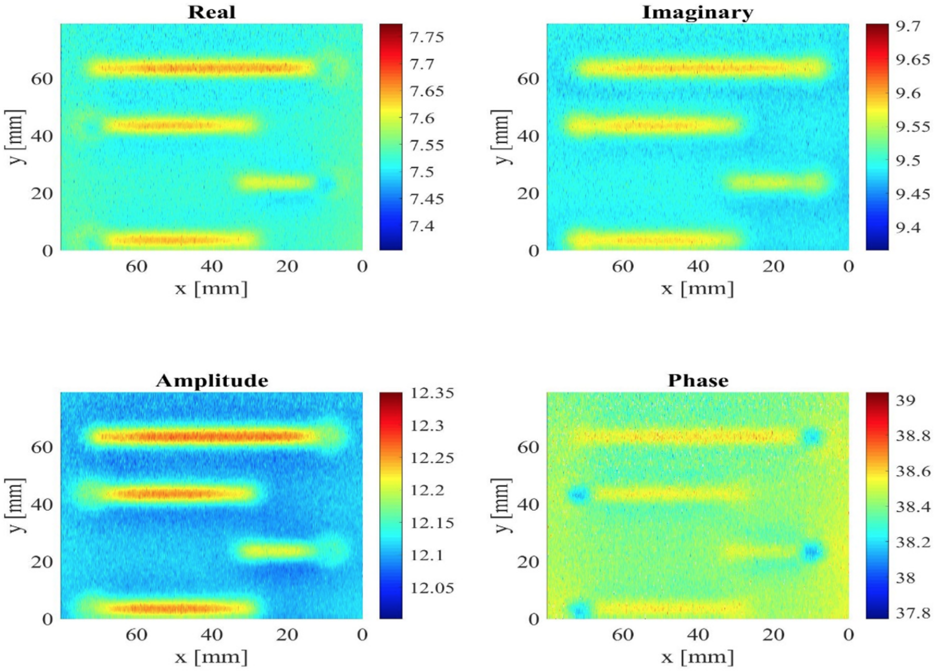

Figure 4.11: Eddy current imaging using 50 KHz excitation and scanning speed of 5mm/s.

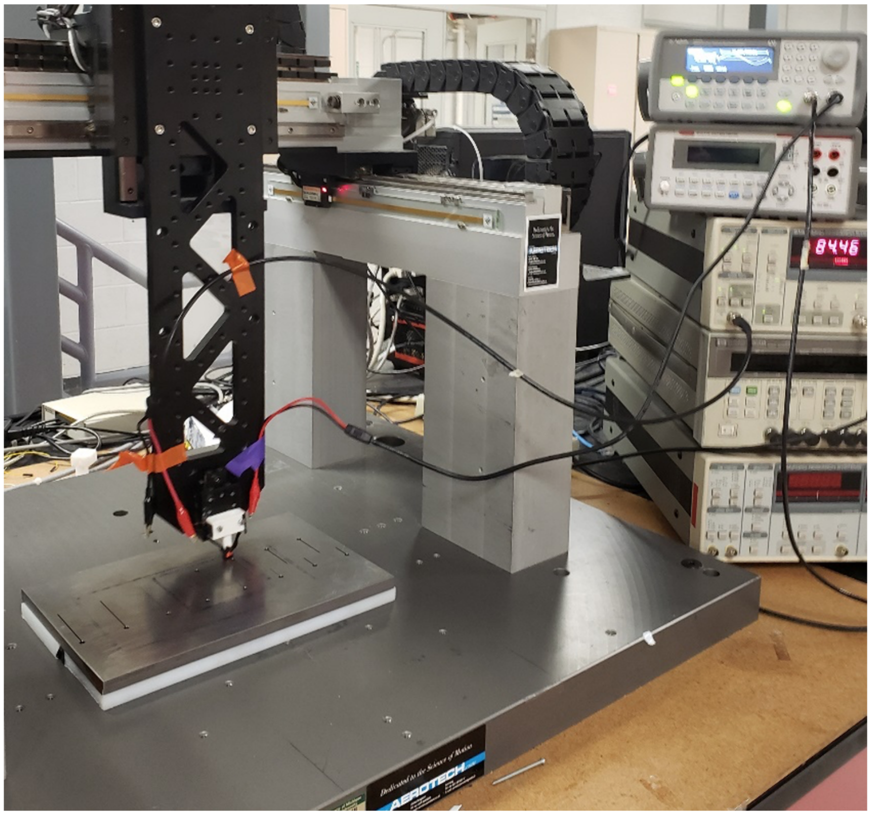

Figure 4.12: Eddy current TR sensor Experimental Setup.

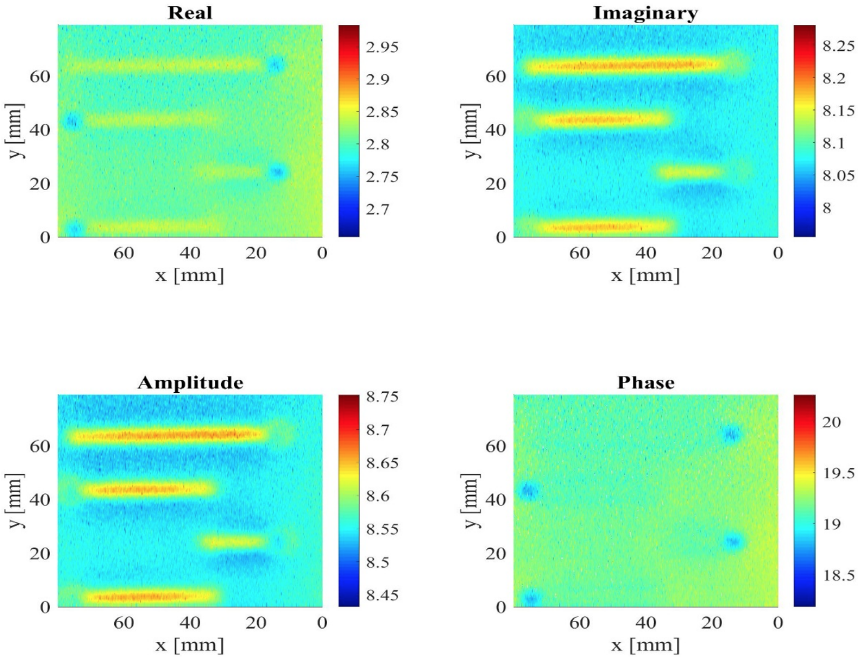

Figure 4.13: Eddy current imaging using 30 KHz excitation and scanning speed of 10mm/s.

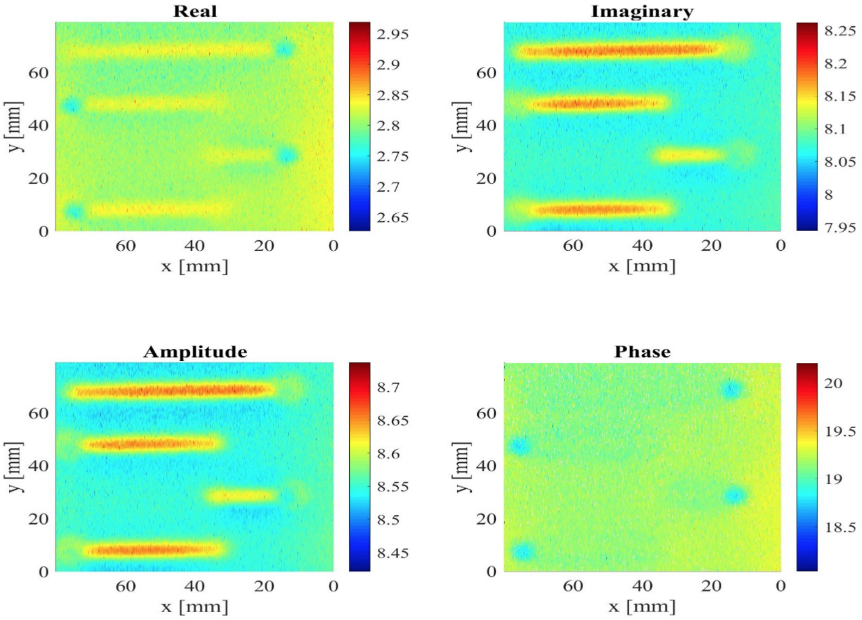

Figure 4.14: Eddy current imaging using 30 KHz excitation and Scanning speed of 5mm/s.

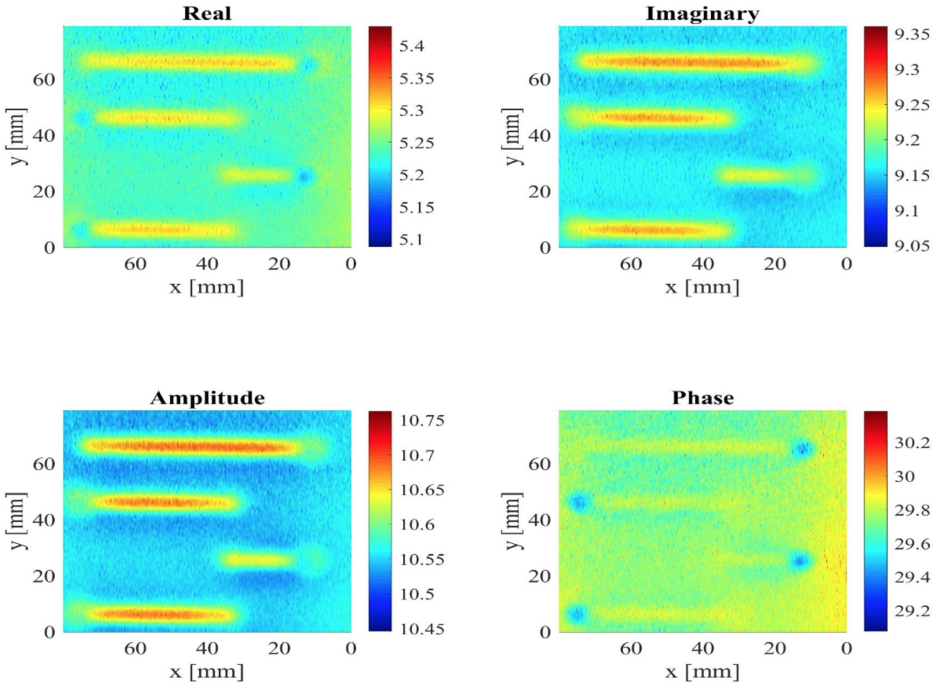

Figure 4.15: Eddy current imaging using 40 KHz excitation and scanning speed of 10mm/s.

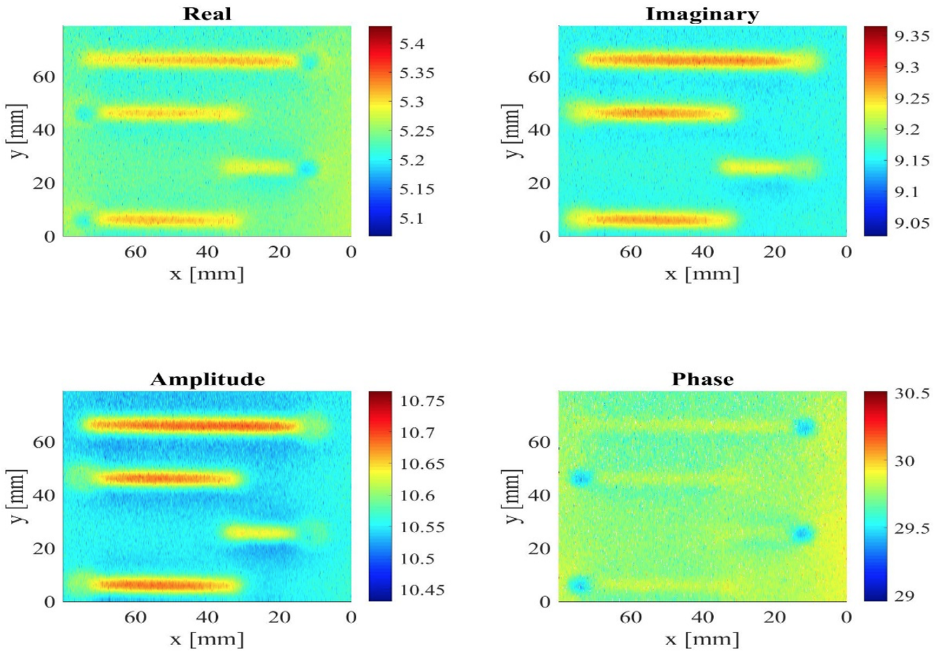

Figure 4.16: Eddy current imaging using 40 KHz excitation and scanning speed of 5mm/s.

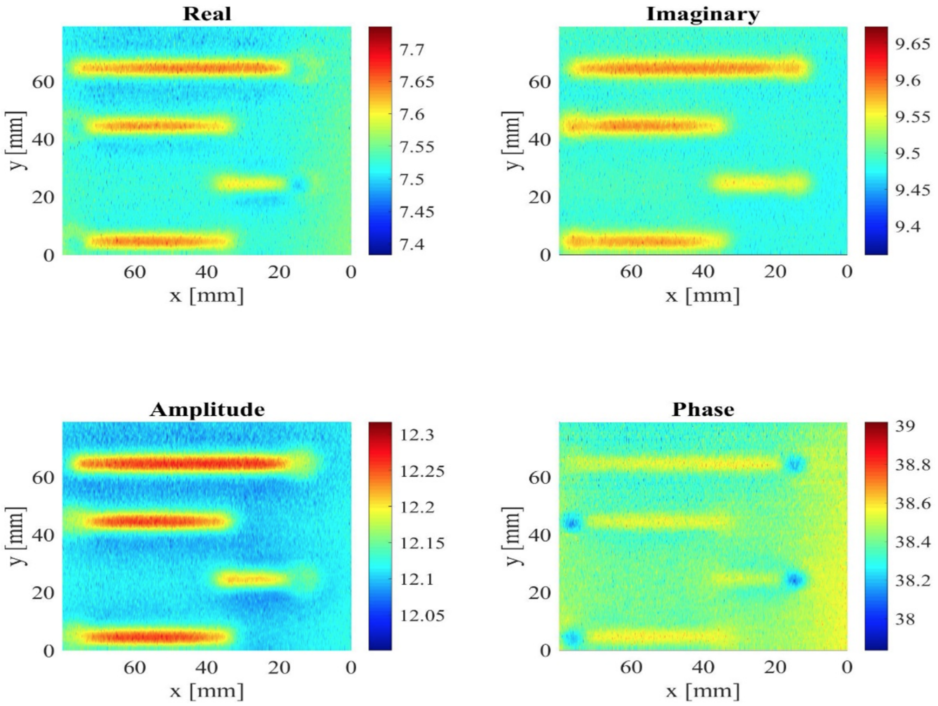

Figure 4.17: Eddy current imaging using 50 KHz excitation and scanning speed of 10mm/s.

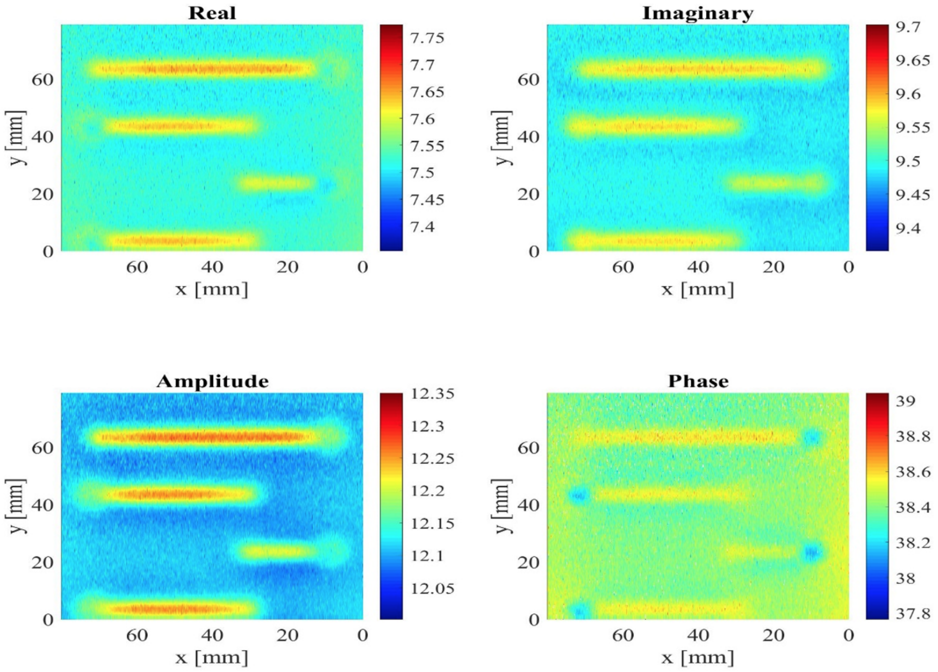

Figure 4.18: Eddy current imaging using 50 KHz excitation and scanning speed of 5mm/s.

Inspecting the sample with 30 kHz for 10mm/s and 5 mm/s are shown in Figure 4.13 and Figure 4.14, respectively. The received signal is amplified using the lock-in amplifier. The real and imaginary values are mapped to amplitude and phase to extract further information about the scanning results. The four quantities are used to create images of the eddy current scanning. Comparing the images of 30 kHz excitation frequency to 40 kHz in Figure 4.15 and Figure 4.16 for 10 mm/s and 5mm/s, respectively, the sensitivity to the crack position was enhanced.

In the experimental testing, an excitation frequency of 50 kHz showed better results for both scanning speeds, as presented in Figure 4.17 and Figure 4.18 compared to the previous results. Although reducing the speed from 10mm/s to 5mm/s did not show better contrast in the defect region, it resulted in less variation in the defect-free region values. Further investigation of the effect of scanning speed is planned in our future work. The presented results show the raw data of the experimental scanning. Postprocessing for image enhancement will be done in the next phase.

4.3.2 Near Field Microwave Sensing

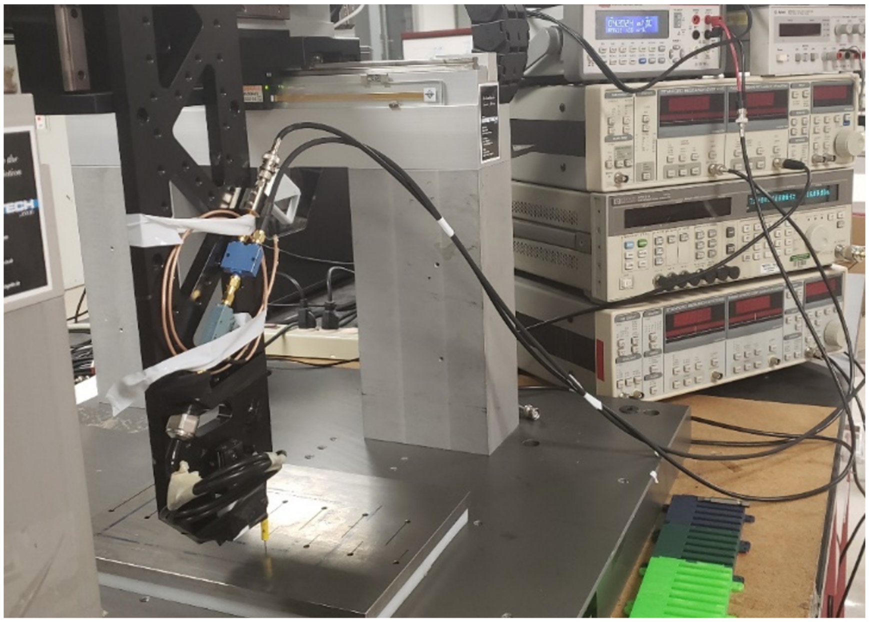

Figure 4.19: Near Field sensing experimental Setup.

An area of 40mm X 20mm is inspected. The selected area contains the smallest crack in the current sample as shown in Figure 4.20.

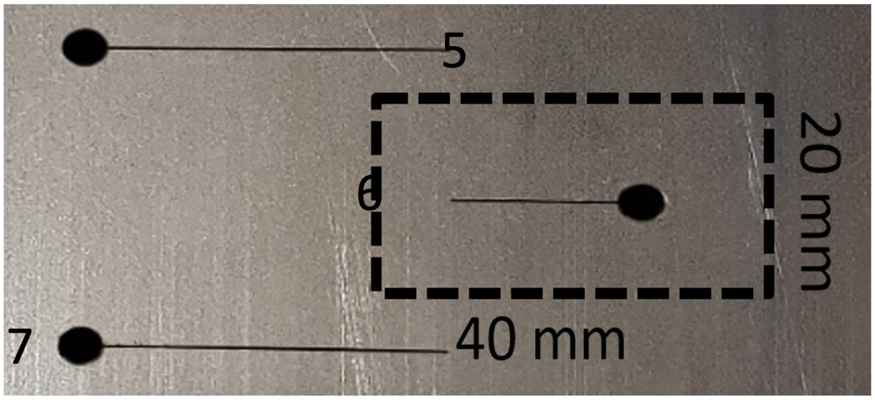

Figure 4.20: 40 mm×20mm inspection area.

An 8.6 GHz, 16 dBm microwave signal excitation to coaxial open-ended antenna. The reflected and through the antenna is mixed with a reference signal, and the DC part of the mixed signal is measured by digital multimeter. The result of the coaxial cable anatta imaging is depicted in Figure 4.21.

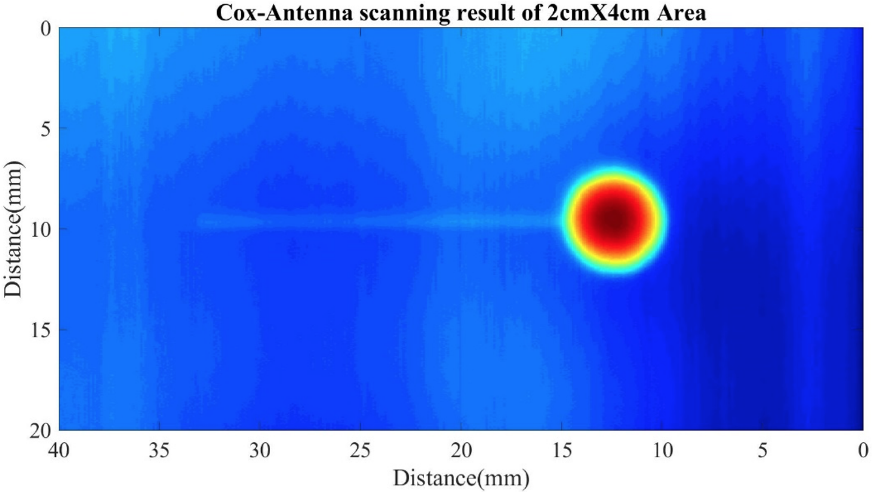

Figure 4.21: 40 mm×20mm scanning Image.

4.4 Coil Array

Although the scanning results show the scanning system's capability to detect the defects with 0.2 mm width, the long scanning time becomes one of the constraints that prevent applying these NDE methods directly on the robot platform. In this case, a sensor array that is able to cover more area in the unit time has been studied through simulation and experiment. To better understand coil array properties, a simulation has been performed.

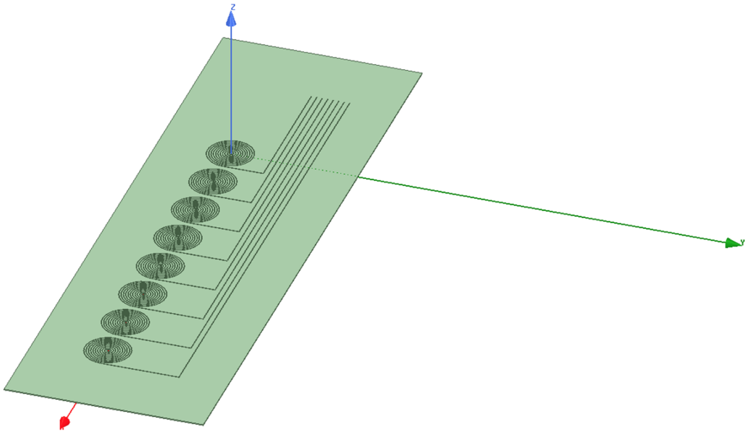

Figure 4.22: Simulation model of coil array.

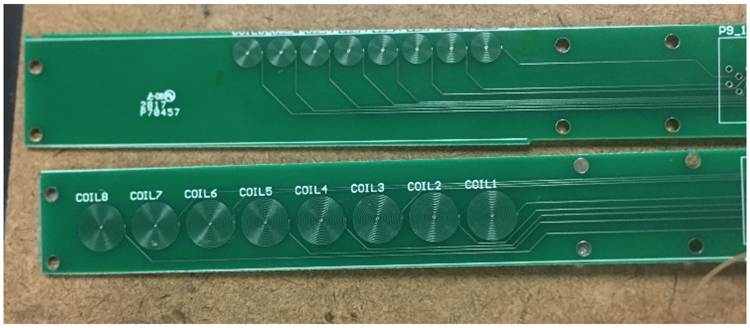

Figure 4.23: Coil arrays with different sizes of coils.

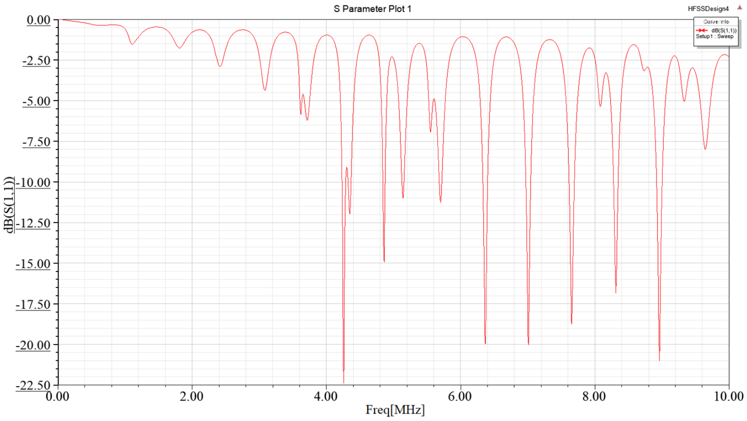

Figure 4.24: S11 simulation result of the coil.

A 1-D scan cross the 2 or 3 cracks (width 0.2 mm) using coil #8~#5 has been perform and each of four coils covered different areas.

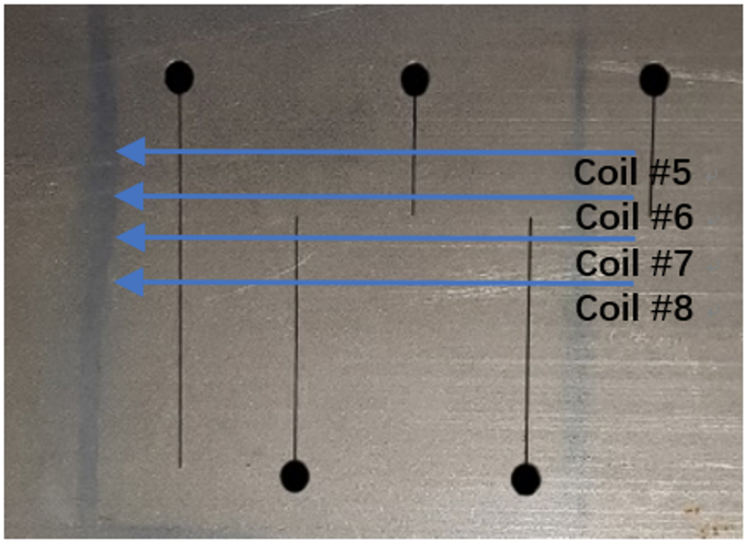

Figure 4.25: Scanning path of the coil array.

The scanning results have been shown below.

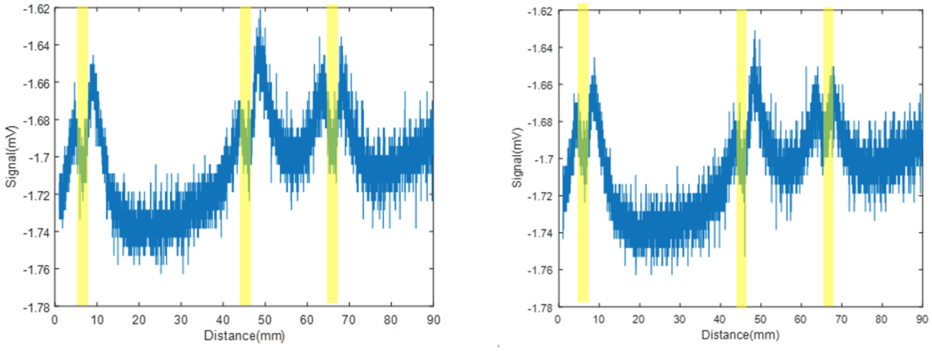

(a) coil#8 (b) coil#7

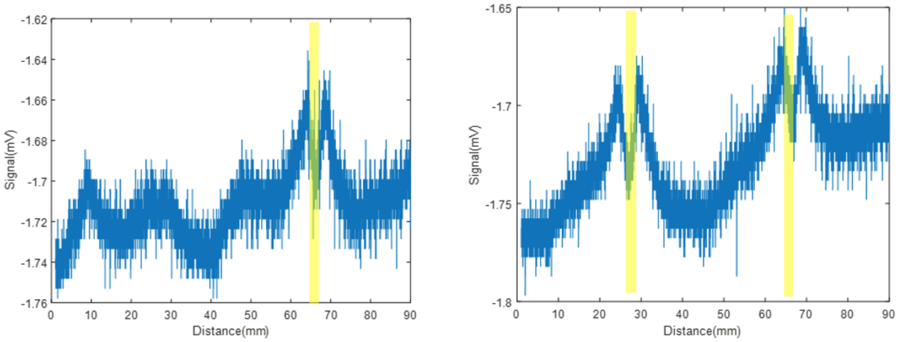

(c) coil#6 (d) coil#5

Figure 4.26: Scanning result of each coil at 8 MHz.

As shown in Figure 4.26, all four coils detected the 0.2 mm width cracks in their own scanning areas. This shows the capability of significantly reducing the scanning time using the array sensor.

4.5 Data Fusion

Recent studies have demonstrated that data fusion is effective in overcoming the limitations of the single NDE method by integrating several methods, and a significant increase in reliability is observed. On the other hand, data fusion offers a solid mathematical framework to enhance data quality obtained across either one sensor of multiple channels/frequencies or multiple sensors of completely different physics in terms of data process perspective. The fusion of multiple images is necessary since target location and recognition could be enhanced via the extraction of valuable information from all data sources. By combining images from multiple NDE systems with different physical properties, pixel-level data fusion provides complementary or redundant information about the physical and mechanical properties of a material[109]. The data fusion technique applied here has adopted wavelet decomposition of images at a certain level [110]. The decomposition result is a vector consisting of horizontal/vertical/diagonal detail coefficients, and approximation coefficients. Moreover, the output decomposition structure consists of the wavelet decomposition vector and the bookkeeping matrix, which also contains the number of coefficients by level and orientation. By calculating the average of approximation coefficients respectively in terms of every image, fused images can be reconstructed by a single-level two-dimensional wavelet reconstruction with respect to either a particular wavelet or particular wavelet reconstruction filters that have been specified. In particular, the Haar wavelet has been used for both decomposition and reconstruction algorithms.

The Harr wavelet function $\psi(x)$ can be described as

$$\psi(x) = \begin{cases} 1, & 0 \leq t < 0.5 \\ -1, & 0.5 \leq t < 1 \\ x, & \text{otherwise} \end{cases}$$

Its scaling function $\varphi(x)$ can be expressed as:

$$\varphi(x) = \begin{cases} 1, & 0 \leq t < 1 \\ 0, & \text{othersise} \end{cases}$$

In this way, information has been extracted from data source identically which implies that images with higher resolution are not given with a larger weight regarding fusion process.

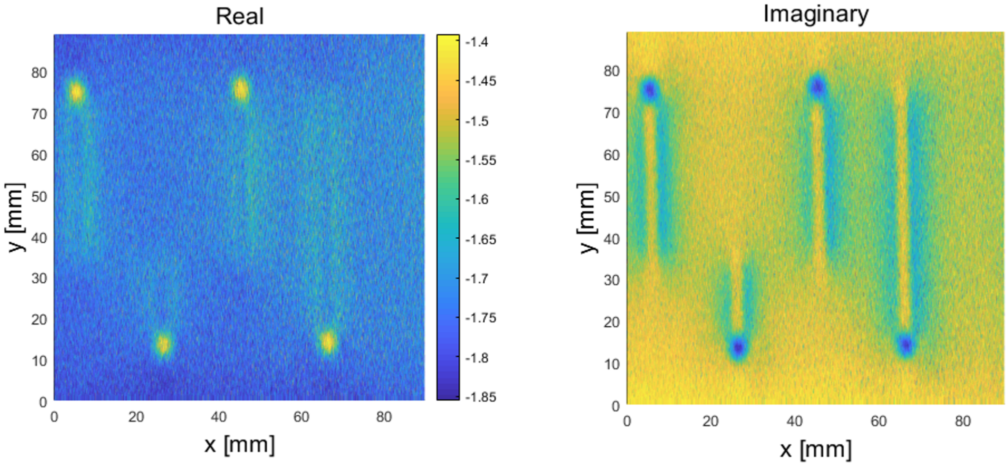

(a) Raw scanning data of GMR sensor at 30KHz

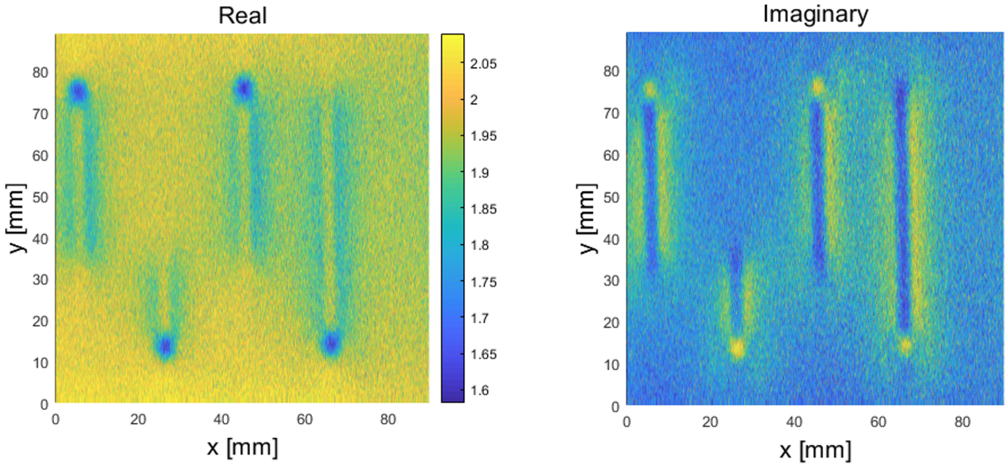

(b) Raw scanning data of GMR sensor at 60KHz

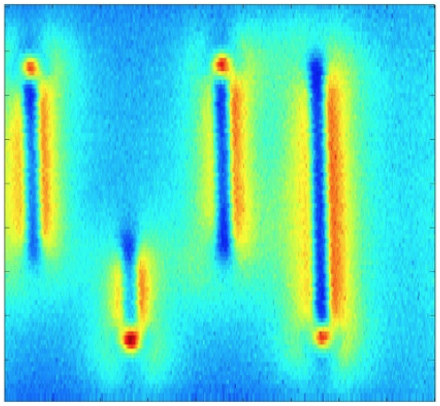

(c) Fused images based on 8 sources with 4 different frequencies for real and imaginary component respectively

Figure 4.27: Raw scanned data and data fusion result.

Each image is transformed prior to fusion using wavelet transformations with Matlab. The major features from each image are kept during the fusion operation, but it was observed that an improvement might result when the quality of the original images is poor, or there is a restriction on the number of images to be fused. In comparison, the fusion of images with identical good qualities may not result in an improvement since complementary information is not provided. As observed from the fused image, local inhomogeneities in composites and defects are clearly shown across the area of interest. It also gives the location and shape of defects. However, the ability of the fusion technique is limited by data source due to the fact that registration or spatial alignment of multiple images has been poorly performed. Thus, the integration or fusion of information extracted from multiple images is reduced.

Through the combination of images from multiple sources with varying physical properties, the goal of pixel-level data fusion is to study information that is complementary or redundant to the physical and mechanical properties of a material. In order to improve the accuracy of detection, a method that aims to extract all the perceptually important features from different original images has been developed. This data fusion method combines the information to form a fused image in such a way that all the key features from each input image are still perceivable.

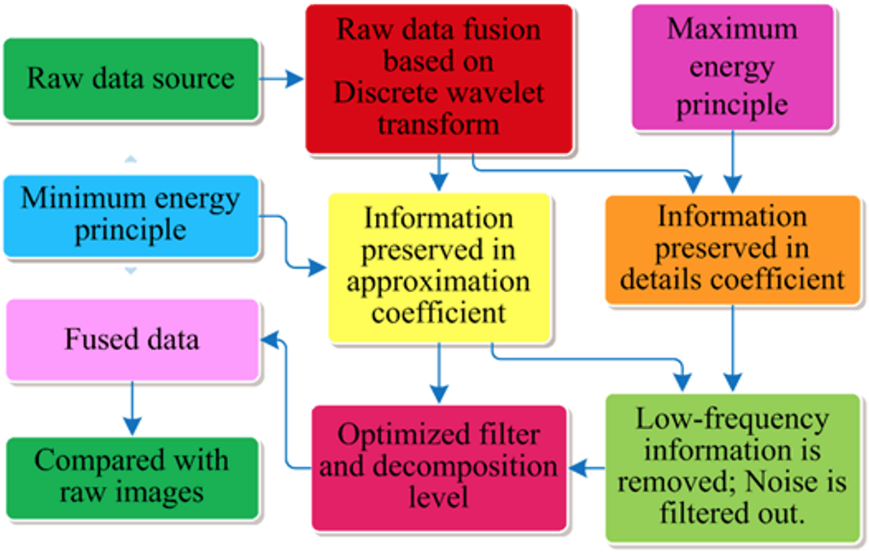

Figure 4.28: Flowchart of data fusion method.

A flowchart of the data fusion method has been shown in Fig.4.28. After selecting the input data, discrete wavelet transform (DWT) will be employed to convert the raw data. DWT-based image fusion consists of two steps: selecting the proper wavelet filters and level of decomposition using formulated parameters and selecting the proper fusion criterion in the wavelet subband. It means that fusion is operated on wavelet domain level via DWT of multiple sources combined with fusion rule, and the fused image is reconstructed by inverse DWT (IDWT). This method fuse images at different frequencies from the eddy current sensor.

$$I = W^{-1}\left[\varphi\left\{W\left(I_1\right) + W\left(I_2\right) + W\left(I_3\right) + \cdots + W\left(I_m\right)\right\}\right]$$

where $I_1, I_2, \ldots, I_m$ are the m images to fuse, φ denotes the fusion rule, and W and W^{-1} represent DWT and IDWT respectively. In order to achieve higher quality, the wavelet filter, level of decomposition, and corresponding fusion rule should be carefully selected.

An energy risk factor is adopted to select the appropriate filter. $E_{\min} = \min_j E_a(j).E_a(j)$ is the energy of approximation coefficient at the j^{th} level of the selected wavelet filter. The wavelet energy represents the percentage of energy corresponding to the approximation and the detail coefficients. $E_{\min}$ denotes the minimum energy of the WAC, which indicate that low-frequency information is removed after decomposition. It is used to filter out the noise and other low-frequency components.

Since useful information could be preserved in low frequencies mixed with noise, the maximized energy within the WDCs is considered. The energy of the denoised image's WDCs cannot be higher than the original raw image. Although energy stored within the WDCs of the denoised image is closer to the energy stored within the WDCs of the raw image, more importance should be given to WDCs in higher frequencies.

The A108 Steel Boiler Sample has been scanned using different kinds of sensors at different frequencies. The selected scanning area includes cracks with 200 µm and 400 µm width.

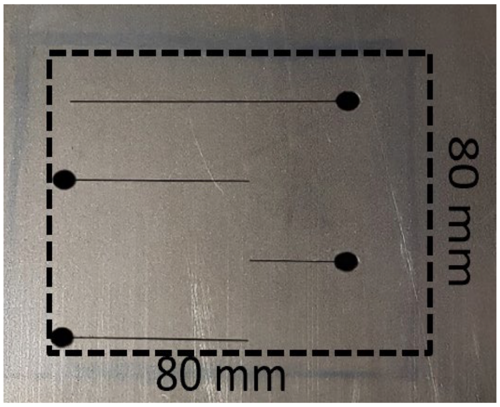

Figure 4.29: The scanning area of the sample.

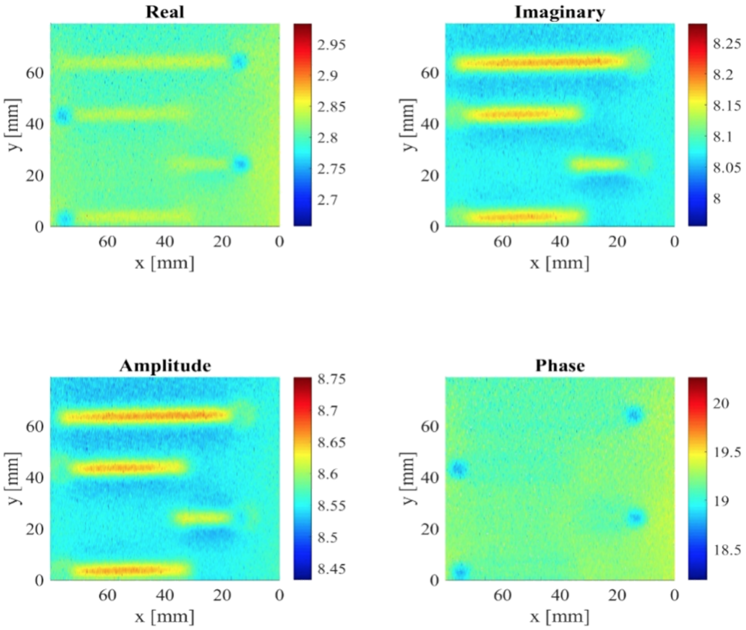

Figure 4.30: Eddy current imaging at 30 KHz.

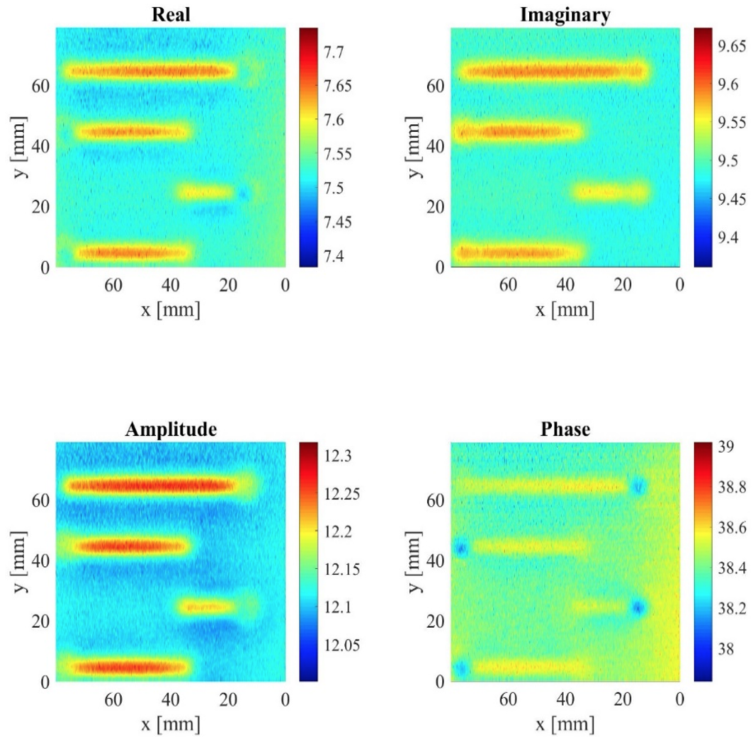

Figure 4.31: Eddy current imaging at 50 KHz.

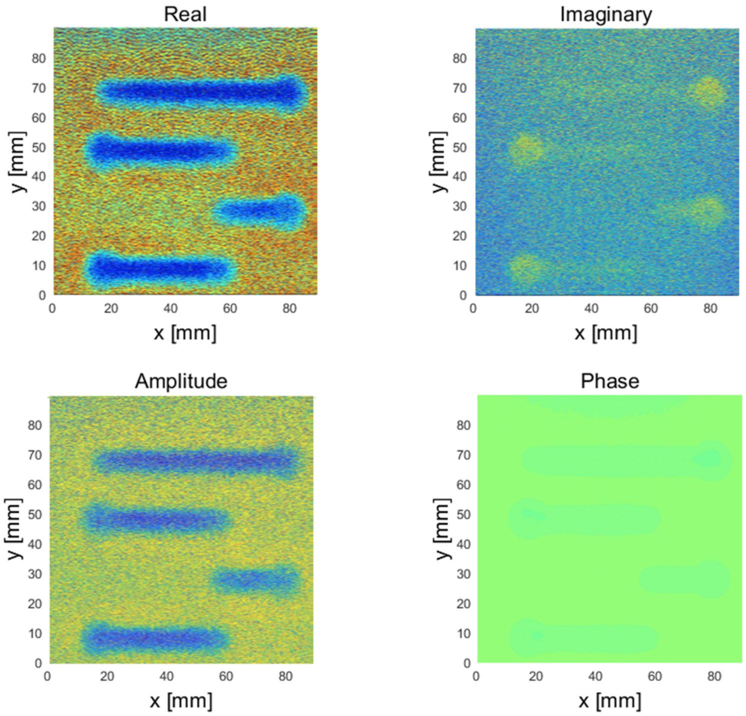

Figure 4.32: GMR sensor imaging at 35 KHz.

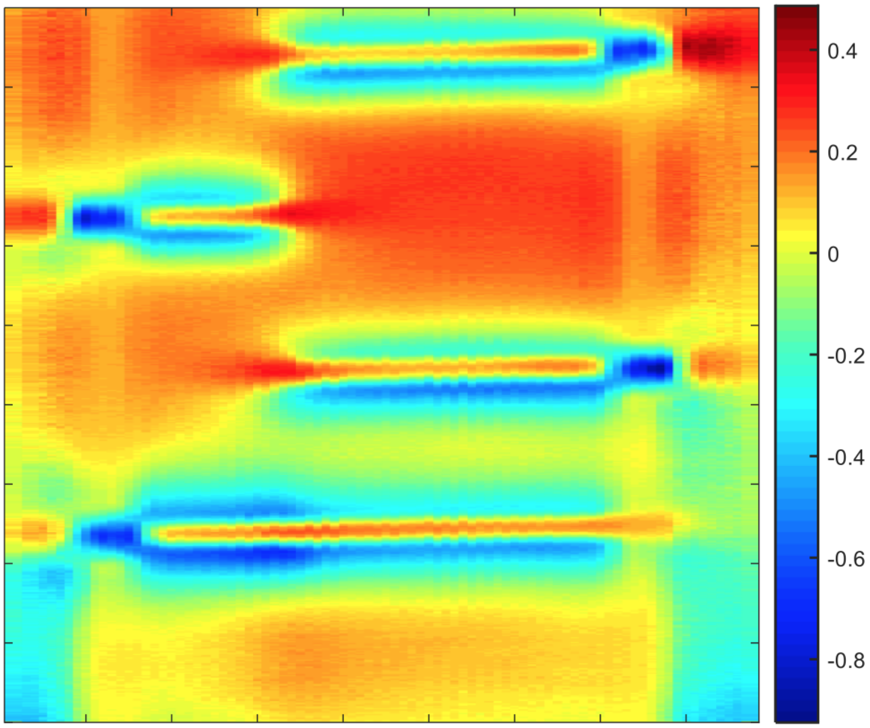

Figure 4.33: Data fusion result of scanning data at different frequencies.

Two 1D plots have been shown below to have a better comparison between raw data and data fusion result. From the figure, the fusion results show that with proper selection of wavelet and fusion procedure, reliability and SNR can be enhanced.

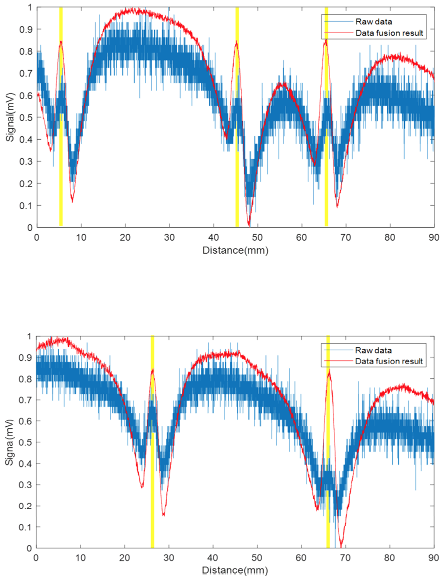

Figure 4.34: 1D plots that compare the raw data and data fusion result. The shading region indicates the location of sub-mm cracks.

4.6 Depth estimation

It is very important to know not only the location but also the size of the cracks. The NDE scanning system on the robot will perform a 2D scanning of the sample. With proper data processing methods, the defects' length and width can be accurately detected. However, the depth of information on the flaws is not that straightforward. In order to have a better depth estimation, both experimental tests and numerical simulations have been studied. A numerical simulation model is developed using Ansys to study the S-parameter change when the sample with different depths of cracks. The model of a single coil is shown below.

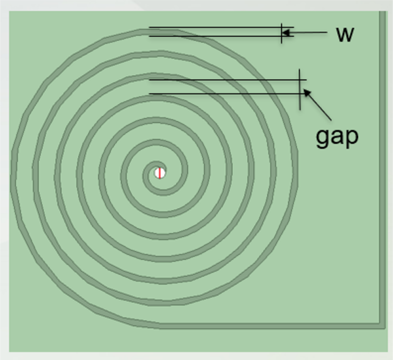

Figure 4.35: Coil simulation model with adjustable parameter gap and width.

A 20 × 20 × 5 (Unit: mm) sample with different depth of the cracks has been place on the top of the coil sensor as shown in Fig.4.28.

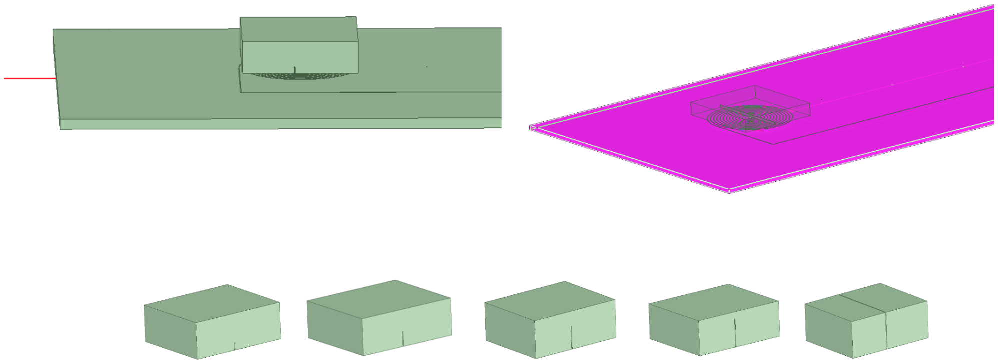

Figure 4.36: The steel samples with different depth of cracks on the top of sensor.

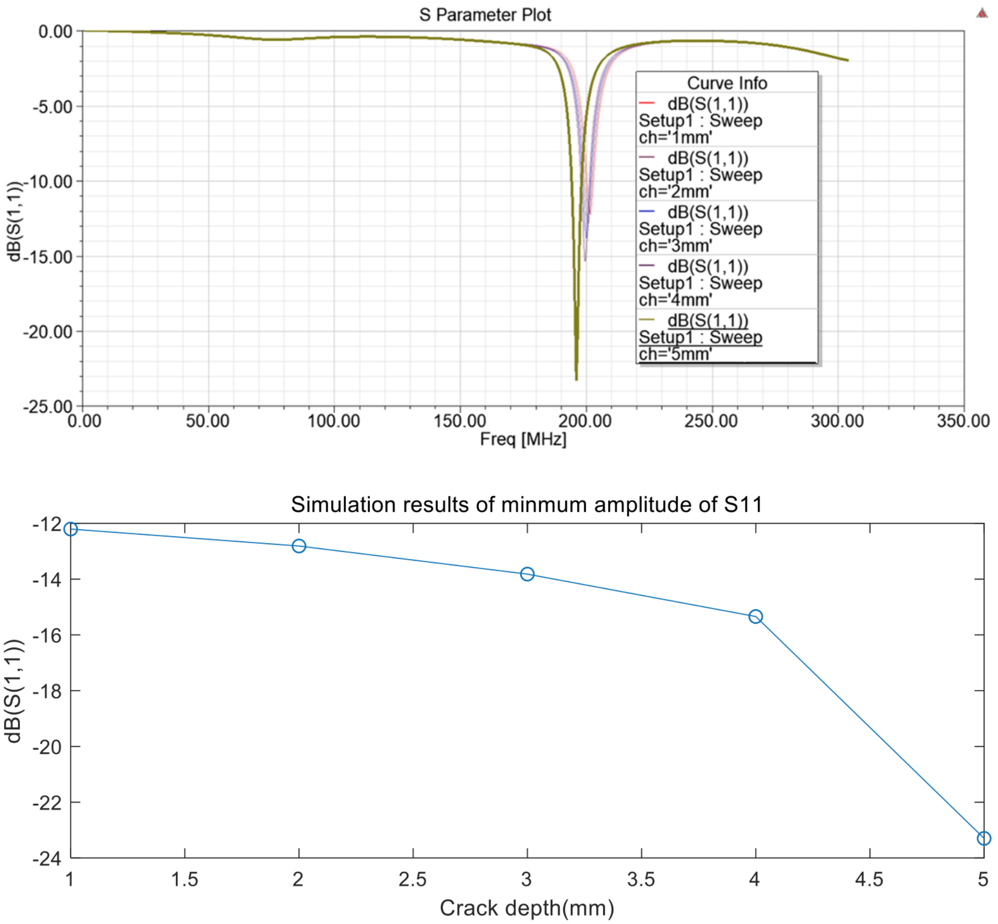

Figure 4.37: S11 simulation results of cracks' depth from 1 mm to 5 mm.

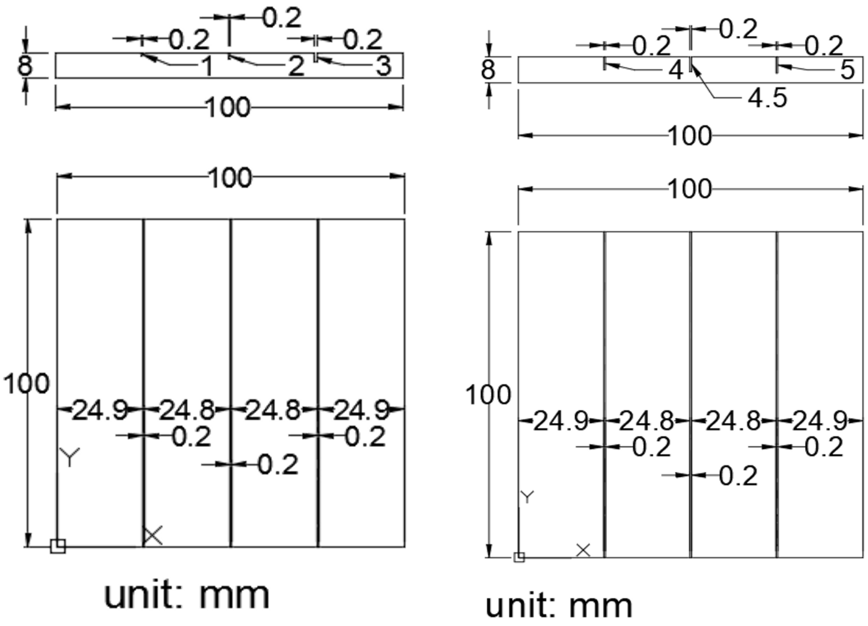

Figure 4.38: Sample design: A3(Q235) steel with 0.2 mm width at different depths.

The sample shown in Fig.4.5 contains only through cracks. In order to study the actual performance of the sensor at different depths, a new sample with different depths of cracks has been fabricated. The material of the sample is Q235 steel. Three 0.2 mm width cracks with depths from 1 to 3 mm have been introduced to sample 1. The cracks on sample 2 are of the same width, but the depths are 4, 4.5, and 5 mm, respectively. The samples have been scanned using an eddy current coil array sensor with a 1 mm lift-off distance. The figure shows that the cracks with different depths can be easily distinguished.

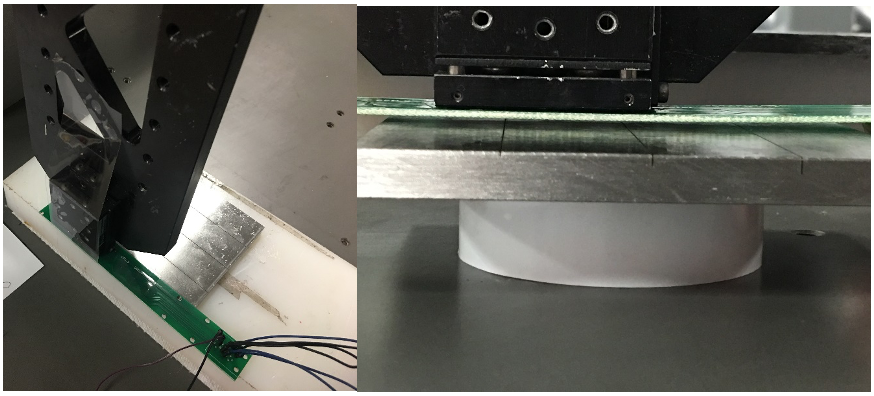

Figure 4.39: Experiment setup with eddy current array sensor.

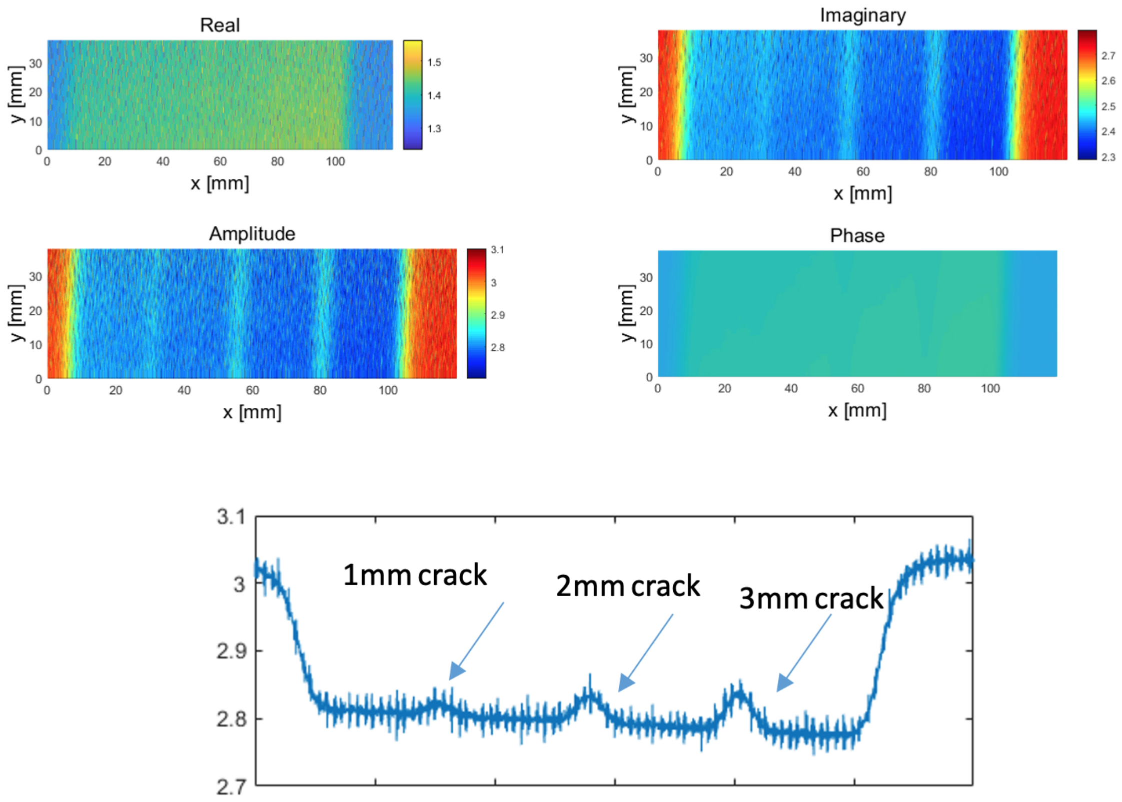

Figure 4.40: 2D and 1D plot of the scanning imaging.

Many constraints need to be considered when designing the NDE sensing system for the robot. The sensor's footprint is limited by the design of the robotic system and the complexity of testing structures. The allowable maximum power consumption of the entire system is constrained by the available power supply unit on the robot. Many environmental conditions could affect the NDE results obtained from the robotic actuating and sensing. Such would add inevitable uncertainties to the acquired data or restrict actuation access, lowering the fidelity and resolution of NDE data used for further damage assessment and analysis. To overcome these aforementioned challenges and obtain optimized sensing outcomes, the proposed NDE sensors were customized to fit the robotic system and workspace environment for power plant boiler inspection. These optimizations lead to a low-cost, lightweight, non-contact, and simplified NDE setup. To achieve the optimized scanning performance, a parametric study of the coil design has been done using Ansys HFSS. The simulation studies focus on the sensor's sensitivity to the very narrow cracks (the width of the crack is less than 0.2 mm) on the boiler wall as well as the sensor's scanning area. A sensor with better sensitivity to the interested defect will provide a better signal-to-noise ratio, and a sensor with a larger scanning area will reduce the scanning time. Two identical coils are simulated with steel plates present on the top of the coil, as shown in Figure 4.41. The lift-off distance is 1 mm. A crack (0.1 mm × 15 mm) has been introduced to one of the steel plates. The parametric sweep study simulates different coil dimensions such as the line space, line width, and the number of turns.

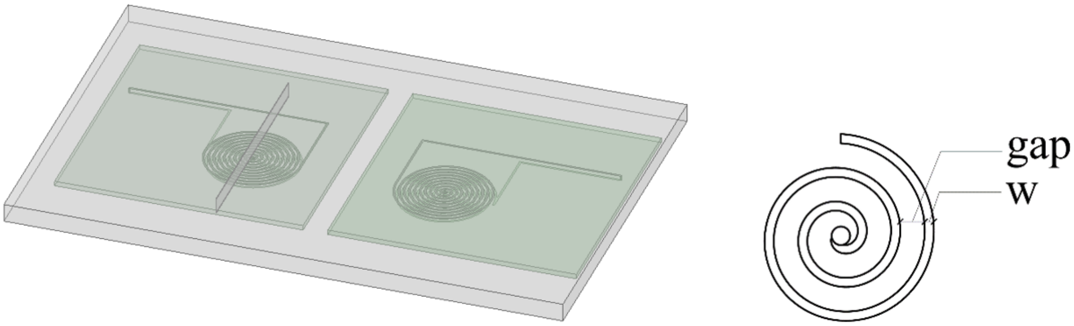

Figure 4.41: The simulation geometry model. Two identical coils are simulated to study the different signal respond from the healthy region and the defective region.

The sensor's sensitivity can be depicted by resonating frequency's magnitude difference when comparing the healthy and defective regions' scanning data, as shown in Fig.4.42 (a). A general trend can be observed that as the number of turns increases, the sensitivity of the sensor decreases. However, there is a trade-off between the scanning area and the sensor's sensitivity, as shown in Figure 4.42 (b). Therefore, a multi-channel eddy current array has been designed and employed, which allows for surface and subsurface anomaly detection while meeting the optimization requirements. As shown in Figure 4.43, a compact NDE system with a four-by-two sensor array has been fabricated.

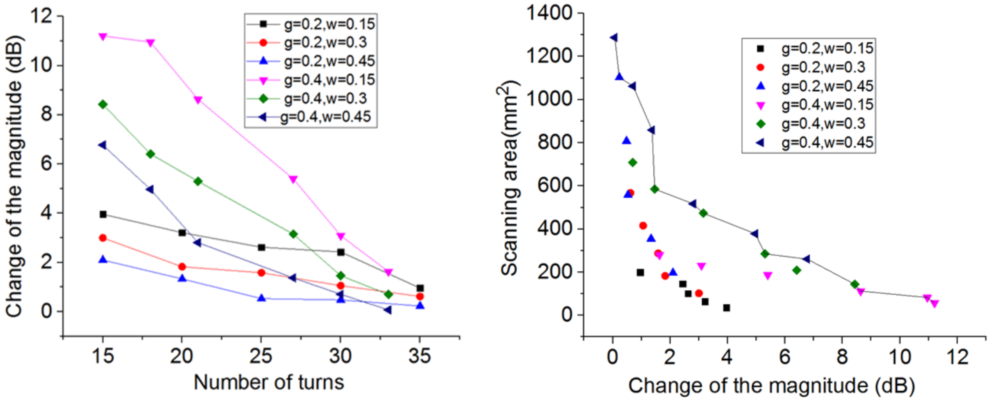

Figure 4.42: The simulation results of the different dimensions' coils on the healthy and defective samples. (a) The magnitudes change at the resonating frequency and (b) the Pareto front of maximizing the scanning area and the sensitivity of the scanning system.

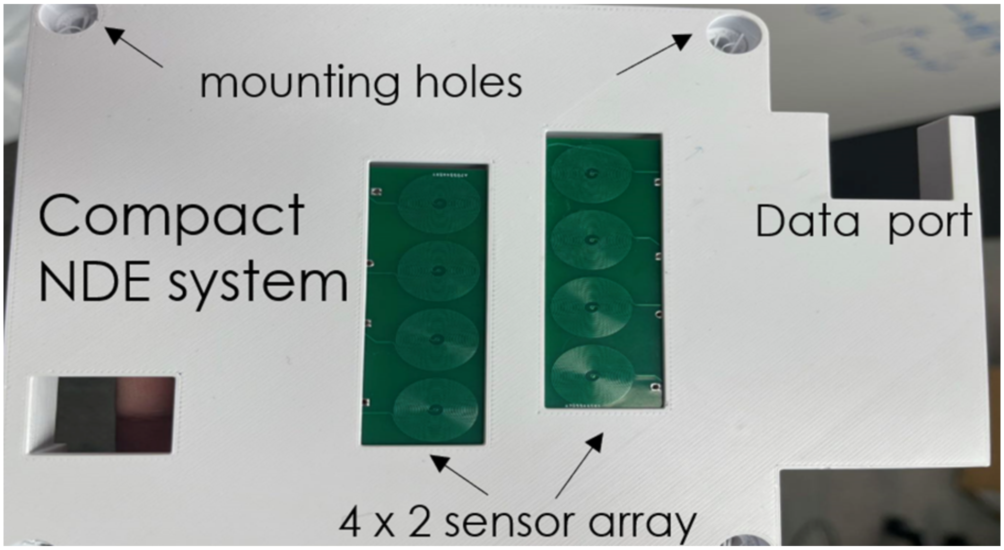

Figure 4.43: The compact NDE system to be mounted on the robot. The sensor array includes 4 by 2 18 turns coils with trace spacing as 0.4 mm and trace width as 0.15 mm.

In order to validate the performance of the proposed sensor, the same steel samples with EDM cracks of various depths were placed side by side and scanned using the designed eddy current coil array sensor with a well-maintained 1 mm lift-off distance. The line scan results for the two samples are shown in Figure 4.44. All cracks have been successfully detected quantitatively, where different shifts of eddy current sensor's resonating frequencies correlate to different depths of the narrow crack.

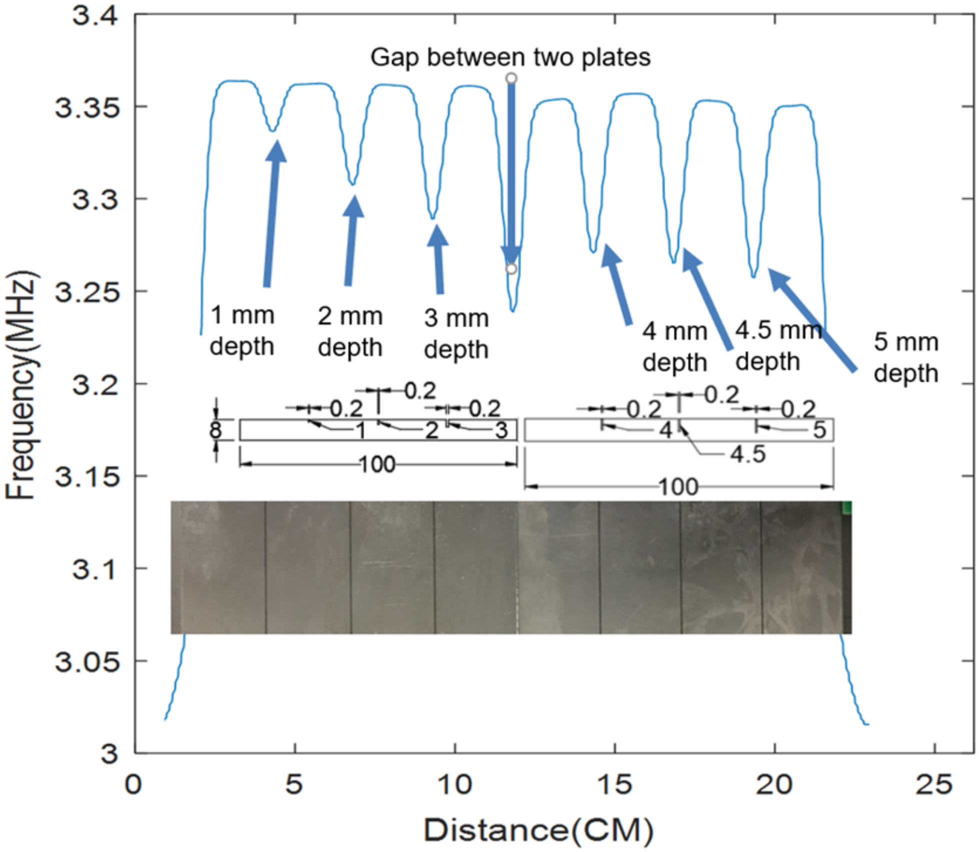

Figure 4.44: The single channel line scan result of the two steel plates with cracks at different depths.

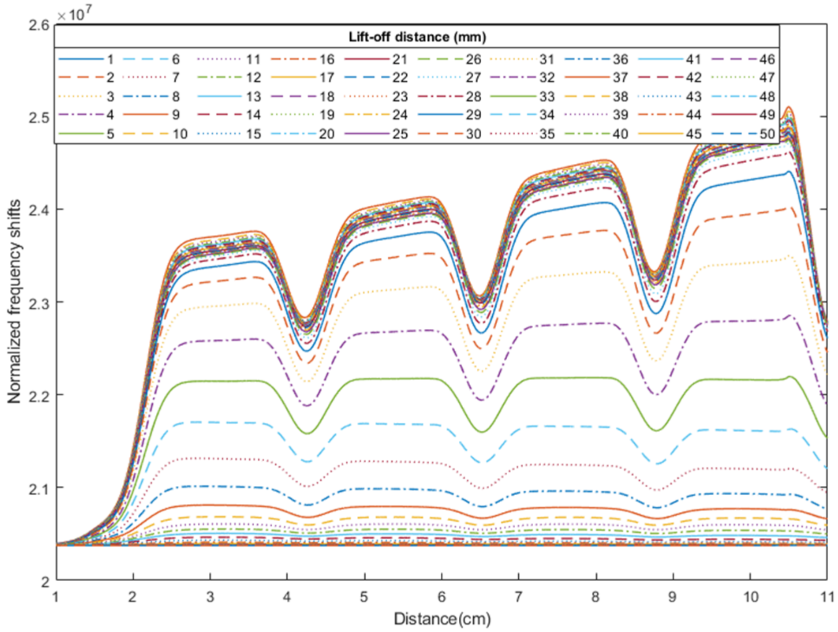

Figure 4.45: Normalized frequency shifts with different lift-off distance of the eddy current sensor.

CHAPTER 5

CONCLUSION AND FUTURE PLAN

5.1 Conclusion

In this work, multiple electromagnetic NDE methods have been studied. The NDE system have been developed, validated, and applied to these complex applications. The research has resulted in the following contributions to the field of electromagnetic NDE.

1) The development and improvement of the Near-field microwave imaging system. The system is able to obtain high-resolution (sub-wavelength) and sub-surface information of the OUT. The strain of sample has been evaluated by a multi-modality data fusion technique through simulations and experiments. The results show the great potential of the developed system as a tool for strain estimation.

2) A root phenotyping system has been designed and optimized for non-destructive root phenotyping with the potential of in-situ monitoring. The system employs an array of ultra-wideband microwave antennas to perform low-cost and non-contact scanning. Based on the collected signal, the system is able to determine the position and shape of the roots with the soil's background noise. A computationally efficient signal processing method based on the non-iterative TR algorithm provides the capability of rapid root localization. Its fast scanning speed and high level of robustness allow the microwave imaging technique to be deployed on the ground to scan large soil areas and determine the health of roots in real-time.

3) A portable NDE sensing system has been designed to meet a variety of scanning requirements. The proposed NDE sensors were customized to fit in the robotic system and workspace environment for power plant boiler inspection. These optimizations lead to a low-cost, lightweight, non-contact, and simplified NDE setup.

5.2 Future Plan

In addition, the remaining work can be pursued in the coming years:

1). More experiments need to perform for the strain estimation with different materials and conditions to provide comprehensive studies of the relation between NMHI data and strain properties.

2). The design of the probe should be optimized to improve its performance for complex geometry inspection.

3). More mechanical properties should be studied.

4). Although the proposed root phenotyping system has been studied numerically and validated experimentally in the lab, it has not been tested on a natural plant in the field. The system needs to be further developed and extensively tested.

5). Further improvement in sensitivity and signal-to-noise ratio also needs to be addressed.

6). The real-time monitoring of the plant's roots growing in the soil would be an exciting topic. Also, to better understand the phenotype of the plants, the study should be performed for multiple generations of the plants.

7). A suitable mechanical structure needs to be developed to reduce the change of lift-off distance during the scan to increase the signal-to-noise ratio.

8). The sensor parameters, including the diameter, number of turns, and array design, should be optimized to provide better performance.

9). A post-processing algorithm for quantitative feature extraction for crack sizing(such as depth and width) and localization information should be developed.

APPENDIX

APPENDIX

REVIEW OF THE NDE METHODS OF ADDITIVE MANUFACTURING

A.1 Background

Additive Manufacturing (AM) is the process of building up parts directly from 3D model data by joining materials one layer upon another layer [17]. As opposed to traditional subtractive manufacturing methodologies, which use cutting tools removing materials from a larger metal, AM print the component by adding materials together. It allows AM to produce complex geometries and internal features which cannot be manufactured using subtractive methods [18]. In addition, AM using a computerized 3D model which allows design optimization and efficient use of raw materials. By eliminating the production steps, AM can reduce material waste, energy and time costs by up to 90% [19]. According to NASA [20], AM can save more than eight months compared to traditional manufacturing when building a rocket injectors. It also able to manufacture customized parts according to different demands. The parts can be produced directly from the designed 3D model, without the need for expensive and time-consuming part tooling and prototype fabrication [21].

With fewer constraints on product design and more flexibility, AM makes it possible to produce single consolidated object instead of separated parts. Since the late 1980s, the AM has been developed rapidly [22], and it also has been called as Rapid Prototyping [23]. 3-Dimensional Printing, Solid Freeform Fabrication or Desktop Manufacturing [24], which express the characteristics of this method from different aspects. It also uses a wide range of materials such as metals, polymers, composites, and biological tissues. This review mainly focuses on the Metallic Additive Manufacturing (MAM).

A.2 Metallic Additive Manufacturing

As an advanced and complicated technology, MAM is one of the most important Research Directions. More and more researchers start to focus on manufacturing complex-shaped metal components due to the urgent demands from the automotive [111], aerospace [112, 113], and rapid tooling industry [114, 115]. MAM can be categorized in terms of the Material Types, Material Feed Methods, Energy Source, etc. [116, 117, 118, 119, 120, 121, 122]. Currently, most MAM methods using titanium or nickel alloys as materials. As shown in fig.A.3, the material feed methods can be mainly divided into three broad categories: (i) powder bed systems, (fig.A.1) (ii) powder feed systems (fig.A.2), and (iii) wire feed systems [118].

The Energy Source of MAM usually includes electron beam, laser beam and arc. The main applications of the arc are the efficient and rapid forming of the large size complex components. The electron beam and laser beam mainly focusing on precise forming of small size components.

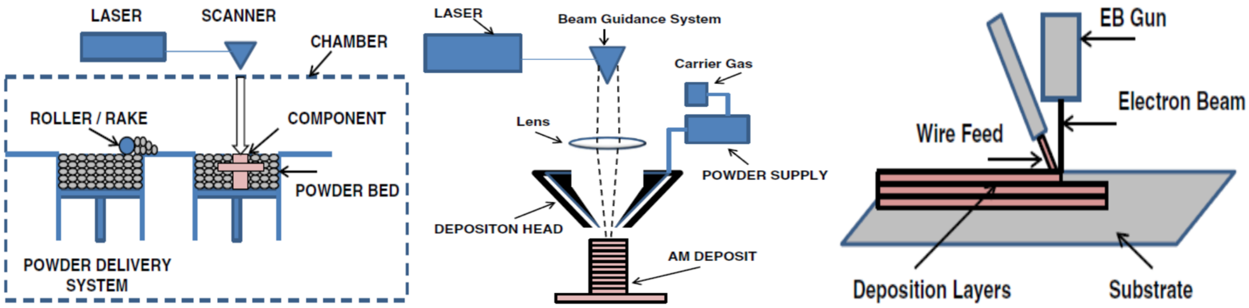

Figure A.1: Generic illustration of an (a) AM powder bed system (b) AM powder feed system (c) AM wire feed system [8].

Depending on the methods of deposition, laser MAM technology can be divided into two major categories: (1) put the metal powder into the heating pool before deposition such as Direct Metal Laser-Sintering (DMLS) and Selective Laser Melting (SLM). The metal powder is preliminarily spread in the deposition area, and the powder is melted layer by layer using a laser source which moves according to the pre-planned scanning path and forms the parts directly. A schematic example of the SLS system is shown in the fig.1.2 [9]; (2) the metal material is sent into the bath in real time during the deposition, such as Laser Direct Metal Deposition (DMD) and Engineered Net Shaping (LENS).

Selective Laser Sintering(SLS) is the fundamental method uses a low-power-density laser as thermal energy to sinter powdered material in the selected areas. The laser beam aims at the points predefined in in CAD model, processes the material to connect together and creates a solid structure. It was first purposed by Carl Deckard in 1987 [123]. As shown in the fig.A.2, the system of SLS usually contains three main components: 1) laser source and scanning control; 2) powder feed control; 3) atmosphere control systems;

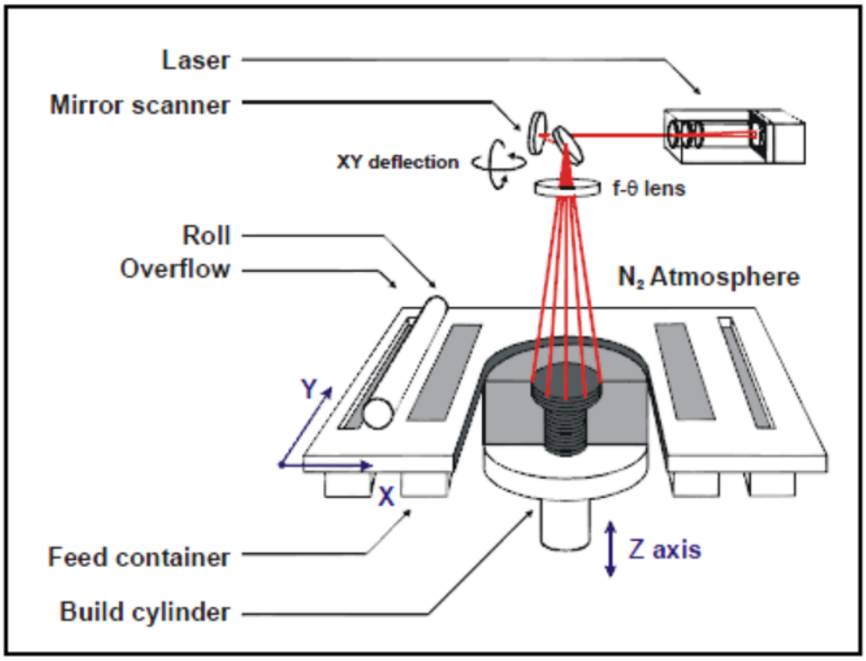

Figure A.2: A typical SLS machine layout [9].

The metallic powder used in the SLS technology is a mixture of treated and low melting metal or polymer materials, and the molten material with a low melting point during the processing process but the high melting point metal powder is not melted. The use of molten material to achieve bonding molding.

The SLM uses a comparable concept but with a higher power source to fully melt the material instead of sinter. This allows SLM to manufacture parts with better density and strength.

A.3 Reason Need NDE

Although AM is able to offer so many impressive benefits, there are still a lot of technical barriers and challenges that need to be overcome. As a novel technology, it not only redefines the way of manufacturing but also redefines the way of testing and evaluating products. When additive-made parts are used in some critical applications and have a direct impact on the safety and success of a project, it is crucial to ensure their quality and reliability. However, the parts produced by AM are often complex in shape and manufactured in one piece directly. These parts usually combine hundreds or thousands of individual layers which are melted by energy source and deposited upon each other. Many of the process variables such as printing speed, energy distribution, substrate and atmosphere will have a complex interaction and influence the parts quality. Therefore, it is difficult to test and evaluate AM parts using conventional methods without affecting the part.

The performance of the AM parts is highly related to its microstructure and the presence of defects [124]. Unexpected cracks, bonding between layers or undesired porosity will result in poor building quality and have a negative influence on the performance. To improve and ensure the quality of AM produced parts, a multi-disciplinary approach that includes knowledge from both AM and NDE is required. The challenges related to the material properties and in-situ monitoring are consistently considered as the most important task to improve the AM process. NDE methods can be potential applications in both materials characterization and in-process monitoring. For materials characterization, the NDE can be performed on the raw input materials such as the metal powder or wire. Evgueni [125] presented the measurement of electromagnetic properties of the AM powder and solid material using eddy current and studied the effect of the magnetic powder properties of AM. For those parts used in the critical areas such aero-engines, the performance must be evaluated before it comes into operation. The properties of AM produced parts can also be evaluated by NDE, such as the dimensions and mechanical properties.

For the in-situ monitoring, NDE techniques have exciting potential to measure and monitor in-processing parts. A significant enhancement of AM parts' quality will be achieved with the improvement of the in-process control. If the NDE sensors could be successfully applied to a MAM system, then it will be able to measure the dimensions of each layer of the parts, right after it is formed. The presence of defects during the process can be detected immediately, and the system might be able to fix the defects with real-time adjustments when the part is still under processing. Compared to post-process inspection, which will be only able to reject the completed flawed parts, in-situ NDE monitoring shows its potential to have a significant impact on the AM industry. The

Fig.A.3 shows the some of NDE methods that can be applied to AM quality control.

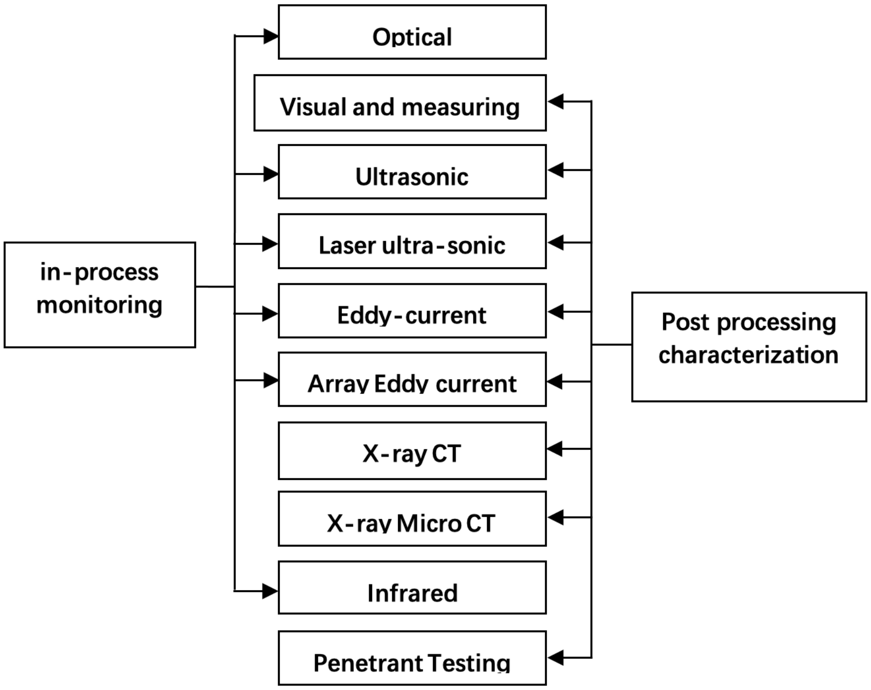

Figure A.3: Methods of NDE applicable for in-process monitoring and post-process characterization.

A.3.1 Common defects in AM

MAM can generally be considered as a process of metal deposition. During the welding, it will potentially introduce the defects that connected with a discontinuity, such porosity, cracks, bonding between layers, balling and unfused powder. The fig.1.2 shown the three most common defects of SLM fabricated parts.

The spherical pores are usually due to the entrapped gas in the material and the typical sizes are between $5 - 20\mu m$ [126, 127]. Lack of fusion will result in the bonding between layers which usually between $50-500\mu m$ [127, 128]. Cracks may occur when removing the component from the platform or due to the residual stress within the component. Sometimes, the melted powder forms a ball-shaped grain on the surface instead of forming a flat layer [129, 130, 131, 132, 133, 134]. The powder may not be fully melted so the printed part would also include unfused powder [134].

To prevent these defects causing critical failures, people developed all kind of detecting methods to evaluate the printed objects.

A.4 Visual measuring and Optical Scanning

Visual and measuring can be considered as the most commonly used inspection method and it is usually the first step to evaluating the parts. With the help of measurement tools and accessories, the information such as profile gauges can be obtained. Usually, only the surface information can be evaluated when checking the non-transparent parts. However, for AM parts, the optical information of each layer is obtainable by using remote visual systems. As shown in the fig.A.4, to obtain the optical information of each layer, a system with a visual camera is proposed in [135].

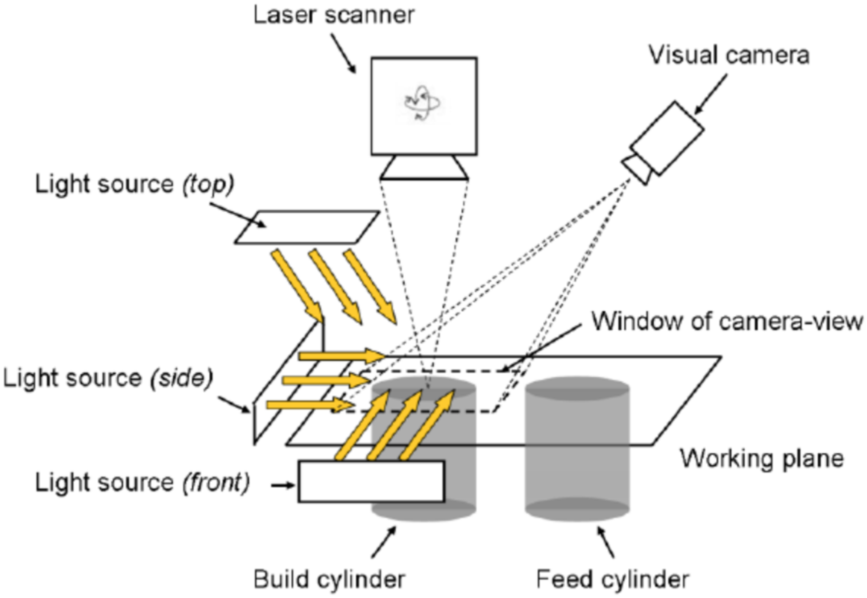

Figure A.4: Schematic of an in-situ monitoring system with a visual camera [10].

Three light sources projecting the light on the powder bed and a high-resolution camera to records the deposition of powder layers. This system aims to detect the defects in the manufacturing at the earliest possible stage so corrective actions can be taken in time. Clijsters et al. developed a similar system that includes a high-speed CMOS camera which captures wavelength in the range of 780 nm to 950 nm [10]. Lower thermal resistance will be represented by a dark zone in the recorded data. The sample rate of the system is from 10 kHz to 20 kHz. The scanning results show the capability of this method that able to detect and identify large pores.

Although a lot of monitoring methods have been designed, only a few of studies employing closed loop control to improve the quality of the AM parts. To solve the discontinuities caused by over-melting, Mireles et al. [67]proposed an automated feedback control system which maintains the build temperatures. Instead of simply recording and processing the images, this system able to control the parameter of the printing machine and attempt to stable the temperature at a certain range. However, the closed loop system still need to be improved. This will require more priori knowledge of the material and build process.

A.5 X-Ray Computed Tomography Technique

Computed tomography (CT) is generally used NDE technique for AM parts inspection. It able to inspect the entirety of the sample, regardless of the complexity of the geometry. It is also able to detect embedded defects and interrogate inaccessible features which offers the information of the internal structure. It has become the main detection method in NASA. Traditional detection method such as ultrasonic, X ray, eddy current and penetration technology are only used as auxiliary methods [136].

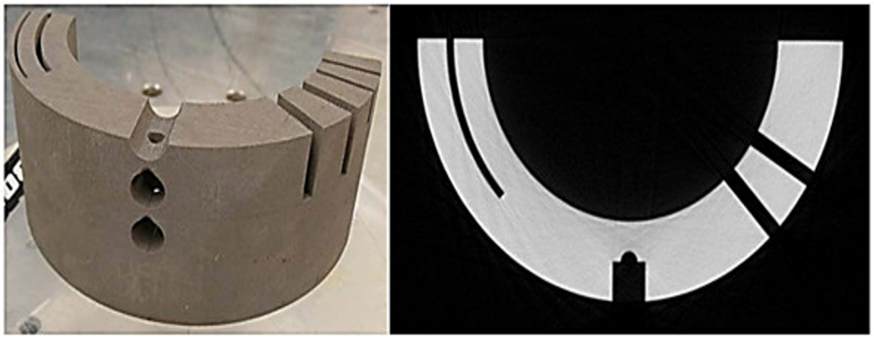

Figure A.5: CT scan result of a DLMS aluminum gauge sample.

As shown in the fig.A.5, an aluminum gauge sample printing using DLMS is showing in the left image and the CT scanned result is shown in the right image. It shows a one-layer information with very high contrast and good resolution of the sample.

However, there are still some limitations of CT. It is not very cost-effective especially for a large sample and it is also a time-consuming method. If the cracks are oriented perpendicular to the beam, then the detecting results may not be accuracy. Also, the increasing of scanning depth will result in the decreasing of the scanning resolution. Therefore, the small pores deeply embedded in the sample may not be correctly detected. In addition, the size of the sample under evaluation are limited by the CT system.

BIBLIOGRAPHY

BIBLIOGRAPHY

[1] G. Ziółkowski, E. Chlebus, P. Szymczyk, and J. Kurzac. Application of x-ray ct method for discontinuity and porosity detection in 316l stainless steel parts produced with slm technology. *Archives of Civil and Mechanical Engineering*, 14(4):608–614, 2014.

[2] NA Zanjani and S Kalyanasundaram. Experimental and numerical studies on forming and failure behaviours of a woven self-reinforced polypropylene composite. *Advanced Composite Materials*, 30(2):116–130, 2021.

[3] L. Thijs, F. Verhaeghe, T. Craeghs, J. V. Humbeeck, and J. P. Kruth. A study of the microstructural evolution during selective laser melting of ti-6al-4v. *Acta Materialia*, 58(9):3303–3312, 2010.

[4] P. Nilsson, A. Appelgren, P. Henrikson, and A. Runnemalm. Automatic ultrasonic testing for metal deposition. In *18th World Conference on Nondestructive Testing*, Durban, South Africa, 2012.

[5] Noriko Read, Wei Wang, Khamis Essa, and Moataz M. Attallah. Selective laser melting of alsi10mg alloy: Process optimisation and mechanical properties development. *Materials & Design (1980-2015)*, 65:417–424, 2015.

[6] Philipp von Gillhaußen. *Testing the potential of priority effects to sustainably increase community function in semi-natural grasslands*. PhD thesis, 2015.

[7] Rainer Pohl, A Erhard, H.-J Montag, H.-M Thomas, and H Wüstenberg. Ndt techniques for railroad wheel and gauge corner inspection. *NDT & E International*, 37(2):89–94, 2004.

[8] William E. Frazier. Metal additive manufacturing: A review. *Journal of Materials Engineering and Performance*, 23(6):1917–1928, 2014.

[9] J.P. Kruth, P. Mercelis, J. Van Vaerenbergh, J. van Vaerenbergh, L. Froyen, and M. Rombouts. Binding mechanisms in selective laser sintering and selective laser melting. *Rapid prototyping journal*, 11(1):26–36, 2005.

[10] Stijn Clijsters, Tom Craeghs, Sam Buls, Karolien Kempen, and Jean-Pierre Kruth. In-situ quality control of the selective laser melting process using a high speed, real-time melt pool monitoring system. *International Journal of Advanced Manufacturing Technology*, 75(5-8):1089–1101, 2014.

[11] Edward Chlebus, Bogumiła Kuźnicka, Tomasz Kurzynowski, and Bogdan Dybała. Microstructure and mechanical behaviour of ti-6al-7nb alloy produced by selective laser melting. *Materials Characterization*, 62(5):488–495, 2011.

[12] ISO 25178-2. Geometrical product specifications (gps) – surface texture: Areal – part 2: Terms, definitions and surface texture parameters, 2012. International Organization for Standardization.

[13] ISO 25178-3. Geometrical product specifications (gps) – surface texture: Areal – part 3: Specification operators, 2012. International Organization for Standardization.

[14] H. Taud, R. Martinez-Angeles, J.F. Parrot, and L. Hernandez-Escobedo. Porosity estimation method by x-ray computed tomography. *Journal of Petroleum Science and Engineering*, 47(3):209–217, 2005.

[15] Charles J Hellier. *Handbook of nondestructive evaluation*. McGraw-Hill Education, 2013.

[16] Peter J Shull. *Nondestructive evaluation: theory, techniques, and applications*. CRC press, 2002.

[17] Pat Picariello. Astm committee f42 on additive manufacturing technologies. *Standard Terminology for Additive Manufacturing Technologies*, 2012. ASTM International.

[18] Ian Gibson, David Rosen, and Brent Stucker. *Additive manufacturing technologies: 3D printing, rapid prototyping, and direct digital manufacturing, second edition*. Additive manufacturing technologies: 3D printing, rapid prototyping, and direct digital manufacturing, second edition, New York, 2015.

[19] Luczkow, Anna, and M. Haute off the press: Refashioning copyright law to protect american fashion designs from the economic threat of 3d printing. *Minnesota Law Review*, page 1131, 2015.

[20] J Waller, B Parker, B Dutton, K Hodges, J Walker, D Wells, E Burke, E Generazio, E Todorov, and A Price. Qualification of products fabricated via additive manufacturing using nondestructive evaluation. Technical report, NTRS - NASA Technical Reports, 2016.

[21] Richard H Crawford and Joseph J Beaman. Solid freeform fabrication. *IEEE Spectrum*, 36(2):34–43, 1999.

[22] T. Wohlers and T. Gornet. History of additive manufacturing. *3D Printing and Its Impact on the Production of Fully Functional Components: Emerging Research and Opportunities*, 24(2014):118, 2012.

[23] E Todorov, R Spencer, S Gleeson, M Jamshidinia, and S. M Kelly. America makes: National additive manufacturing innovation institute (namii) project 1: Nondestructive evaluation (nde) of complex metallic additive manufactured (am) structures. *U.S. Government Science and Technology Report*, 2014.

[24] Richard H Crawford and Joseph J Beaman. Solid freeform fabrication. *IEEE Spectrum*, 36(2):34–43, 1999.

[25] Rabi Sankar Panda, Prabhu Rajagopal, and Krishnan Balasubramaniam. Rapid guided wave inspection of complex stiffened composite structural components using non-contact air-coupled ultrasound. *Composite Structures*, 206:247–260, 2018.

[26] Nick Eleftheroglou, Dimitrios Zarouchas, Theodoros Loutas, Rene Alderliesten, and Rinze Benedictus. Structural health monitoring data fusion for in-situ life prognosis of composite structures. *Reliability Engineering and System Safety*, 178:40–54, 2018.

[27] Xiaodong Shi, Vivek T Rathod, Saptarshi Mukherjee, Lalita Udpa, and Yiming Deng. Multi-modality strain estimation using a rapid near-field microwave imaging system for dielectric materials. *Measurement*, 151:107243, 2020.

[28] Kula E. *stress and stress relaxation*. Springer Science Business Media.

[29] K.-C.T. Nguyen L.H.Le Y. Zhang, P.-Y. Ben Jar. Characterization of ductile damage in polyethylene plate using ultrasonic testing. *Polymer Testing*, 62:51–60, 2017.

[30] A. D. Cinson S. E. Cumblidge M. T. Anderson S. L. Crawford, S. R. Doctor. Preliminary assessment of nde methods on inspection of hdpe butt fusion piping joints for lack of fusion. In *Proceedings of the ASME 2009 Pressure Vessels and Piping Division Conference*, pages 219–224, 2009.

[31] H Aben, L Ainola, and J Anton. Integrated photoelasticity for nondestructive residual stress measurement in glass. *Optics and lasers in engineering*, 33(1):49–64, 2000.

[32] N. McCormick and J. Lord. Digital image correlation. *Materials Today*, 13(12):52–54, 2010.

[33] Kunjalata Kalita, Nipan Das, P. K. Boruah, and Utpal Sarma. Design and uncertainty evaluation of a strain measurement system. *MAPAN*, 31(1):17–24, Mar 2016.

[34] Shoichi Yasukawa. X-ray stress measurement method and apparatus, February 10 2015. US Patent 8,953,743.

[35] W Szymański and M Lech-Grega. Validation of the x-ray stress measurement method. *Advances in Materials Science*, 14(4):102–109, 2014.

[36] Deepak Kumar, Saranraj Karuppuswami, Yiming Deng, and Premjeet Chahal. A wireless shortwave near-field probe for monitoring structural integrity of dielectric composites and polymers. *NDT and E International*, 96:9–17, 2018.

[37] T. R. Filanc-Bowen, Geun Hyung Kim, and Y. M. Shkel. Novel sensor technology for shear and normal strain detection with generalized electrostriction. In *SENSORS, 2002 IEEE*, volume 2, pages 1648–1653, 2002.

[38] Kwok L. Chung, Chunwei Zhang, Yuanyuan Li, Li Sun, and Mohamed Ghannam. Microwave non-destructive inspection and prediction of modulus of rupture and modulus of elasticity of engineered cementitious composites (eccs) using dual-frequency correlation. *Sensors*, 17(12), 2017.

[39] HM Xie and YL Kang. Digital image correlation technique. *Optics And Lasers In Engineering*, 65:1–2, 2015.

[40] Bing Pan, Kemao Qian, Huimin Xie, and Anand Asundi. Two-dimensional digital image correlation for in-plane displacement and strain measurement: a review. *Measurement Science and Technology*, 20(6):062001, 2009.

[41] Bing Pan, Kemao Qian, Huimin Xie, and Anand Asundi. Two-dimensional digital image correlation for in-plane displacement and strain measurement: a review. *Measurement Science and Technology*, 20(6):062001, 2009.

[42] Yiming Deng and Xin Liu. Electromagnetic imaging methods for nondestructive evaluation applications. *Sensors*, 11(12):11774–11808, 2011.

[43] S. Mukherjee, X. Shi, L. Udpa, S. Udpa, Y. Deng, and P. Chahal. Design of a split-ring resonator sensor for near-field microwave imaging. *IEEE Sensors Journal*, 18(17):7066–7076, 2018.

[44] Joongsuk Park and C. Nguyen. An ultrawide-band microwave radar sensor for nondestructive evaluation of pavement subsurface. *IEEE Sensors Journal*, 5(5):942–949, 2005.

[45] Mohammed Saif ur Rahman, Abdallah Yassin, and Mohamed A Abou-Khousa. Microwave imaging of thick composite structures using circular aperture probe. *Measurement Science and Technology*, 29(9):095403, 2018.

[46] Saptarshi Mukherjee, Lalita Udpa, Satish Udpa, and Edward J Rothwell. Target localization using microwave time-reversal mirror in reflection mode. *IEEE Transactions on Antennas and Propagation*, 65(2):820–828, 2017.

[47] E. H. Synge. A suggested method for extending microscopic resolution into the ultra-microscopic region. *The London, Edinburgh, and Dublin Philosophical Magazine and Journal of Science*, 6(35):356–362, 1928.

[48] E. A. ASH and G. NICHOLLS. Super-resolution aperture scanning microscope. *Nature*, 237(5357):510–512, 1972.

[49] Yasuo Cho, Koya Ohara, Atsushi Koike, and Hiroyuki Odagawa. New functions of scanning nonlinear dielectric microscopy –higher-order measurement and vertical resolution–. *Japanese Journal of Applied Physics*, 40(5S):3544, 2001.

[50] Chen Gao, Tao Wei, Fred Duewer, Yalin Lu, and X. . Xiang. High spatial resolution quantitative microwave impedance microscopy by a scanning tip microwave near-field microscope. *Applied Physics Letters*, 71(13):1872–1874, 1997.

[51] H. Bakli, K. Haddadi, and T. Lasri. Interferometric technique for scanning near-field microwave microscopy applications. *IEEE Transactions on Instrumentation and Measurement*, 63(5):1281–1286, May 2014.

[52] T. Wei, XD Xiang, WG WallaceFreedman, and PG Schultz. Scanning tip microwave near-field microscope. *Applied Physics Letters*, 68(24):3506–3508, 1996.

[53] S. Y. Semenov, A. E. Bulyshev, A. Abubakar, V. G. Posukh, Y. E. Sizov, A. E. Souvorov, P. M. van den Berg, and T. C. Williams. Microwave-tomographic imaging of the high dielectric-contrast objects using different image-reconstruction approaches. *IEEE Transactions on Microwave Theory and Techniques*, 53(7):2284–2294, 2005.

[54] J. Hoffmann, G. Gramse, J. Niegemann, M. Zeier, and F. Kienberger. Measuring low loss dielectric substrates with scanning probe microscopes. *Applied Physics Letters*, 105(1):13102, 2014.

[55] J. D. Chisum and Z. Popovic. Performance limitations and measurement analysis of a near-field microwave microscope for nondestructive and subsurface detection. *IEEE Transactions on Microwave Theory and Techniques*, 60(8):2605–2615, 2012.

[56] Taro Hitosugi, Ryota Shimizu, Tomihiro Hashizume, and Katsuya Iwaya. Systematic analyses of vibration noise of a vibration isolation system for high-resolution scanning tunneling microscopes. *Review of Scientific Instruments*, 82(8):083702–083702–6, 2011.

[57] C. Gao and X. . Xiang. Quantitative microwave near-field microscopy of dielectric properties. *Review of Scientific Instruments*, 69(11):3846–3851, 1998.

[58] Steven M. Anlage, Vladimir V. Talanov, and Andrew R. Schwartz. *Principles of Near-Field Microwave Microscopy*, pages 215–253. Springer New York, New York, NY, 2007.

[59] B. J. Feenstra, C. P. Vlahacos, A. S. Thanawalla, D. E. Steinhauer, S. K. Dutta, F. C. Wellstood, and S. M. Anlage. Near-field scanning microwave microscopy: measuring local microwave properties and electric field distributions. In *1998 IEEE MTT-S International Microwave Symposium Digest (Cat. No.98CH36192)*, volume 2, pages 965–968 vol.2, June 1998.

[60] N. N. Qaddoumi, M. Abou-Khousa, and W. M. Saleh. Near-field microwave imaging utilizing tapered rectangular waveguides. *IEEE Transactions on Instrumentation and Measurement*, 55(5):1752–1756, Oct 2006.

[61] Constantine A. Balanis. *Antenna theory: analysis and design*. Wiley, New York;Singapore;, 2nd, wiley singapore edition, 2003.

[62] Ho Young Lee, Yiyan Peng, and Yuri M. Shkel. Strain-dielectric response of dielectrics as foundation for electrostriction stresses. *Journal of Applied Physics*, 98(7):074104, 2005.

[63] Y. M. Shkel. Electrostriction: material parameters and stress/strain constitutive relations. *Philosophical Magazine*, 87(11):1743–1767, 2007.

[64] Andreas Trols, Alexander Kogler, Richard Baumgartner, Rainer Kaltseis, Christoph Keplinger, Reinhard Schwodiauer, Ingrid Graz, and Siegfried Bauer. Stretch dependence of the electrical breakdown strength and dielectric constant of dielectric elastomers. *Smart Materials and Structures*, 22(10):104012, 2013.

[65] Junjie Sheng, Hualing Chen, Bo Li, and Longfei Chang. Temperature dependence of the dielectric constant of acrylic dielectric elastomer. *Applied Physics A*, 110(2):511–515, Feb 2013.

[66] Sukesha, Renu Vig, and Navin Kumar. Effect of electric field and temperature on dielectric constant and piezoelectric coefficient of piezoelectric materials: A review. *Integrated Ferroelectrics*, 167(1):154–175, 2015.

[67] Anthony J. Bur. Dielectric properties of polymers at microwave frequencies: a review. *Polymer*, 26(7):963–977, 1985.

[68] JE Shigley and Mischke Shigley. Cr, & budynas, rg (2003). *Mechanical Engineering Design*, page 1056.

[69] W. E. Leithead and Yunong Zhang. O(n^2)-operation approximation of covariance matrix inverse in gaussian process regression based on quasi-newton bfgs method. *Communications in Statistics - Simulation and Computation*, 36(2):367–380, 2007.

[70] J. E. Dennis and Jorge J. Moree. Quasi-newton methods, motivation and theory. *SIAM Review*, 19(1):46–89, 1977.

[71] Anjali S Iyer-Pascuzzi, Olga Symonova, Yuriy Mileyko, Yueling Hao, Heather Belcher, John Harer, Joshua S Weitz, and Philip N Benfey. Imaging and analysis platform for automatic phenotyping and trait ranking of plant root systems. *Plant physiology*, 152(3):1148–1157, 2010.

[72] Keith Paustian, Nell Campbell, Chris Dorich, Ernest Marx, and Amy Swan. Assessment of potential greenhouse gas mitigation from changes to crop root mass and architecture. Technical report, Booz Allen Hamiltion Inc., McLean, VA (United States), 2016.

[73] Xiaodong Shi, Jiaoyang Li, Saptarshi Mukherjee, Srijan Datta, Vivek Rathod, Xinyu Wang, Wei Lu, Lalita Udpa, and Yiming Deng. Ultra-wideband microwave imaging system for root phenotyping. *Sensors*, 22(5):2031, 2022.

[74] Saoirse R. Tracy, Kerstin A. Nagel, Johannes A. Postma, Heike Fassbender, Anton Wasson, and Michelle Watt. Crop improvement from phenotyping roots: Highlights reveal expanding opportunities. *Trends in Plant Science*, 25(1):105–118, Jan 2020.

[75] Gernot Bodner, Alireza Nakhforoosh, Thomas Arnold, and Daniel Leitner. Hyperspectral imaging: a novel approach for plant root phenotyping. *Plant Methods*, 14(1):84, Oct 2018.

[76] Randy T. Clark, Robert B. MacCurdy, Janelle K. Jung, Jon E. Shaff, Susan R. McCouch, Daniel J. Aneshansley, and Leon V. Kochian. Three-dimensional root phenotyping with a novel imaging and software platform. *Plant Physiology*, 156(2):455–465, 2011.

[77] Albert L Smit, A Glyn Bengough, Christof Engels, Meine van Noordwijk, Sylvain Pellerin, and Siebe C van de Geijn. *Root methods: a handbook*. Springer Science & Business Media, 2013.

[78] JJ Schuurman, MAJ Goedewaagen, et al. *Methods for the examination of root systems and roots*. Centre for agricultural publications and documentation Wageningen, 1965.

[79] Gernot Bodner, Alireza Nakhforoosh, Thomas Arnold, and Daniel Leitner. Hyperspectral imaging: a novel approach for plant root phenotyping. *Plant methods*, 14(1):84, 2018.

[80] Wolfgang Böhm. *Methods of studying root systems*, volume 33. Springer Science & Business Media, 2012.

[81] GH Bates. A device for the observation of root growth in the soil. *Nature*, 139(3527):966–967, 1937.

[82] Ahmad B Moradi, Héctor M Conesa, Brett Robinson, Eberhard Lehmann, Guido Kuehne, Anders Kaestner, Sascha Oswald, and Rainer Schulin. Neutron radiography as a tool for revealing root development in soil: capabilities and limitations. *Plant and Soil*, 318(1-2):243–255, 2009.

[83] Peter J Gregory, DJ Hutchison, Derek B Read, Paul M Jenneson, Walter B Gilboy, and Edward J Morton. Non-invasive imaging of roots with high resolution x-ray micro-tomography. In *Roots: the dynamic interface between plants and the Earth*, pages 351–359. Springer, 2003.

[84] Saoirse R Tracy, Jeremy A Roberts, Colin R Black, Ann McNeill, Rob Davidson, and Sacha J Mooney. The x-factor: visualizing undisturbed root architecture in soils using x-ray computed tomography. *Journal of experimental botany*, 61(2):311–313, 2010.

[85] Sonja Schmidt, A Glyn Bengough, Peter J Gregory, Dmitri V Grinev, and Wilfred Otten. Estimating root–soil contact from 3d x-ray microtomographs. *European Journal of Soil Science*, 63(6):776–786, 2012.

[86] Jonathan A Atkinson, Michael P Pound, Malcolm J Bennett, and Darren M Wells. Uncovering the hidden half of plants using new advances in root phenotyping. *Current Opinion in Biotechnology*, 55:1–8, 2019. Analytical Biotechnology.

[87] Helen F Downie, MO Adu, Sonja Schmidt, Wilfred Otten, Lionel X Dupuy, PJ White, and Tracy A Valentine. Challenges and opportunities for quantifying roots and rhizosphere interactions through imaging and image analysis. *Plant, cell & environment*, 38(7):1213–1232, 2015.

[88] Ralf Metzner, Anja Eggert, Dagmar Van Dusschoten, Daniel Pflugfelder, Stefan Gerth, Ulrich Schurr, Norman Uhlmann, and Siegfried Jahnke. Direct comparison of mri and x-ray ct technologies for 3d imaging of root systems in soil: potential and challenges for root trait quantification. *Plant methods*, 11(1):17, 2015.

[89] Daniel Pflugfelder, Ralf Metzner, Dagmar van Dusschoten, Rüdiger Reichel, Siegfried Jahnke, and Robert Koller. Non-invasive imaging of plant roots in different soils using magnetic resonance imaging (mri). *Plant methods*, 13(1):102, 2017.

[90] Anton P. Wasson, Kerstin A. Nagel, Saoirse Tracy, and Michelle Watt. Beyond digging: Noninvasive root and rhizosphere phenotyping. *Trends in Plant Science*, 25(1):119–120, Jan 2020.

[91] Suqin Fang, Xiaolong Yan, and Hong Liao. 3d reconstruction and dynamic modeling of root architecture in situ and its application to crop phosphorus research. *The Plant Journal*, 60(6):1096–1108, 2009.

[92] Emanuela Turillazzi, Steven B Karch, Margherita Neri, Cristoforo Pomara, Irene Riezzo, and Vittorio Fineschi. Confocal laser scanning microscopy. using new technology to answer old questions in forensic investigations. *International journal of legal medicine*, 122(2):173–177, 2008.

[93] Sotirios A Tsaftaris and Christos Noutsos. Plant phenotyping with low cost digital cameras and image analytics. In *Information Technologies in Environmental Engineering*, pages 238–251. Springer, 2009.

[94] Noah Fahlgren, Malia A Gehan, and Ivan Baxter. Lights, camera, action: high-throughput plant phenotyping is ready for a close-up. *Current opinion in plant biology*, 24:93–99, 2015.

[95] Marc Faget, Stephan Blossfeld, Philipp Von Gillhaußen, Ulrich Schurr, and Vicky Martine Temperton. Disentangling who is who during rhizosphere acidification in root interactions: combining fluorescence with optode techniques. *Frontiers in plant science*, 4:392, 2013.

[96] Michelle Watt, Philip Hugenholtz, Rosemary White, and Kerry Vinall. Numbers and locations of native bacteria on field-grown wheat roots quantified by fluorescence in situ hybridization (fish). *Environmental Microbiology*, 8(5):871–884, 2006.

[97] Ajay Singhvi, Bo Ma, Johannes Daniel Scharwies, José R Dinneny, Butrus T Khuri-Yakub, and Amin Arbabian. Non-contact thermoacoustic sensing and characterization of plant root traits. In *2019 IEEE International Ultrasonics Symposium (IUS)*, pages 1992–1995. IEEE, 2019.

[98] N. Smith, L. A. Rivera, N. Burford, T. Bowman, M. O. El-Shenawee, and G. N. DeSouza. Towards root phenotyping in situ using thz imaging. In *2015 40th International Conference on Infrared, Millimeter, and Terahertz waves (IRMMW-THz)*, pages 1–2, 2015.

[99] Saptarshi Mukherjee, Xiaodong Shi, Yiming Deng, and Lalita Udpa. A hybrid microwave nde system for rapid inspection of gfrp composites. *Materials Evaluation*, 78(8):963–975, 2020.

[100] Vivek T. Rathod, Portia Banerjee, and Yiming Deng. *Low Field Methods (GMR, Hall Probes, etc.)*, pages 1–54. Springer International Publishing, Cham, 2019.

[101] Paulo Sergio de Paula Herrmann, Viktor Sydoruk, and Felipe Nieves Marques Porto. Microwave transmittance technique using microstrip patch antennas, as a non-invasive tool to determine soil moisture in rhizoboxes. *Sensors*, 20(4), 2020.

[102] Marion I Menzel, Susanne Tittmann, Jonas Buehler, Stella Preis, Norbert Wolters, Siegfried Jahnke, Achim Walter, Antonia Chlubek, Ariel Leon, Normen Hermes, et al. Non-invasive determination of plant biomass with microwave resonators. *Plant, cell & environment*, 32(4):368–379, 2009.

[103] Tribikram Kundu. *Nonlinear ultrasonic and vibro-acoustical techniques for nondestructive evaluation*. Springer, 2018.

[104] Saptarshi Mukherjee, Lalita Udpa, Yiming Deng, Premjeet Chahal, and Edward J Rothwell. Design of a microwave time reversal mirror for imaging applications. *Progress In Electromagnetics Research*, 77:155–165, 2017.

[105] Geoffroy Lerosey, J De Rosny, A Tourin, A Derode, G Montaldo, and M Fink. Time reversal of electromagnetic waves. *Physical review letters*, 92(19):193904, 2004.

[106] Saptarshi Mukherjee, Lalita Udpa, Satish Udpa, and Edward J Rothwell. Target localization using microwave time-reversal mirror in reflection mode. *IEEE Transactions on Antennas and Propagation*, 65(2):820–828, 2016.

[107] Saptarshi Mukherjee, Antonello Tamburrino, Mahmoodul Haq, Satish Udpa, and Lalita Udpa. Far field microwave nde of composite structures using time reversal mirror. *NDT & E International*, 93:7–17, 2018.

[108] Xiaodong Shi, Anthony Olvera, Ciaron Hamilton, Erzhuo Gao, Jiaoyang Li, Lucas Utke, Andrew Petruska, Zhenzhen Yu, Lalita Udpa, Yiming Deng, et al. Ai-enabled robotic nde for structural damage assessment and repair. *Materials Evaluation*, 79(7), 2021.

[109] Z. Liu, X.E.G., K. Tsukada, K. Hanasaki, and K. Takahashi. The use of wavelets for pixel level ndt data fusion. *NDT & E International*, 1999.

[110] Gonzalo Pajares and Jesús Manuel de la Cruz. A wavelet-based image fusion tutorial. *Pattern Recognition*, 37(9):1855–1872, 2004.

[111] Dipling H. Mueller. Experiences using rapid prototyping techniques to manufacture sheet metal forming tools. In *ISATA Conference*, 2000.

[112] J. Ding, P. Colegrove, J. Mehnen, S. Ganguly, P.M. Sequeira Almeida, F. Wang, and S. Williams. Thermo-mechanical analysis of wire and arc additive layer manufacturing process on large multi-layer parts. *Computational Materials Science*, 50(12):3315–3322, 2011.

[113] J. N. Zalameda, E. R. Burke, R. A. Hafley, K. M. Taminger, C. S. Domack, A. R. Brewer, and R. E. Martin. Thermal imaging for assessment of electron-beam freeform fabrication (ebf3) additive manufacturing deposits. In *Thermosense: Thermal Infrared Applications XXXV*, 2013.

[114] Gideon N. Levy, Ralf Schindel, and J.P. Kruth. Rapid manufacturing and rapid tooling with layer manufacturing (lm) technologies, state of the art and future perspectives. *CIRP Annals-Manufacturing Technology*, 52(2):589–609, 2003.

[115] D King and T Tansey. Rapid tooling: selective laser sintering injection tooling. *Journal of Materials Processing Technology*, 132(1):42–48, 2003.

[116] Donghong Ding, Zengxi Pan, Dominic Cuiuri, and Huijun Li. A multi-bead overlapping model for robotic wire and arc additive manufacturing (waam). *Robotics and Computer-Integrated Manufacturing*, 31:101–110, 2015.

[117] Yan Ma, Dominic Cuiuri, Chen Shen, Huijun Li, and Zengxi Pan. Effect of interpass temperature on in-situ alloying and additive manufacturing of titanium aluminides using gas tungsten arc welding. *Additive Manufacturing*, 8:71–77, 2015.

[118] Y. Zhou, S.F. Wen, B. Song, X. Zhou, Q. Teng, Q.S. Wei, and Y.S. Shi. A novel titanium alloy manufactured by selective laser melting: Microstructure, high temperature oxidation resistance. *Materials & Design*, 89:1199–1204, 2016.

[119] Scott M. Thompson, Linkan Bian, Nima Shamsaei, and Aref Yadollahi. An overview of direct laser deposition for additive manufacturing; part i: Transport phenomena, modeling and diagnostics. *Additive Manufacturing*, 8:36–62, 2015.

[120] E.O. Olakanmi, R.F. Cochrane, and K.W. Dalgarno. A review on selective laser sintering/melting (sls/slm) of aluminium alloy powders: Processing, microstructure, and properties. *Progress in Materials Science*, 74:401–477, 2015.

[121] Lawrence E. Murr, Sara M. Gaytan, Diana A. Ramirez, Edwin Martinez, Jennifer Hernandez, Krista N. Amato, Patrick W. Shindo, Francisco R. Medina, and Ryan B. Wicker. Metal fabrication by additive manufacturing using laser and electron beam melting technologies. *Journal of Materials Science & Technology*, 28(1):1–14, 2012.

[122] P. Heinl, C. K´orner, and R. F. Singer. Selective electron beam melting of cellular titanium: Mechanical properties. *Advanced Engineering Materials*, 10(9):882–888, 2008.

[123] P. Kulkarni, A. Marsan, and D. Dutta. A review of process planning techniques in layered manufacturing. *Rapid Prototyping Journal*, 6(1):18–35, 2000.

[124] Khan, Mushtaq, Dickens, and Phill. Selective laser melting (slm) of pure gold for manufacturing dental crowns. *Rapid Prototyping Journal*, 20(6):471–479, 2014.

[125] H. F. Wu, A. L. Gyekenyesi, P. J. Shull, T. Y. Yu, and E. I. Todorov. Measurement of electromagnetic properties of powder and solid metal materials for additive manufacturing. In *SPIE Smart Structures and Materials+ Nondestructive Evaluation and Health Monitoring*, page 1016907, 2017.

[126] Lore Thijs, Frederik Verhaeghe, Tom Craeghs, Jan Van Humbeeck, and Jean-Pierre Kruth. A study of the microstructural evolution during selective laser melting of ti-6al-4v. *Acta Materialia*, 58(9):3303–3312, 2010.

[127] S. Tammas-Williams, H. Zhao, F. Léonard, F. Derguti, I. Todd, and Philip B Prangnell. Xct analysis of the influence of melt strategies on defect population in ti-6al-4v components manufactured by selective electron beam melting. *Materials Characterization*, 102:47–61, 2015.

[128] Kamran Aamir Mumtaz, Poonjolai Erasenthiran, and Neil Hopkinson. High density selective laser melting of waspaloy®. *Journal of Materials Processing Technology*, 195(1):77–87, 2008.

[129] R. Li, J. Liu, Y. Shi, L. Wang, and W. Jiang. Balling behavior of stainless steel and nickel powder during selective laser melting process. *International Journal of Advanced Manufacturing Technology*, 59(9-12):1025–1035, 2012.

[130] Dongdong Gu and Yifu Shen. Balling phenomena in direct laser sintering of stainless steel powder: Metallurgical mechanisms and control methods. *Materials & Design*, 30(8):2903–2910, 2009.

[131] E. Yasa, J. Deckers, and J. Kruth. The investigation of the influence of laser re-melting on density, surface quality and microstructure of selective laser melting parts. *Rapid Prototyping Journal*, 17(5):312–327, 2011.

[132] Dongdong Gu and Yifu Shen. Processing conditions and microstructural features of porous 316l stainless steel components by dmls. *Applied Surface Science*, 255(5, Part 1):1880–1887, 2008.

[133] H. J. Niu and Ith Chang. Instability of scan tracks of selective laser sintering of high speed steel powder. *Scripta Materialia*, 41(11):1229–1234, 1999.

[134] J.P. Kruth, L. Froyen, J. Van Vaerenbergh, P. Mercelis, M. Rombouts, and B. Lauwers. Selective laser melting of iron-based powder. *Journal of Materials Processing Technology*, 149(1):616–622, 2004. 14th Interntaional Symposium on Electromachining (ISEM XIV).

[135] Tom Craeghs, Stijn Clijsters, Evren Yasa, and Jean-Pierre Kruth. Online quality control of selective laser melting. In *Proceedings of the 20th Solid Freeform Fabrication (SFF) symposium, Austin (Texas), 8-10 august*, pages 212–226, 2011.

[136] J. M. Waller, B. H. Parker, K. L. Hodges, E. R. Burke, and J. L. Walker. Nondestructive evaluation of additive manufacturing state-of-the-discipline report. Technical report, NTRS - NASA Technical Reports, 2014.

[137] H. Jiang. *Computed Tomography Principles, Design, Artifacts, and Recent Advances*. WA: SPIE Optical Engineering Press, Bellingham, 2009.

[138] F. Losano, G. Marinsek, A. M. Merlo, and M. Ricci. Computed tomography in the automotive field. development of a new engine head case study. In *International Symposium on Computerized Tomography for Industrial Applications and Image Processing in Radiology*, Berlin, Germany, 1999.

[139] Hakon Wadell. Volume, shape, and roundness of quartz particles. *The Journal of Geology*, 43(3):250–280, 1935.

[140] A. Townsend, L. Pagani, P. Scott, and L. Blunt. Areal surface texture data extraction from x-ray computed tomography reconstructions of metal additively manufactured parts. *Precision Engineering*, 48:254–264, 2017.

[141] Greet Kerckhofs, Grzegorz Pyka, Maarten Moesen, Simon Van Bael, Jan Schrooten, and Martine Wevers. High-resolution microfocus x-ray computed tomography for 3d surface roughness measurements of additive manufactured porous materials. *Advanced Engineering Materials*, 15(3):153–158, 2013.

[142] H. Attar, M. Calin, L.C. Zhang, S. Scudino, and J. Eckert. Manufacture by selective laser melting and mechanical behavior of commercially pure titanium. *Materials Science and Engineering: A*, 593:170–177, 2014.